Generation of Ultrashort Pulses – From Femtoseconds to Attoseconds

Louisy, Maite

2017

Document Version:
Publisher's PDF, also known as Version of record

Generation of Ultrashort Light Pulses – From Femtoseconds to Attoseconds

Maïté Louisy

Doctoral Thesis
2017

Lund University

Generation of Ultrashort Light Pulses
– From Femtoseconds to Attoseconds

Printed in Sweden by Media-Tryck, Lund, 2017

Division of Atomic Physics
Department of Physics
Faculty of Engineering, LTH
Lund University
P.O. Box 118
SE-221 00 Lund
Sweden
www.atomic.physics.lu.se

ISSN: 0281-2762
Lund Reports on Atomic Physics, LRAP 542 (2017)
ISBN: 978-91-7753-531-7 (print)
ISBN: 978-91-7753-532-4 (pdf)

Abstract

Electronic dynamics takes place on the attosecond timescale and can thus only be studied using a tool with attosecond temporal resolution. High harmonic generation (HHG) provides coherent attosecond pulses in the extreme ultraviolet spectral region. The work presented in this thesis focuses on generating and characterizing ultrashort femtosecond pulses and using them for HHG, together with a gating scheme, in order to produce isolated attosecond pulses (IAPs).

The first part describes the work on the generation of high-energy, few-cycle femtosecond pulses using post-compression schemes, with emphasis on gas-filled, hollow-core capillary post-compression systems. General scaling laws for nonlinear optics in gases were identified.

The second part focuses on the compression and characterization of ultrabroadband femtosecond pulses with emphasis on the dispersion scan (d-scan) technique for characterization of the pulses and on the stabilization of the carrier-to-envelope offset phase. Significant improvements were made in the d-scan technique, namely, a new, faster retrieval algorithm and a novel, compact, single-shot design.

The last part deals with HHG. First, a pump-probe scheme called RABBIT (reconstruction of attosecond beating by interference of two-photon transitions) is described, with emphasis on its application to measure the phase across a Fano resonance. Then, a novel gating technique, called noncollinear optical gating, allowing the generation of several, spatially separated, synchronized IAPs, is presented together with its experimental demonstration.

Popular Scientific Summary

The atom, the heart of all matter, that constitutes everything around us, is still a scientific mystery. The motion of the elementary particles forming the atom, including the ultrafast motion of electrons, is still not completely understood. However, in the last decades, scientists took valuable steps towards a better understanding of the atom by finally obtaining glimpses of the motion of electrons using lasers generating extremely short pulses of light that are only hundreds of attoseconds long.

An attosecond is 0.000,000,000,000,000,001 seconds; almost impossible for the human mind to imagine. Let me give you some comparisons. An attosecond is to a second, what a second is to twice the age of the universe. In one second, light can circle the earth $7^1/_2$ times, while in an attosecond, light could barely travel from one side of a molecule to the other.

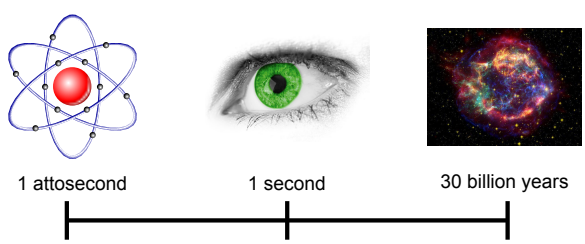

Figure 1: An attosecond is to a second, what a second is to twice the age of the universe.

The motion of electrons is on the attosecond timescale. If we could see things as small as electrons, think at the speed of light, and perceive events on the attosecond timescale, we would be able to see the electron cloud around the nucleus of the atom. We would not see electrons neatly circling the nucleus like a tiny solar system, as electrons do not occupy specific orbits; rather, they are everywhere at the same time and only have a higher probability of being in certain places (along certain trajectories) than in others. They do not make the same repetitive circuits, but have the ability to jump back and forth between different trajectories. If we could see things on the attosecond timescale, we would be able to see how their trajectories change when light interacts with the atom, and what happens when atoms come together to form molecules. It would also be possible to see the effects that take place when molecules interact with each other during chemical reactions. This is the dream of all atomic physicists.

But, back to reality, how can we observe a movement that is way too fast for the human eye?

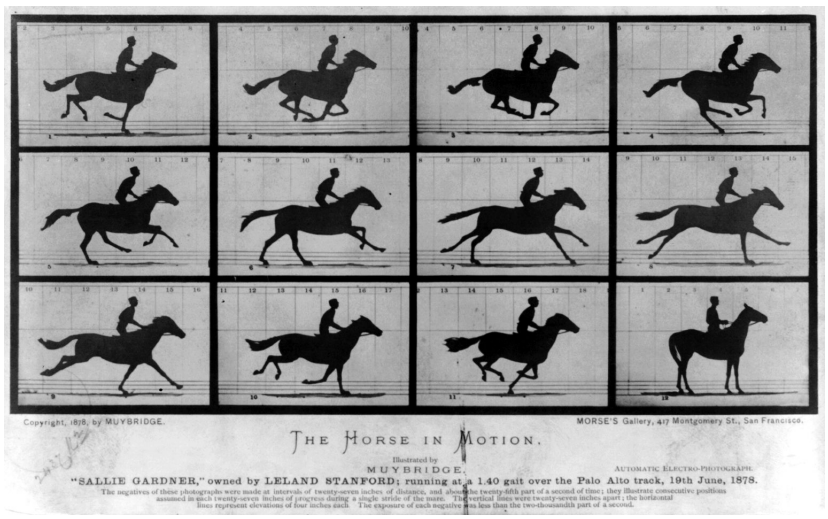

Figure 2: In the middle of the 19th century, a British photographer, Eadweard Muybridge, wondered if a galloping horse had all four feet off the ground at any instant. To answer this question, he constructed 16 cameras with a mechanical shutter able to open and close in only six milliseconds (0.006 seconds), which was fifty times faster than a blink of an eye. With these cameras, he was able to take sharp pictures of a fast-moving horse. This was the first step towards slow-motion photography.

When a camera takes a picture, it records all the light reaching the detector during the exposure time. To take sharp pictures of very rapid motion, the exposure time must be extremely short. This can be achieved with a fast mechanical shutter that will allow the light to reach the detector during only a short time. It can also be done using a short flash of light. The object to be photographed is illuminated for a very short time, during which it will reflect the light towards the detector. If the flash has a shorter duration than the motion, the image will be sharp. By taking many pictures one after the other, we can create a slow-motion video showing very interesting features that could not be observed with our eyes alone.

No mechanical shutter can move sufficiently fast to observe the ultrafast movements of electrons in an atom. However, we can record images by illuminating atoms with a flash of light that lasts for a shorter time than the motion of the electrons we want to observe, in a similar way as taking a picture with a flash on a normal camera.

Since the discovery of the electron at the end of the 19th century, scientists have had the dream of being able to observe the motion of electrons. The invention of the laser and its rapid development in the second half of the 20th century made this possible, and about 15 years ago, a new field of research, called attosecond science, was created. Research groups all over the world are now trying to observe and understand the motion of electrons using flashes of light hundreds of attoseconds long.

Creating such short flashes of light is not easy, as there is a fundamental limitation on how short a flash of light can be. Light can be described as an oscillation, or vibration, of an electromagnetic field that travels like waves on water. Flashes of

light cannot be made shorter than the periodicity of their oscillation, in other words, they cannot have less than one wave crest. Visible light, the light that our eyes can perceive, oscillates with a periodicity of about two femtoseconds (2000 attoseconds), thus, a flash of visible light cannot be shorter than 2000 attoseconds.

In order to obtain shorter flashes (hundreds of attoseconds), we need to increase the frequency of the oscillations, bring the wave crests closer to each other. This changes the "colour" of the light towards the ultraviolet. Such light is not visible to the human eye, is absorbed by air (so it can only propagate in vacuum), and is potentially harmful to the eyes and skin. However, this is the light we need to observe the motion of electrons.

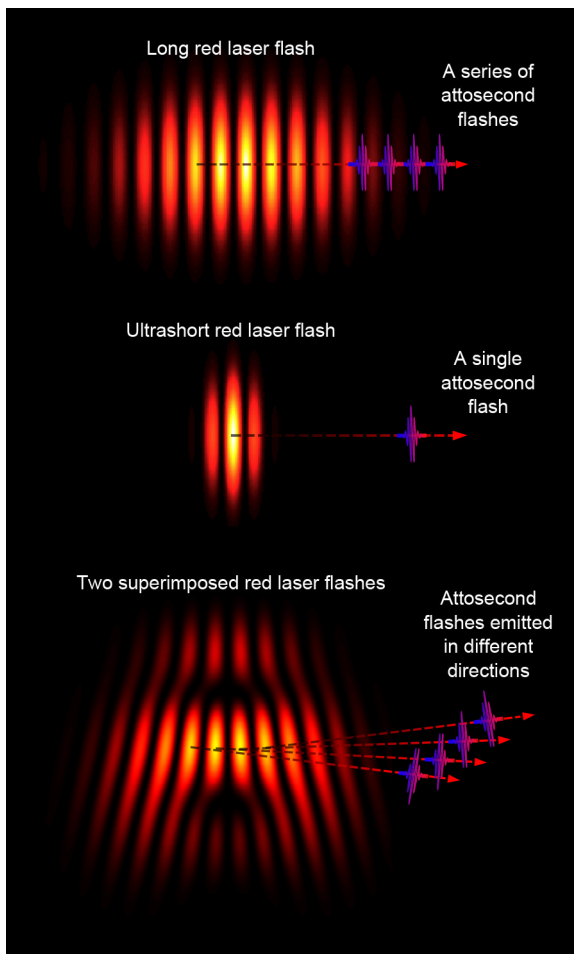

Figure 3: A flash of light from a red laser will propagate like waves on water. Every time a new crest reaches the gas, it will create an attosecond, ultraviolet flash of light.

Such light can be generated by firing an extremely powerful red laser into a gas. This technique is called "high harmonic generation" (HHG). Every time a wave crest from the red laser flash reaches the gas, it will interact with the atoms and an attosec-

ond ultraviolet flash of light will be created. So a single flash from the red laser will create a series of much shorter ultraviolet flashes.

However, returning to our comparison with a normal camera, a series of flashes will not provide a sharp picture of the motion, since light will reach the detector at different times during the motion, and several images will, therefore, be superimposed in the picture. This will result in a blurred picture.

Despite the fact that scientists have developed tricks to obtain information about the motion of electrons using series of flashes, it is still desirable to use a single attosecond flash of light. Most of the work presented in this thesis was aimed at creating such a single flash of light, called an "isolated attosecond pulse" (IAP).

The most straightforward method consists of shortening the flash from the red laser until only one wave crest is left and, thus, only one ultraviolet attosecond flash is created. In this thesis, I describe how this can be done by passing the red laser through a hollow glass tube filled with gas. When the intense light from the red laser travels through the gas, it changes the nature of the gas, which in turn changes the nature of the light. The flash of light is changed from red to white, thus lowering the limit on how short the flash can be. The flash is then directed by a series of special mirrors, called "chirped mirrors", which shorten the duration of the flash as close as possible to this new limit. This technique is called "hollow-capillary post-compression".

However, due to experimental difficulties, the resulting flashes usually still contain a few wave crests. In order to generate single attosecond flashes by HHG, it is necessary to isolate a single wave crest. This is called "gating". In this thesis, a novel gating technique called "noncollinear optical gating" (NOG) is described. This consists of superimposing two flashes from the red laser, coming from different directions. When this superimposed flash reaches the gas, it will propagate like a series of waves, where subsequent waves are slightly rotated in respect to each other. This results in each ultraviolet attosecond flash being emitted in a different direction. Therefore, a single flash can be selected by shielding the detector from the others.

Attosecond flashes of light have already been used by scientists for 16 years to observe and understand the motion of electrons. Much has already been discovered, but there is still a great deal left to do. John Tisch, professor at Imperial College London, a researcher in attosecond science, said: "At the moment our work is like that of a movie cameraman, recording the movements of the electrons. One day, we would like to become like movie directors, making the electrons move where we want. If we could do this, we could control chemical reactions, design new materials, and create faster, more efficient electronic devices." Attosecond science may perhaps lead to breakthroughs in technology, chemistry and medicine, but one thing is sure, it will give us a better understanding of the world around us.

List of Publications

This thesis is based on five papers which are referred to by their Roman numerals in the text, and appended at the end of the thesis.

I **Fast iterative retrieval algorithm for ultrashort pulse characterization using dispersion scans**
M. Miranda, J. Penedones, C. Guo, A. Harth, M. Louisy, L. Neoricic, A. L'Huillier, and C. L. Arnold.
Journal of the Optical Society of America B **34**, 190-197 (2017).

II **Compact single-shot d-scan setup for the characterization of few-cycle laser pulses**
M. Louisy*, C. Guo*, L. Neoricic, S. Zhong, A. L'Huillier, C. L. Arnold, and M. Miranda;
(*Authors contributed equally).
Applied Optics **56**, 9084-9089 (2017).

III **Gating attosecond pulses in a noncollinear geometry**
M. Louisy*, C. L. Arnold*, M. Miranda, E. W. Larsen, S. N. Bengtsson, D. Kroon, M. Kotur, D. Guénot, L. Rading, P. Rudawski, F. Brizuela, F. Campi, B. Kim, A. Jarnac, A. Houard, J. Mauritsson, P. Johnsson, A. L'Huillier, and C. M. Heyl;
(*Authors contributed equally).
Optica **2**, 563-566 (2015).

IV **Scale-invariant nonlinear optics in gases**
C. M. Heyl, H. Coudert-Alteirac, M. Miranda, M. Louisy, K. Kovacs, V. Tosa, E. Balogh, K. Varjú, A. L'Huillier, A. Couairon, and C. L. Arnold.
Optica **3**, 75-81 (2016).

V **Spectral phase measurement of a Fano resonance using tunable attosecond pulses**
M. Kotur, D. Guénot, D. Kroon, E. W. Larsen, M. Miranda, M. Louisy, S. N. Bengtsson, S. Carlström, J. Mauritsson, J. M. Dahlström, S. E. Canton, M. Gisselbrecht, C. L. Arnold, and A. L'Huillier.
Nature Communications **7**, 10566 (2016).

Abbreviations

ALH	Attosecond lighthouse
CCD	Charge-coupled device
CEP	Carrier–envelope phase
CEO	Carrier–envelope phase offset
CPA	Chirped pulse amplification
DFG	Difference frequency generation
DOG	Double optical gating
d-scan	Dispersion scan
FROG	Frequency-resolved optical gating
FWHM	Full width at half maximum
GD	Group delay
GDD	Group delay dispersion
GVD	Group velocity dispersion
HHG	High harmonic generation
HeNe	Helium-neon
IAP	Isolated attosecond pulse
KDP	Potassium dihydrogenphosphate
MIIPS	Multiphoton intrapulse interference phase scan
NIR	Near-infrared
NOG	Noncollinear optical gating
OPCPA	Optical parametric chirped-pulse amplification
PPT	Perelomov, Popov and Terent'ev
RABBIT	Reconstruction of attosecond beating by interference of two-photon transitions
RMS	Root mean square
SHG	Second-harmonic generation
SPIDER	Spectral phase interferometry for direct electric field reconstruction
SPM	Self-phase modulation

TDSE	Time-dependent Schrödinger equation
TOD	Third-order dispersion
WFR	Wavefront rotation
XPW	Cross-polarized wave generation
XUV	Extreme ultraviolet

Symbols

$A = 1 - T$	Overall propagation loss
a	Inner radius of a hollow-core capillary
$\mathbf{B}$	Magnetic flux density
B	B-integral which represents the accumulated nonlinear phase
$c = 299\ 792\ 458$ m/s	Speed of light in vacuum
$\mathbf{D}$	Electric displacement
d	Dipole moment
d_q	Dipole moment of the harmonic q
E_{kin}	Kinetic energy
$\mathbf{E}$	Electric field
E	Scalar electric field
$\hat{E}$	Scalar electric field in the frequency domain
$\hat{\mathcal{E}}$	Scalar electric field in the frequency domain, in the moving frame
$e \approx 1.602 \times 10^{-19}$ C	Charge of an electron
e_{12}	Distance between the two mirrors of a telescope
$1\,\text{eV} = 1.602 \times 10^{-19}$ J	Electronvolt – unit of energy
F	Spectral broadening factor
f	Focal length or frequency
G	Error for d-scan retrievals
$\text{GD} = \partial\hat{\varphi}/\partial\omega$	Group delay
$\text{GDD} = \partial^2\hat{\varphi}/\partial\omega^2$	Group delay dispersion
GVD	GDD per unit length
H	Coupling coefficient
$\hbar \approx 1.055 \times 10^{-34}$ Js	Reduced Planck constant
I	Intensity
$\hat{I}$	Spectral intensity

I_p	Ionization potential
$\mathbf{J}$	Current density of free charges
J_0	Zeroth-order Bessel function
$k = n\omega/c$	Wavenumber
$K = k - \omega/c$	
$k_0 = 2\pi/\lambda_0$	Free-space wavenumber
L	Interaction length
$\hat{M}$	Frequency marginal
M^2	Beam quality factor
$m_e \approx 9.109 \times 10^{-31}\,\mathrm{kg}$	Mass of an electron
N_e	Density of free electrons
$n = \sqrt{\varepsilon} = n_0 + n_2 I$	Refractive index
n_0	Linear refractive index
n_2	Nonlinear coefficient of the refractive index
$n_c = n + i\alpha$	Complex refractive index
$\mathbf{P}$	Nonlinear polarization
P	Scalar nonlinear polarization
$\hat{P}$	Scalar nonlinear polarization in the frequency domain
$\hat{\mathcal{P}}$	Scalar nonlinear polarization in the frequency domain, in the moving frame
P_Laser	Pulse peak power
P_in	Pulse initial peak power
P_crit	Critical power for self-focusing
p	Gas pressure
q	Harmonic number
$\hat{R}$	Spectral response of a d-scan system
R	Radius of curvature
$R_\mathrm{T} = R\cos\theta$	Effective radius of curvature in the tangential plane
$R_\mathrm{S} = R/\cos\theta$	Effective radius of curvature in the sagittal plane
r	Radius
SB	Sideband amplitude
T	Cycle period
Tr	Transmission
$\mathrm{TOD} = \partial^3\hat{\varphi}/\partial\omega^3$	Third-order dispersion
$U_\mathrm{p} = e^2E_0^2/(4m_e\omega_0^2)$	Ponderomotive energy
V	Atomic potential
$v_p = c/n$	Phase velocity

w_0	Gaussian beam waist radius at focus ($1/e^2$ of the intensity)
w_L	Gaussian beam waist radius before focusing ($1/e^2$ of the intensity)
w_m	Ionization rate
z	Length
z_{R}	Rayleigh length
z_{cr}	Critical length after which the beam collapses due to self-focusing
α	Field attenuation
α_{T}	Threshold parameter for self-focusing
β	Wavefront rotation angle or diffraction angle of a grating
ϵ	Pulse energy
ϵ_{in}	Pulse initial energy
ϵ_{out}	Pulse final energy
$\varepsilon_0 = 8.854 \times 10^{-12}$ F/m	Vacuum permittivity
$\varepsilon = 1 + \chi$	Relative permittivity
η	Scaling parameter
θ	Angle of incidence
Γ	Grating pitch
γ	Ionization probability or noncollinear angle
δ	Spatial separation
Δk	Wave vector mismatch
Δt	Time delay
$\Delta\phi_{\mathrm{atom}}$	Intrinsic phase difference of the matrix elements corresponding to photoionization from the harmonics $q+1$ and $q-1$
$\Delta\phi_q = \Delta\phi_{q+1} - \Delta\phi_{q-1}$	Phase difference between harmonics $q+1$ and $q-1$
λ	Instantaneous wavelength
λ_0	Central wavelength
$\mu_0 = 4\pi \times 10^{-7}$ N/A^2	Vacuum permeability
μ	Factor minimizing the error between two traces
ρ	Gas density
τ	Pulse duration FWHM
φ	Phase
$\hat{\varphi}$	Spectral phase
ϕ	Phase shift
ϕ_{CE}	Carrier–envelope phase

χ	Susceptibility of the medium
$\chi^{(3)} = 4\varepsilon_0 c n_2 n_0^2/3$	Third-order susceptibility
Ψ	Wave function
$\omega = 2\pi c/\lambda$	Instantaneous angular frequency
$\omega_0 = 2\pi c/\lambda_0$	Carrier angular frequency

Contents

Chapter 1

Introduction

When referring to the duration of a laser pulse, "Ultrashort" is a subjective term. It depends on the historical context and the technologies available at the time. The term "ultrashort" was first used to describe sub-ps pulses. Nowadays, this is not considered so short anymore since near-infrared (NIR) pulses in the femtosecond regime and extreme ultraviolet (XUV) pulses in the attosecond regime are routinely generated. Whether a pulse is considered ultrashort also depends on its central frequency: 2.7 fs corresponds to a single-cycle of an electric field at 800 nm but to many cycles of an XUV pulse. A good definition of an ultrashort pulse is a pulse with a spectral bandwidth comparable to its central frequency, this is equivalent to a pulse with a duration comparable to the duration of its carrier cycle.

An ultrashort pulse of light is a wave packet that is extremely localized in time. This implies a broad spectrum. One way of generating ultrashort pulses is to broaden the spectrum of a longer pulse. If the intensity is high enough to trigger nonlinear effects while propagating in a dielectric medium or a gas, new frequencies can appear, resulting in spectral broadening of the pulse.

However, generation of a broad spectrum does not automatically lead to a short pulse, mainly because of dispersion, i.e., different spectral components propagate at different speeds. Therefore, as the pulse propagates, it becomes stretched in time. This phenomenon increases as the spectrum becomes broader, which means that the shortest pulses are the most difficult to keep short. Fortunately, dispersion can be compensated for by making different spectral components travel different distances. This can be achieved using compressors consisting of gratings [1–4], prisms [5–8] or chirped mirrors [9–11].

Several methods have been developed to generate high-power, ultrashort femtosecond pulses. Post-compression techniques combine spectral broadening and ultra-broadband dispersion compensation to provide high-energy, few-cycle femtosecond pulses. Post-compression is usually implemented after Ti:sapphire, chirped pulse amplification (CPA) laser systems, which routinely deliver pulses at 800 nm with tens of femtoseconds duration and multi-millijoule energy. The most common post-compression technique is based on spectral broadening in a gas-filled hollow-core glass fibre [12, 13]. Another post-compression technique is based on creating a filament in a gas [14, 15]. A different approach to few-cycle pulses is optical parametric chirped-

pulse amplification (OPCPA) [16], which combines optical parametric amplification and CPA to provide high-peak-power, few-cycle femtosecond pulses.

In the development of ultrashort pulsed laser systems, and their applications, it is crucial to be able to characterize the pulses. However, their characterization is not straightforward. Several methods have been developed during recent decades. One of them, the dispersion scan (d-scan) technique [17], was developed at the Division of Atomic Physics at Lund University (in collaboration with the Department of Physics and Astronomy at the University of Porto).

Figure 1.1 shows a typical spectrum obtained by nonlinear propagation in a gas-filled, hollow-core capillary, and the temporal profile of the pulse, characterized using the d-scan technique, after compression with a chirped-mirror compressor. The spectrum can support a Fourier-limited pulse duration of 2.9 fs. After compression, a pulse duration of 3.2 fs was obtained.

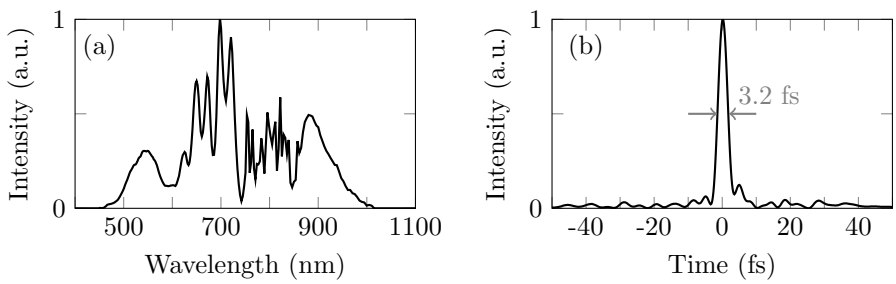

Figure 1.1: a) A spectrum obtained by spectral broadening of a NIR pulse by nonlinear propagation through a gas-filled hollow-core capillary. b) Measured temporal profile of this pulse after compression with a chirped-mirror compressor.

To generate even shorter pulses, femtosecond NIR pulses can be used to generate attosecond XUV pulses via high harmonic generation (HHG) [18, 19]. High-order harmonics are created when an intense laser field is focused into a gas. Typically, HHG leads to a train of attosecond pulses where a pulse with a duration of about a hundred attoseconds is emitted at every half cycle of the driving field. However, an isolated attosecond pulse (IAP) with a broad continuous spectrum is desirable in many applications. IAPs can be generated by using few-cycle femtosecond pulses to drive the HHG process, often combined with a gating technique in order to confine the generation to a single half-cycle of the field.

Attosecond pulses have been used to investigate ultrafast electron dynamics, induced by the interaction of light with matter, in atoms, molecules, and solids. These dynamics play a crucial role in many chemical or biological processes in which electrons are transferred, e.g., in the early stages of photosynthesis or radiation damage of molecules. Ultimately, attosecond pulses could eventually be used to control these dynamics.

1.1 Motivation

The aim of this research was to develop an IAP source. For this purpose, I worked on generating few-cycle femtosecond pulses. I used mainly gas-filled hollow-core cap-

illaries together with chirped-mirror compressors, but filaments were also studied. The pulses produced were characterized using the d-scan technique, which was further developed during my PhD. A faster retrieval algorithm was developed (Paper I), and a compact single-shot system was designed (Paper II). Finally, I used the ultrashort femtosecond pulses for HHG with a novel gating method called noncollinear optical gating (NOG), allowing the generation of several spatially separated IAPs (Paper III). Moreover, a general scale invariance of nonlinear light–matter interactions in gases (i.e., propagation in a gas-filled capillary, filamentation and HHG) was identified (Paper IV), thus opening the way for versatile IAP sources. As a side-project, to familiarize myself with attosecond science applications, I used attosecond pulse trains to study electron dynamics in the vicinity of a Fano resonance (Paper V).

1.2 Experimental environment

1.2.1 The different experiments: a chronological presentation

Figure 1.2 shows the layout of the laboratory where the experimental work was performed. The laser system is mounted on the top right table, and the output beam can be directed to different setups. Long pulses ($\sim$ 20 fs) can be used for HHG in two setups. First, the HHG setup on the right was used for RABBIT (reconstruction of attosecond beating by interference of two-photon transitions) measurements of a Fano resonance in argon. Then, a first post-compression hollow-capillary system was constructed for this HHG setup. The ultrashort pulses generated were used to create IAPs using NOG. A filamentation setup was temporarily constructed on the top left table to perform scaling experiments. Afterwards, a new post-compression hollow-capillary system was constructed, scaled up for input energy, and the ultrashort pulses generated were characterized with the d-scan technique using a new improved retrieval algorithm. Finally, a new d-scan setup was constructed for single-shot characterization of these ultrashort pulses.

Since the same laser system was used for all the experiments presented in this thesis, a detailed description is given below.

1.2.2 The laser system

The laser system is a CPA-based Ti:sapphire laser. The oscillator (Rainbow v1, Femtolasers) is a chirped-mirror-based, Kerr-lens mode-locked system and delivers 2 nJ at 800 nm with a repetition rate of 78 MHz. The pulses have a bandwidth greater than 300 nm, which can support a duration of less than 7 fs. After the oscillator, the pulses are stretched to 400 ps by a grating stretcher based on a low-aberration, all-reflective Öffner triplet design [4]. The stretcher has a bandwidth of 130 nm.

Once stretched, the pulses pass through an acousto-optic, programmable dispersive filter [20] (Dazzler, Fastlite). This system consists of a birefringent crystal and a programmable ultrasound generator. A grating is created in the crystal by an acoustic wave, and the light is diffracted from the ordinary mode (fast propagation) to the extraordinary mode (slow propagation) at a time depending on its frequency. Therefore, a frequency-dependent time delay is added to the pulse. In this way, the spectral phase and amplitude can be controlled independently.

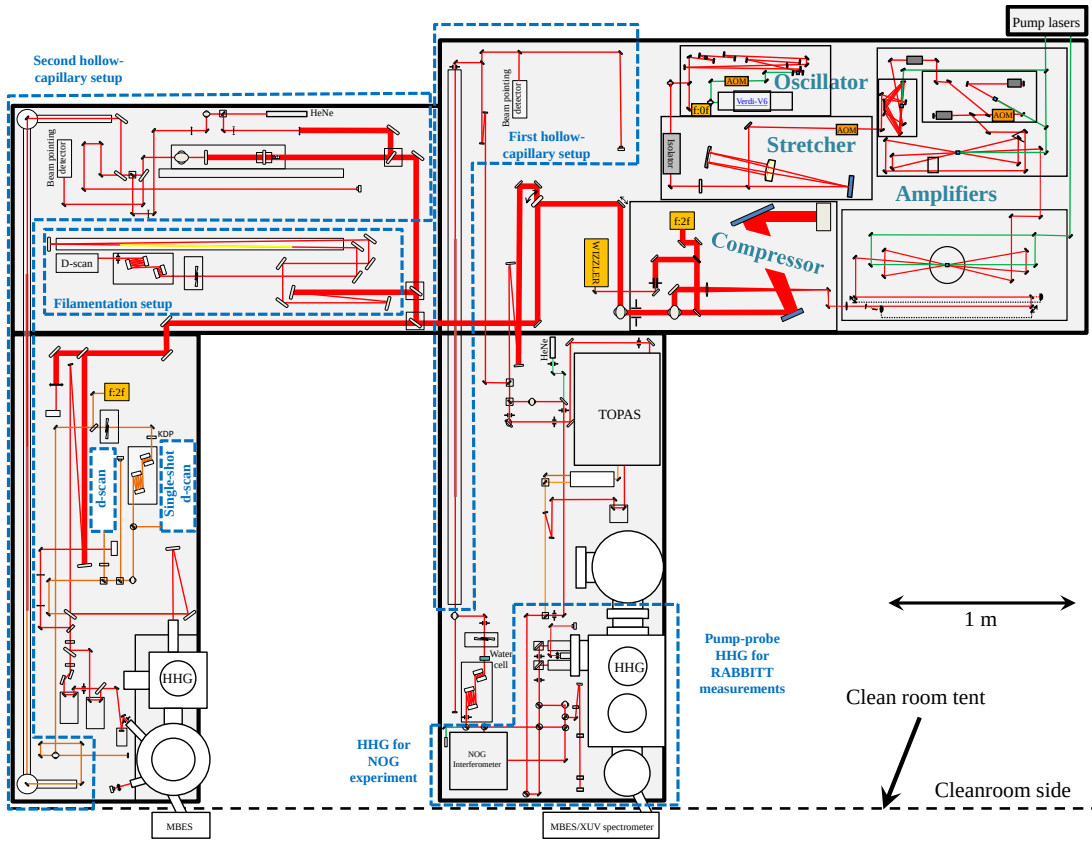

Figure 1.2: Layout of the laboratory where all the work presented in this thesis was performed. The laser system used in all the experiments is shown on the top right table. The blue dashed frames indicate the different experimental setups used in this work.

The beam is then amplified by four consecutive amplifiers with Ti:sapphire gain crystals pumped at 527 nm. The first amplifier is a 4-pass amplifier which pre-amplifies the pulses to 250 nJ in order to raise the seed energy for the following regenerative amplifier. Then, a picker Pockels cell sets the frequency to 1 kHz by opening for a very short time (about 10 ns), every ms, to let a single pulse pass through. The second amplifier is a regenerative amplifier with two Pockels cells which let the pulse in and out of the cavity. An acousto-optic programmable gain filter [21] (Mazzler, Fastlite) is placed in the cavity to counteract the effects of gain narrowing. It introduces spectral losses through partial diffraction to the spectral components with the highest gain. After 13 round trips in the regenerative amplifier, the pulses have acquired an energy of 0.5 mJ. The last two amplifiers are 3-pass bow-tie amplifiers that are able to amplify the pulses to 3 mJ and 10 mJ, respectively. The last amplifier is cryogenically cooled to 123 K in order to minimize the effect of thermal lensing.

Finally, a grating compressor is used, and near-transform-limited, 20 fs, 5 mJ, 800 nm pulses with a spectral bandwidth of up to 100 nm can be delivered. However, only 3 mJ pulses are generated on a regular basis to avoid the risk of burning the gain

crystal in the last amplifier and to increase the lifetime of the pump lasers.

The pulses are characterized using a system based on self-referenced spectral interferometry [22, 23] (Wizzler, Fastlite). A reference pulse with a flat spectral phase and a spectrum broader than the input pulse is created from the input pulse by cross-polarized wave generation (XPW) [24]. Pulses are initially rather close to the Fourier limit, therefore, the temporal filtering of the XPW effect is sufficient to create a reference pulse with a reasonably flat spectral phase. Since XPW is a third-order nonlinear process, the spectral phase of the generated pulse should be three times flatter than that of the fundamental. Both pulses are then delayed and overlapped. The resulting spectral interference is measured, and the phase difference between the reference and the input pulse is retrieved by Fourier-transform spectral interferometry [25]. Near-transform-limited pulses are obtained from the combined actions of the Dazzler and Wizzler. The spectral phase is measured with the Wizzler and corrected with the Dazzler. A flat spectral phase is obtained after a few iterations. Moreover, the entire chain can be actively CEP-stabilized.

The Dazzler also allows the central frequency of the laser to be tuned. Frequencies on one side of the spectrum are removed, reducing the bandwidth around a shifted central frequency. A tunability of about 50 nm can be achieved. This feature was used in the experiment described in Paper V.

1.3 Outline of this thesis

In Chapter 2, the theoretical concepts behind the generation of few-cycle femtosecond pulses by post-compression, using gas-filled hollow-core capillaries or filaments, are presented. The scale invariance of such nonlinear interactions is also discussed as an introduction to Paper IV. Experimental results are presented and discussed.

Chapter 3 presents three major components of ultrafast femtosecond science: ultrabroadband dispersion compensation, temporal characterization, and CEP stability. Dispersion compensation and CEP stability follow directly from the previous chapter, being the last important pieces of a post-compression system. The section on temporal characterization describes the work performed to improve the d-scan technique. The technique is discussed and the improved retrieval algorithm presented in Paper I is described. A novel compact design for single-shot d-scan measurements is then presented, introducing Paper II, and providing complementary information on the calculations behind this design.

Chapter 4 describes HHG using a semi-classical model. Its scale invariance is then briefly discussed. A detailed demonstration is found in Paper IV. Following this, one particular experiment is explored: RABBIT, and its application to measure the spectral phase of a Fano resonance, as an introduction to Paper V. Finally, the generation of IAPs is described, and the NOG scheme described in Paper III is presented.

The Appendix provides a practical guide for the construction and operation of a hollow-capillary post-compression system. This part of the thesis is not the synthesis of published work, but rather a detailed description of experimental solutions aiming at helping the reader to construct a hollow-capillary post-compression system.

Chapter 2

Generation of ultra-broadband femtosecond pulses

2.1 Introduction

Nonlinear effects occurring during the propagation of an intense laser pulse in a dielectric medium or a gas can create new frequencies. One of these effects is called self-phase modulation (SPM), and is widely used for post-compression of NIR femtosecond pulses.

In this chapter, an introduction is given to wave propagation and the nonlinear effects relevant to the work described in this thesis. It will then be shown how spectral broadening of NIR femtosecond pulses can be achieved using SPM in a gas-filled hollow capillary [12, 13] or in a filament [14, 15]. Finally, the scaling principle presented in Paper IV, which states that, in most cases, the propagation of linearly polarized light and its linear and nonlinear interactions with gases are scale-invariant, provided the spatial dimensions, gas density and pulse energy are scaled appropriately, is presented. Emphasis is placed on the scaling of hollow capillaries and filaments. The scaling of HHG will be discussed in Chapter 4.

2.2 Introduction to wave propagation

The propagation of light through a medium involves the absorption and re-emission of the light by the atoms constituting the medium. Light is an electromagnetic wave. When it travels through a medium, its energy is absorbed by the atoms, causing the electrons within the atom to undergo vibrations. This vibration has the same frequency as the incoming wave. Therefore, the electric dipoles created will emit a new electromagnetic wave with the same frequency. This is the linear response of the medium. However, if the incoming light is a very intense laser, the response can become nonlinear, and frequency variations may occur.

The interaction of light with matter can be described classically by Maxwell's equations. A wave equation can be derived directly from Maxwell's equations, the solution of which is the electromagnetic field of the light.

Let us consider the Maxwell–Faraday and the Maxwell–Ampère equations:

$$\nabla \times \mathbf{E} = -\frac{\partial \mathbf{B}}{\partial t} \tag{2.1}$$

$$\nabla \times \mathbf{B} = \mu_0 \left(\mathbf{J} + \frac{\partial \mathbf{D}}{\partial t} \right) \tag{2.2}$$

where the constant μ_0 is the vacuum permeability and the field variables: $\mathbf{E}$, $\mathbf{B}$, $\mathbf{J}$ and $\mathbf{D}$, are the electric field, the magnetic flux density, the current density of free charges, and the electric displacement, respectively. All field variables are functions of space and time. A Fourier transform takes a field variable $\mathbf{F}(t)$ from the time domain to the spectral domain: $\hat{\mathbf{F}}(\omega) = \int_{-\infty}^{\infty} \exp(i\omega t)\, \mathbf{F}(t) dt$, where ω is the angular frequency. Equations 2.1 and 2.2 become:

$$\nabla \times \hat{\mathbf{E}} = -i\omega \hat{\mathbf{B}} \tag{2.3}$$

$$\nabla \times \hat{\mathbf{B}} = \mu_0 (\hat{\mathbf{J}} + i\omega \hat{\mathbf{D}}) \tag{2.4}$$

By taking the curl of Equation 2.3, we can combine Equations 2.3 and 2.4, leading to:

$$\nabla \times (\nabla \times \hat{\mathbf{E}}) = \mu_0 (-i\omega \hat{\mathbf{J}} + \omega^2 \hat{\mathbf{D}}) \tag{2.5}$$

The electric displacement is a function of the polarization, which is a measure of the density of electric dipoles:

$$\hat{\mathbf{D}} = \varepsilon_0 \varepsilon(\omega) \hat{\mathbf{E}}(\omega) + \hat{\mathbf{P}} \tag{2.6}$$

where ε_0 is the vacuum permittivity, $\varepsilon(\omega) = 1 + \chi(\omega)$ is the relative permittivity, and $\chi(\omega)$ is the susceptibility of the medium. $\hat{\mathbf{P}}$ denotes the nonlinear polarization; the linear polarization is included in $\varepsilon(\omega)$. The refractive index of the medium can be expressed as $n = \sqrt{\varepsilon}$ and the speed of light in vacuum as $c = (\mu_0 \varepsilon_0)^{-1/2}$. Therefore, inserting Equation 2.6 into Equation 2.5 leads to:

$$\nabla \times (\nabla \times \hat{\mathbf{E}}) - \frac{n^2 \omega^2}{c^2} \hat{\mathbf{E}} = \mu_0 (\omega^2 \hat{\mathbf{P}} - i\omega \hat{\mathbf{J}}) \tag{2.7}$$

To simplify the above equation, the polarization can be formally redefined to include the current density of free charges: $\hat{\mathbf{P}} - i\hat{\mathbf{J}}/\omega \to \hat{\mathbf{P}}$. This leads to a very general nonlinear wave equation:

$$\nabla^2 \hat{\mathbf{E}} - \nabla(\nabla \cdot \hat{\mathbf{E}}) + k^2 \hat{\mathbf{E}} = -\mu_0 \omega^2 \hat{\mathbf{P}} \tag{2.8}$$

where k is the wavenumber.

In this thesis, the paraxial interaction of linearly polarized light with gas is mostly considered. In this case, several basic approximations can be made to simplify the wave equation. Firstly, in the case of a transverse wave, $\nabla(\nabla \cdot \hat{\mathbf{E}}) = 0$. This remains negligible for not too tight focusing geometries (numerical aperture $\lesssim 0.3$). Secondly, linear polarization of the laser is assumed, allowing the vector equation to be transformed into a scalar equation:

$$\nabla^2 \hat{E} + k^2 \hat{E} = -\mu_0 \omega^2 \hat{P} \tag{2.9}$$

Finally, the propagation is considered to be uni-directional. The Laplace operator can be separated into a longitudinal and a transverse component: $\nabla^2 = \Delta_\perp + \partial^2/\partial z^2 = \Delta_\perp + \partial_z^2$. Using the forward and backward propagators $\partial_z \pm ik$ [26], Equation 2.9 can be factorized:

$$(\partial_z + ik)(\partial_z - ik)\hat{E} = -\Delta_\perp \hat{E} - \mu_0 \omega^2 \hat{P} \tag{2.10}$$

Neglecting the backward propagation is equivalent to the approximation $\partial_z + ik \approx 2ik$ [27].

This finally gives the well-known uni-directional propagation equation, i.e., the forward Maxwell equation [27]:

$$\left[\frac{\partial}{\partial z} - \frac{i}{2k}\Delta_\perp - ik\right]\hat{E} = \frac{i\omega^2}{2kc^2\varepsilon_0}\hat{P} \tag{2.11}$$

In the scalar and paraxial approximation, this equation can describe the propagation of linearly polarized ultrashort pulses and their linear and nonlinear interactions with gases.

2.2.1 Temporal and spectral properties

Returning to the time domain, in the absence of spatio-temporal coupling, the solution of Maxwell's equations for a laser pulse can be written as a product of a spatial function $E(x, y)$ and a temporal field equal to the product of an amplitude and a complex phase:

$$E(t) = \sqrt{I(t)}\exp\left(i\omega_0 t - i\varphi(t)\right) \tag{2.12}$$

where $I(t)$ is a time-dependent intensity, ω_0 the carrier frequency, and $\varphi(t)$ a time-dependent phase.

The spectral composition of the pulse, as a function of time, is described by the phase since the instantaneous frequency is linked to the derivative of the phase as follows:

$$\omega(t) = \omega_0 - \frac{d\varphi}{dt} \tag{2.13}$$

Therefore, a constant phase means no frequency variation in time. A linear phase leads to a frequency shift of the entire spectrum. A quadratic phase describes a linear ramp of frequency versus time, i.e., a linear chirp of the pulse. Higher orders of the phase represent a nonlinear chirp.

In the frequency domain, the field can be written as:

$$\hat{E}(\omega) = \sqrt{\hat{I}(\omega)}\exp\left(i\hat{\varphi}(\omega)\right) \tag{2.14}$$

where $\hat{I}$ is the spectral intensity and $\hat{\varphi}$ the spectral phase.

A pulse reaches its Fourier-limited pulse duration when it is compressed, i.e. when all the frequency components are in phase at a same instant. This corresponds to a flat spectral phase. When a pulse propagates through a medium, it is delayed by the absorption/re-emission of the light by the atoms. This delay is frequency dependent and will thus lead to different spectral components travelling at different speeds in the medium, lengthening the duration of the pulse. This phenomenon is called dispersion. A field propagating a distance z through a medium can be expressed:

$$\hat{E}(z) = \hat{E}(0)\exp\left(i\frac{\omega}{c}n_c(\omega)z\right) \tag{2.15}$$

where $n_c(\omega) = n(\omega) + i\alpha(\omega)$ is the complex refractive index. The real part corresponds to the refractive index, and the imaginary part to absorption.

The different orders of dispersion can be accessed through a Taylor expansion of the spectral phase around the carrier frequency of the pulse:

$$\hat{\varphi}(\omega) \approx \hat{\varphi}(\omega_0) + \frac{\partial\hat{\varphi}}{\partial\omega}(\omega_0)(\omega-\omega_0) + \frac{\partial^2\hat{\varphi}}{\partial\omega^2}(\omega_0)\frac{(\omega-\omega_0)^2}{2} + \frac{\partial^3\hat{\varphi}}{\partial\omega^3}(\omega_0)\frac{(\omega-\omega_0)^3}{6} \quad (2.16)$$

The zero order adds a constant to the phase and does not affect the shape of the pulse. The first order is called the group delay (GD):

$$\mathrm{GD} = \frac{\partial\hat{\varphi}}{\partial\omega} \quad (2.17)$$

and adds a delay to the pulse, but does not affect its shape. The second order is called the group delay dispersion (GDD):

$$\mathrm{GDD} = \frac{\partial^2\hat{\varphi}}{\partial\omega^2} \quad (2.18)$$

and introduces a frequency-dependent delay into the different spectral components. In the case of a Gaussian beam, it will generate a linear chirp, whereas in other cases, the chirp will be nonlinear. The third order is called the third order dispersion (TOD).

$$\mathrm{TOD} = \frac{\partial^3\hat{\varphi}}{\partial\omega^3} \quad (2.19)$$

2.2.2 Nonlinear effects

At high intensities, when the electric field is not negligible compared to the local fields inside the medium, the response of the atom depends on the intensity. Therefore, the temporal, spectral and spatial properties of the pulse can change during propagation. The polarization P becomes a nonlinear function of the field E:

$$P = \varepsilon_0\chi^{(1)}E + \varepsilon_0\chi^{(2)}E^2 + \varepsilon_0\chi^{(3)}E^3 + ... \quad (2.20)$$

which leads to a number of nonlinear processes that influence the amplitude and phase of the field. Harmonics of the fundamental field can be emitted since a nonlinear component of order m corresponds to an oscillation of the polarization with frequency $m\omega$ (because $[E(t)]^m \propto e^{im\omega t}$). These harmonics are implicitly described here in a perturbative picture, where it is assumed that their amplitude decreases rapidly with harmonic order, which is in strong contrast to HHG (see Chapter 4). The first nonlinear term $\chi^{(2)}$ leads to processes such as second-harmonic generation (SHG) or parametric amplification. In isotropic media, $\chi^{(2)} = 0$ and, therefore, $\chi^{(3)}$ becomes dominant, leading to effects such as the optical Kerr effect [28, 29], i.e., an intensity-dependent refractive index:

$$n(I) = n_0 + n_2 I \quad (2.21)$$

where n_0 is the linear refractive index and n_2 is the nonlinear coefficient, which is related to the third-order susceptibility according to $\chi^{(3)} = 4\varepsilon_0 c n_2 n_0^2/3$. They are both frequency dependent, and, to a good approximation, n_2 varies linearly with the density of the medium. Values for a wavelength, λ, of 800 nm, and a pressure p of

1 bar are given for a few noble gases in Table 2.1. The values for n_0 were taken or extrapolated from references [30–32], and the values for n_2 from reference [33].

The optical Kerr effect influences the pulse in many ways. First, spatially, by focusing the beam (self-focusing); second, spectrally, by causing intensity-dependent phase modulations (SPM) resulting in spectral broadening, which can be used for pulse compression, and thirdly, temporally, by reshaping it (self-steepening).

Table 2.1: Linear and nonlinear refractive indices of some noble gases for $\lambda = 800$ nm and $p = 1$ bar

	n_0	n_2 $(10^{-20}$ cm^2/W)
Helium	1.00003480	0.37
Neon	1.00006575	0.94
Argon	1.0002798	10.9
Krypton	1.0004234	24.7
Xenon	1.0006792	63.9

Self-focusing

Because of the spatial profile of the pulse, the intensity dependence of the refractive index leads to its variation across the beam profile:

$$n(r) = n_0 + n_2 I(r) \tag{2.22}$$

The refractive index becomes greater at the centre of the beam than at the edges, and this curvature acts as a focusing lens (Kerr lens) for the beam. Self-focusing was first predicted in the 1960s [34–36], and experimentally demonstrated using ruby lasers propagating in glasses and liquids [37, 38].

Self-focusing occurs when the peak power of the pulse is higher than the critical power at which Kerr lensing exactly compensates for the divergence of the beam due to diffraction [39]:

$$P_{\text{crit}} = \frac{\alpha_{\text{T}} \lambda^2}{4\pi n_0 n_2} \tag{2.23}$$

where α_{T} is the threshold parameter, a constant depending on the spatial beam shape. For a Gaussian profile, $\alpha_{\text{T}} \simeq 1.8962$.

Self-phase modulation

Because of the temporal profile of the pulse, the intensity dependence of the refractive index also leads to a time dependence of the refractive index.

$$n(t) = n_0 + n_2 I(t) \tag{2.24}$$

The variation in the refractive index with intensity creates a nonlinear time-dependent phase shift, which in turn leads to a frequency shift, i.e., new frequencies are created. Therefore, when an intense laser pulse travels through a dielectric medium or a gas, its frequency spectrum is broadened, creating new frequencies that will also shift, further broadening the spectrum, and so on. This process is quite complicated

and not easily modelled. In this section, a very simple model of SPM will be presented, which relies on significant approximations and therefore leads to results quite far from reality. However, it provides a good picture of SPM.

We assume that the laser pulse is monochromatic (which is physically impossible since a sufficiently broad spectrum is needed to support a finite pulse duration). The nonlinear time-dependent phase shift accumulated over a small propagation distance Δz can then be expressed as:

$$\phi(t) = k\Delta z = \frac{2\pi}{\lambda_0} n(t)\Delta z \tag{2.25}$$

and the instantaneous frequency can be expressed as:

$$\omega(t) = \omega_0 - \frac{\partial \phi}{\partial t} = \omega_0 - \frac{2\pi}{\lambda_0}\frac{\partial [n(t)]}{\partial t}\Delta z = \omega_0 - \frac{2\pi}{\lambda_0} n_2 \frac{\partial I}{\partial t}\Delta z \tag{2.26}$$

The time-dependent phase shift leads to a time-dependent shift of the frequency spectrum of the pulse: new frequencies appear at the positions of the greatest changes of intensity.

To simulate the frequency broadening over an interaction length L it is necessary to take into account the fact that the new frequencies created at each small step Δz will also shift and create new frequencies of their own. It is also necessary to consider other effects that may occur, such as diffraction, absorption, ionization and other nonlinear effects. These effects may affect the intensity profile of the pulse and, thus, the spectral broadening. A complete solution can be obtained by solving the wave propagation equation (Equation 2.11), which takes all nonlinear effects into account through the polarization, P. However, for this simple model, we can assume that all the new frequencies are created at the same time, at the end of the interaction, from the phase shift accumulated through the entire interaction length. We can also assume that no other effects than SPM occur, meaning that the intensity profile of the pulse remains constant throughout the whole interaction. In this case, the instantaneous frequency can be expressed as:

$$\omega(t) = \omega_0 - \frac{2\pi}{\lambda_0} n_2 \frac{\partial I}{\partial t} L \tag{2.27}$$

and the instantaneous wavelength can be deduced.

$$\lambda(t) = \lambda_0 \left(1 + \frac{n_2}{c}\frac{\partial I}{\partial t} L\right) \tag{2.28}$$

In the case of a Gaussian temporal profile, the intensity can be written as:

$$I(t) = I_0 \exp\left(-\ln 2 \frac{t^2}{\tau^2}\right) \tag{2.29}$$

where τ is the temporal full width at half maximum (FWHM). Then,

$$\frac{\partial I}{\partial t} = \frac{-2t}{\tau^2} I_0 \exp\left(\frac{-t^2}{\tau^2}\right) \tag{2.30}$$

and,

$$\lambda(t) = \lambda_0 \left[1 + \frac{n_2}{c} \left(\frac{-2t}{\tau^2} I_0 \exp\left(\frac{-t^2}{\tau^2} \right) \right) L \right] \tag{2.31}$$

Figure 2.1 shows the time-dependent wavelength shift in this simple model for a 20 fs, 3 mJ, 800 nm Gaussian pulse (typical of pulses from the laser used in the present work) propagating for 0.5 m in helium at a pressure of 2 bar, and its dependence on the intensity. It can be seen that the rising edge of the pulse is shifted to the red, and the tail to the blue. In this simple model of pure SPM, the broadening is symmetrical, and varies linearly with the intensity and the interaction length. It also varies linearly with the gas pressure, since n_2 does.

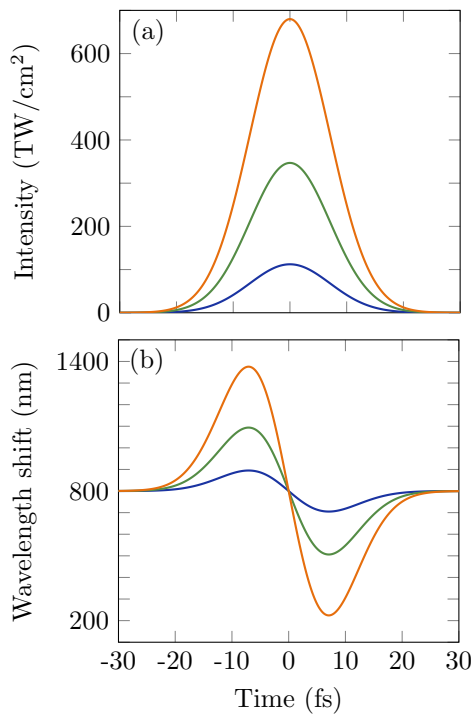

Figure 2.1: a) Temporal profile of a 20 fs, 3 mJ, 800 nm Gaussian pulse focused to a radius of $w_0 = 200$ µm (blue), $w_0 = 115$ µm (green) and $w_0 = 80$ µm (orange). b) Wavelength shift of the previous pulse induced by SPM in helium, at a pressure of 2 bar, for an interaction length, L, of 0.5 m.

Self-steepening

The intensity dependence and, therefore, the time dependence, of the refractive index leads to another nonlinear effect called self-steepening. The pulse is temporally reshaped as its phase velocity depends on intensity and, therefore, on time.

$$v_p(t) = \frac{c}{n(t)} \tag{2.32}$$

Since $n_2 > 0$, the higher the intensity, the greater the refractive index, thus, the slower the light. Therefore, the most intense part of the pulse propagates more slowly than the wings, resulting in a steep edge at the tail of the pulse. Figure 2.2 shows qualitatively the appearance of such a self-steepened pulse, and the asymmetric spectral broadening that would be created by SPM. Since the slope is gentler on the rising side and steeper at the tail, the red shift becomes smaller and the blue shift greater. Therefore, the overall spectrum is blue-shifted.

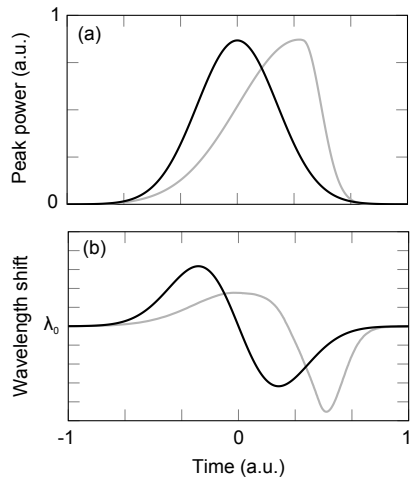

Figure 2.2: Qualitative description of self-steepening and its effect on SPM. a) Temporal profile of a Gaussian pulse (black) and of the same pulse after self-steepening (grey). b) Wavelength shift of the pulses induced by SPM. A distinct blue shift can be expected as a result of self-steepening.

Ionization

Beyond the optical Kerr effect, ionization of the medium also changes the refractive index and, therefore, the spatial, spectral and temporal properties of the pulse. At high intensity, multiphoton absorption occurs resulting in ionization (often described, for low-frequency and high-intensity light, by tunnel ionization). The probability of ionization increases strongly with increasing intensity. The ionization rate, $w_m[I(t)]$, can be calculated using a tunnel ionization model proposed by Perelomov, Popov and Terent'ev (PPT) [40–42] (see Figure 2.3a).

The ionization probability, γ, can be derived from the ionization rate (see Figure 2.3b) by integrating over the pulse duration.

$$\gamma = 1 - \exp\left(-\int_{-\infty}^{\infty} w_m[I(t)]dt\right) \tag{2.33}$$

When a medium is ionized, free electrons are released. The density of free electrons, N_e (see Figure 2.3c), depends on both the ionization probability and the gas density, ρ.

$$N_e = \rho\gamma \tag{2.34}$$

The presence of free electrons in the medium changes its refractive index (see Figure 2.3d).

$$\Delta n \approx -N_e \frac{e^2}{\varepsilon_0 m_e \omega^2} \tag{2.35}$$

where e and m_e are the charge and mass of an electron.

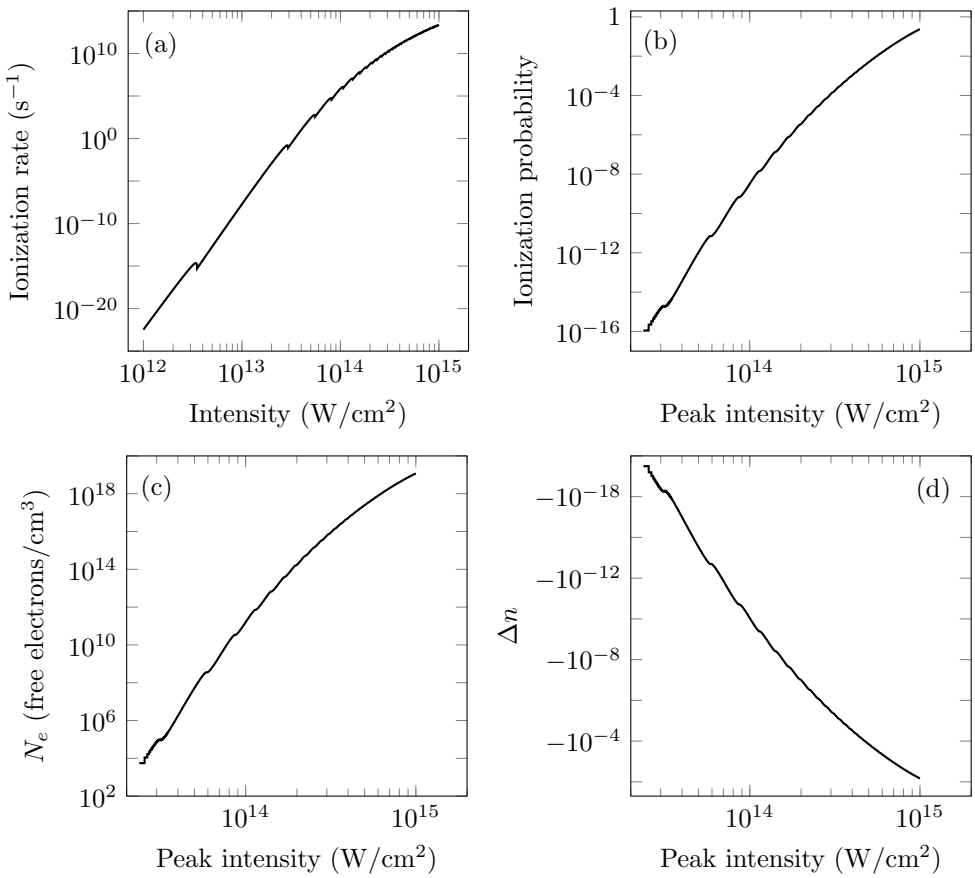

Figure 2.3: a) Ionization rate of linearly polarized light, at 800 nm, in helium, calculated using PPT theory (courtesy of Stefanos Carlström). b) Ionization probability for a 20 fs Gaussian pulse. c) Density of free electrons generated by this pulse, in helium at a pressure of 2 bar (5×10^{19} atom/cm^3). d) Shift in refractive index induced by the free electrons.

When an intense laser pulse propagates in a medium, the rising edge of the pulse rapidly increases the free electron density, leading to a rapid decrease in the refractive index. According to Equation 2.26, this will generate higher frequencies due to SPM, thus leading to a blue shift of the spectrum. Moreover, the spatial profile of the pulse creates a radially dependent shift of the refractive index. Since ionization is stronger in the centre of the beam, the refractive index becomes lower at the centre than at the edges, similarly to self-focusing, but in the opposite direction, thus acting as a defocusing lens. This phenomenon is called plasma defocusing.

2.2.3 Conclusions

To generate ultrashort pulses, one can broaden the spectrum of a longer pulse. Spectral broadening can be achieved by propagating an intense laser pulse through a dielectric medium. Unfortunately, the many effects occurring during this propagation are highly entangled and cannot be simulated separately.

If one wishes to simulate the spectral broadening to a reasonably good approximation, it is necessary to solve the propagation equation (Equation 2.11). This can be done using a method called the split-step approach [43]. This method consists of computing the solution in small steps in space or time, and treating the linear effects (e.g. dispersion) and nonlinear effects (e.g. self-focusing, SPM, self-steepening, ionization) separately. It is necessary to Fourier transform back and forth since the linear step is most easily performed in the frequency domain, and the nonlinear step, in the time domain.

However, if only an estimate of the spectral broadening is required, the B-integral, which represents the accumulated nonlinear phase, can be used.

$$B = k_0 \int n_2 I(z) dz \tag{2.36}$$

Spectral broadening through SPM can be evaluated using the spectral broadening factor, F [44].

$$F = \frac{\Delta\omega_{\text{out}}}{\Delta\omega_{\text{in}}} = \sqrt{1 + \frac{4}{3\sqrt{3}} B^2} \tag{2.37}$$

For $B > 5$, the spectral broadening factor is approximately proportional to the B-integral.

In order to achieve ultrashort pulses of sub-4 fs duration, an octave-spanning spectrum is needed. To obtain such broadening by SPM, a high intensity must be maintained over a long distance. Therefore, it is necessary to find a way of guiding the light so that the full power of the beam is concentrated on a small spatial area over a long distance.

2.3 Spectral broadening in a gas-filled, hollow-core capillary

An intuitive way to guide the light is to use a waveguide. Initially, single-mode fibres were used for spectral broadening with SPM [45]. This was successful for low energies (nJ), but as the technology of femtosecond lasers improved and higher energies became available, material damage and high-order nonlinearities prevented the use of these fibres. Hollow-core capillaries filled with a noble gas at high pressure have replaced these fibres [12]. As they allow the guiding of a mode with a large diameter, high pulse energies can be used. Nowadays, they are used routinely for spectral broadening of millijoule femtosecond pulses.

2.3.1 Propagation and losses

In a hollow-core capillary, the light is guided by grazing incidence reflections at the inner surface of the dielectric. Higher-order modes will suffer higher losses than the

fundamental mode. Therefore, after propagation through the capillary, only the fundamental mode will remain if no higher-order modes have been excited by strong nonlinearities. The lowest loss mode is the EH_{11} hybrid mode. For a capillary of inner radius $a \gg \lambda$, the intensity profile of this mode is [46]:

$$I_{EH_{11}}(r) = I_0 J_0^2 \left(2.405 \frac{r}{a}\right), \qquad r < a \tag{2.38}$$

where J_0 is the zeroth-order Bessel function of the first kind.

When the beam enters the capillary, the closer its beam profile is to this mode, the more energy will be coupled in the capillary. The coupling coefficient, H, can be calculated by performing the overlap integral between the capillary mode and the beam profile.

Typical laser pulses have a Gaussian spatial intensity profile:

$$I_{\text{Gauss}}(r) = I_0 \exp\left(-\frac{2r^2}{w_0^2}\right) \tag{2.39}$$

where w_0 is the radius of the beam at $1/e^2$ of the intensity. In this case, the highest overlap integral occurs for:

$$w_0 \simeq 0.65a \tag{2.40}$$

and leads to a coupling coefficient of $H \approx 0.98$. Figure 2.4 illustrates this coupling.

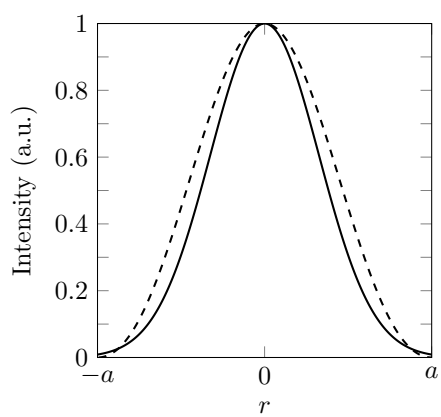

Figure 2.4: Best matching ($H \approx 0.98$) of a Gaussian profile (heavy line) to the EH_{11} hybrid mode (dashed line), the lowest loss mode of a hollow capillary.

Propagation through a hollow capillary is intrinsically lossy due to the grazing reflections. The transmission, Tr, can be expressed as:

$$Tr = \exp\left(-\alpha z\right) \tag{2.41}$$

where α is the field attenuation constant [12]:

$$\alpha = \left(\frac{2.405}{2\pi}\right)^2 \frac{\lambda^2}{a^3} \frac{\nu^2 + 1}{\sqrt{\nu^2 - 1}} \tag{2.42}$$

where ν is the ratio between the refractive indices of the external and internal media: $\nu = n_{\text{capillary}}/n_{\text{gas}}$. The total transmission will then be a product of the coupling coefficient and the transmission of the capillary (with length L):

$$Tr_{\text{tot}} = H \exp(-\alpha L) \tag{2.43}$$

Figure 2.5 shows the optimal total transmission for different capillary lengths and inner radii. The larger the inner radius, the better the transmission, however, the peak intensity in the capillary becomes lower thus reducing the nonlinear effects.

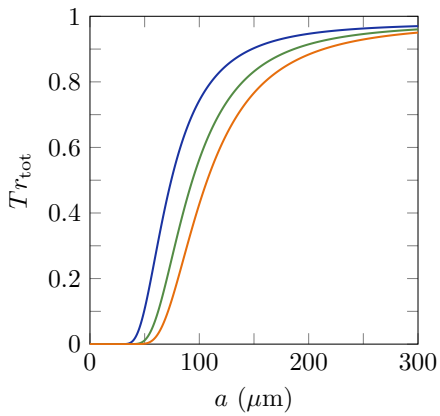

Figure 2.5: Total transmission as a function of the inner radius for 1 m (blue), 2 m (green) and 3 m (orange) long fused silica hollow capillaries filled with helium, at 800 nm, with a coupling coefficient of $H = 0.98$.

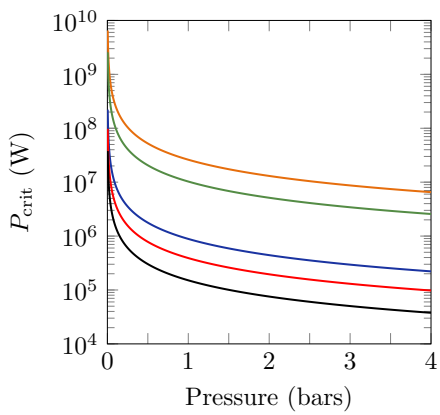

Figure 2.6: Critical peak power for self-focusing of a Gaussian beam, at 800 nm, as a function of gas pressure for xenon (black), krypton (red), argon (blue), neon (green) and helium (orange).

2.3.2 Self-focusing

In a hollow capillary, each mode travels independently and becomes attenuated at its own rate (higher-order modes are attenuated more rapidly). When self-focusing occurs, the reshaping of the pulse results in the fundamental mode being coupled to higher-order modes, leading to faster energy losses. The transmission and the spectral broadening are therefore reduced, and the quality of the beam profile can be degraded.

Figure 2.6 shows the critical power, above which self-focusing occurs (see Equation 2.23), as a function of the gas pressure for different noble gases. Self-focusing can be avoided by choosing the gas and pressure appropriately, allowing the spectral broadening and transmission to be optimized.

2.3.3 Ionization

In a hollow capillary, ionization also reshapes the pulse, exciting higher-order modes, leading to a loss of broadening and transmission. The effect of ionization in a capillary can be considered acceptable for ionization of up to 10 %.

Figure 2.7 shows that, at constant energy, the ionization probability decreases as the inner radius of the capillary increases. Therefore, ionization places a constraint on how small the inner radius can be. For a 20 fs, 3 mJ, 800 nm Gaussian pulse in helium, 10 % ionization corresponds to an inner radius of 113 μm. One way of overcoming this constraint is to use circularly polarized light as the ionization rate is lower for circularly polarized than linearly polarized light [47].

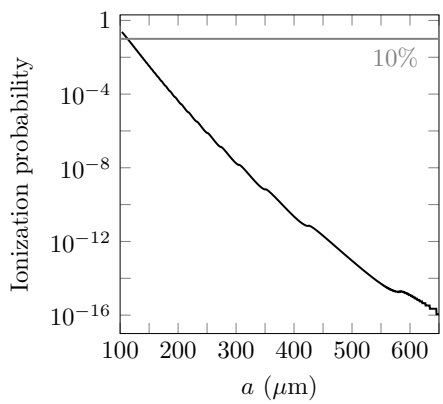

Figure 2.7: Ionization probability as a function of the inner radius, a, for a 20 fs, 3 mJ Gaussian pulse with a waist, w_0, of $0.65a$, linearly polarized, at 800 nm, in helium, calculated from the data shown in Figure 2.3.

Self-focusing and plasma defocusing are especially problematic when they occur before the pulse enters the capillary. In this case, the coupling is changed and losses are introduced. A solution to this problem is to pump the entrance of the capillary to vacuum, while adding gas at the output end. This results in a pressure gradient along the capillary. Self-focusing and ionization will then be unlikely at the entrance, but more probable at the output, where their negative effects have a lower impact on broadening and transmission. This method is called differential pumping, and has

been proven to be efficient [48]. However, it reduces the interaction length for the SPM and, therefore, longer capillaries are needed.

2.3.4 Spectral broadening

The spectral broadening achieved with a given capillary can be estimated using the B-integral formalism [49] introduced in Section 2.2.3. In the low-intensity regime, i.e., in the absence of self-focusing ($P_{\text{Laser}} < P_{\text{crit}}$), with negligible ionization (< 10 %) and homogeneous gas pressure, the accumulated nonlinear phase can be analytically evaluated from Equation 2.36:

$$B = k_0 n_2(\rho) I_0 \frac{1 - e^{-\alpha L}}{\alpha} = \frac{k_0 n_2(\rho) I_0}{\alpha} A \tag{2.44}$$

where I_0 is the intensity at the entrance of the capillary, ρ is the gas density and $A = 1 - Tr$ is the overall propagation loss in the waveguide.

For the same B-integral, thus the same broadening factor, a longer capillary with a larger inner radius will provide less linear losses.

2.3.5 Conclusions

Hollow capillaries offer a standard method for spectral broadening due to the excellent beam quality over a wide pressure range, and the excellent spectral homogeneity across the beam profile. These characteristics allow for high-quality pulse compression. The output spectrum from a capillary is especially well suited for chirped-mirror compressors. However, the alignment of a capillary is challenging and, together with the beam pointing stability, critical, as both have a considerable impact on the efficiency of the coupling and the quality of the beam profile. Moreover, longer capillaries are needed in the quest for higher power and shorter pulses, but handling them can be difficult.

2.4 Spectral broadening in a filament

Another way to guide the light, which requires a simpler experimental arrangement, is filamentation [15]. The laser beam is focused into a dielectric medium or a gas in such a way that, just after the focus, self-focusing balances the divergence of the beam. The beam is then self-guided, creating a filament.

After being focused, a beam normally expands again due to diffraction. The propagation length after which this width increases by a factor of $\sqrt{2}$ is called the Rayleigh length, and can be expressed as:

$$z_{\text{R}} = \frac{\pi n_0 w_0^2}{\lambda} \tag{2.45}$$

However, if the laser peak power reaches the critical power for self-focusing given by Equation 2.23, i.e., $P_{\text{Laser}} = P_{\text{crit}}$, the Kerr lensing effect exactly balances the divergence of the beam due to diffraction, and the beam stops diverging or converging, i.e., it is self-guided. However, this effect is not stable, and without additional effects, it will not hold for more than $10 z_{\text{R}}$.

If $P_{\text{Laser}} > P_{\text{crit}}$, self-focusing overcomes divergence, and the beam should eventually collapse on itself. The propagation length at which the beam collapses is well approximated by the semi-empirical formula [50, 51]:

$$z_{\text{cr}} = \frac{0.367 z_{\text{R}}}{\sqrt{[(P_{\text{in}}/P_{\text{crit}})^2 - 0.852]^2 - 0.0219}} \tag{2.46}$$

where P_{in} is the initial power of the pulse.

However, when the beam becomes smaller due to self-focusing, the peak intensity becomes higher and eventually, the medium is ionized. This ionization leads to plasma defocusing, preventing the beam from collapsing. The beam expands and ionization stops, but the peak power may still be high enough for self-focusing. In this case, the beam contracts until ionization occurs again. This dynamic chain process of focusing/defocusing (illustrated in Figure 2.8) provides self-guiding of the beam. The series of plasmas resulting from ionization is seen as a luminescent channel. This is called the filament. Energy losses during filamentation are minimized since the intensity is mostly maintained below the ionization threshold of the medium.

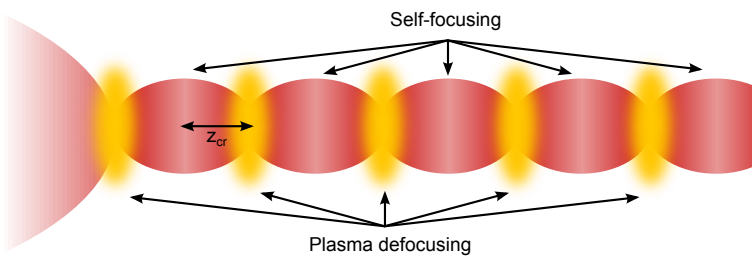

Figure 2.8: Principle of filamentation. The beam is focused into a dielectric medium or a gas. As the beam becomes smaller, the peak intensity becomes higher, and eventually ionizes the medium creating a plasma. The resulting free electrons lead to plasma defocusing and the beam expands again. Eventually, the peak intensity becomes too low to ionize the medium and self-focusing takes over, re-focusing the beam, and the process repeats itself.

On the other hand, if $P_{\text{Laser}} >> P_{\text{crit}}$, high nonlinearity can cause an initially homogeneous state to develop spatial structures; this is called modulation instability [52]. In the case of filamentation, this means that small perturbations along the transverse profile can lead to local self-focusing, which will create multiple filaments, degrading the beam profile to such extent that the beam becomes unusable for most experiments.

In practice, 4 to 10 times the critical power is needed for the filamentation process to start when a beam is focused into a gas. However, once formed, the filament only supports about 1× the critical power. The surplus power is expelled into the so-called "reservoir" (the divergent beam around the filament core) when the first plasma is formed. Therefore, filamentation usually leads to a lower efficiency than hollow capillaries.

Significant spectral broadening arises from filamentation due to the combined effects of SPM, self-steepening, ionization and plasma defocusing. The generated beam consists of a white central part surrounded by rainbow-like conical emission.

2.5 Scaling of nonlinear light–matter interactions in gases

In Paper IV, it was shown that the forward Maxwell wave equation (Equation 2.11) is scale invariant, if the spatial dimensions, gas density and pulse energy are scaled appropriately. Therefore, the phenomena it can describe, e.g., guiding in capillaries or filaments, are scale-invariant.

2.5.1 Formalism

To facilitate the understanding of scaling, it is interesting to modify Equation 2.11 by changing from the laboratory frame to a frame moving at the speed of light in vacuum [53]. It is easier to understand this transformation by studying the linear wave propagation in vacuum, i.e., when $\hat{P} = 0$ and $k = \omega/c$. Equation 2.11 then becomes:

$$\left[\frac{\partial}{\partial z} - \frac{i}{2k}\Delta_\perp - i\frac{\omega}{c}\right]\hat{E} = 0 \tag{2.47}$$

The first two terms in this equation describe wave propagation and diffraction. The third term only defines the absolute location of the spatial carrier wave with wavelength $\lambda = 2\pi c/\omega$ propagating at the speed of light. This is not important information for most optical propagation phenomena, in contrast to the carrier–envelope phase (CEP). Therefore, this term can be removed from the equation. This is done by introducing the field $\hat{\mathcal{E}} \equiv \hat{E}\exp(-i\omega z/c)$, where z is the longitudinal position in the moving frame of reference. Equation 2.47 then becomes:

$$\left[\frac{\partial}{\partial z} - \frac{i}{2k}\Delta_\perp\right]\hat{\mathcal{E}} = 0 \tag{2.48}$$

For nonlinear propagation, it is necessary to reintroduce dispersion as $k = n\omega/c$ and nonlinear polarization as $\hat{\mathcal{P}} \equiv \hat{P}\exp(-i\omega z/c)$. This gives a modified version of Equation 2.11 for a moving frame:

$$\left[\frac{\partial}{\partial z} - \frac{i}{2k}\Delta_\perp - iK\right]\hat{\mathcal{E}} = \frac{i\omega^2}{2kc^2\varepsilon_0}\hat{\mathcal{P}} \tag{2.49}$$

where $K = k - \omega/c$.

This change of frame places no limits on the spectral bandwidth, and the equation is therefore valid for any pulse duration.

2.5.2 Scalability

To show that the wave equation (Equation 2.49) is scale-invariant when the spatial dimensions, gas density and pulse energy are scaled appropriately, we can consider a field $\hat{\mathcal{E}}(r, z, \omega)$, which is a solution to Equation 2.49. A scaling parameter η is chosen. Then, we will show that $\hat{\mathcal{E}}(\eta r, \eta^2 z, \omega)$ is also a solution if the gas density is scaled as $\rho \to \rho/\eta^2$, and the pulse energy as $\epsilon_{\text{in}} \to \eta^2\epsilon_{\text{in}}$. This is done by considering how each term in Equation 2.49 reacts to scaling.

- On the left-hand side, the scaling of the first term is clear:

$$\frac{\partial}{\partial z} \to \frac{1}{\eta^2}\frac{\partial}{\partial z} \tag{2.50}$$

- For the second term, we have to consider both k and $\Delta_\perp$.
  - Firstly, it is known that $k = n\omega/c = (\sqrt{1+\chi})\omega/c$, where the susceptibility of the medium is exactly proportional to the gas density: $\chi \propto \rho$. Therefore, for $\chi \ll 1$, k does not change upon scaling:

    $$k \to k \tag{2.51}$$

    This approximation reaches its limitation at high gas densities, leading to deviations from exact scale invariance (see the supplementary material of Paper IV for more details).
  - Secondly, it is clear that:

    $$\Delta_\perp \to \frac{1}{\eta^2}\Delta_\perp \tag{2.52}$$

- For the third term, it is known that $K = k - \omega/c = (n-1)\omega/c$. For $\chi \ll 1$, $n \approx 1 + \chi/2$, thus $K \approx \chi\omega/2c$. Therefore, K varies linearly with pressure and scales as:

  $$K \to \frac{1}{\eta^2}K \tag{2.53}$$

- On the right-hand side, only $\hat{\mathcal{P}}$ will vary. However, its variation is rather complicated. The scalability must be evaluated individually for each term contributing to the nonlinear propagation phenomenon considered. Most terms vary linearly with pressure, to a good approximation, except for the term describing nonlinear absorption due to avalanche ionization (see the supplementary material of Paper IV for more details). This places a strict limit on the validity of scaling, restricting it to cases where avalanche ionization is not important in the nonlinear interaction with the medium, i.e., when ionization is generally weak (low intensity) or when avalanche ionization is weak compared to optical field ionization, e.g., for short pulses or low gas density. This scaling is valid for the parameter regime for HHG, hollow capillaries, and filamentation, used in this work. In these cases, the nonlinear polarization will vary linearly with pressure and scale as:

  $$\hat{\mathcal{P}} \to \frac{1}{\eta^2}\hat{\mathcal{P}} \tag{2.54}$$

Table 2.2: Scaling of basic parameters

	Parameter	**Scaled parameter**
Input energy	ϵ_{in}	$\eta^2\epsilon_{\text{in}}$
Output energy	ϵ_{out}	$\eta^2\epsilon_{\text{out}}$
Length	z	$\eta^2 z$
Width	r	ηr
Gas density	ρ	ρ/η^2

It can be seen that both sides of Equation 2.49 scale as $1/\eta^2$. This shows the scale invariance of the wave equation and, of course, of all the nonlinear phenomena it describes. However, one must not forget that most of the terms in $\hat{\mathcal{P}}$ are dependent

on the intensity. Therefore, for scaling to be successful, the intensity must remain constant. Since the spatial dimensions of the beam have been modified, the energy must be scaled accordingly for the intensity to remain unchanged: $\epsilon_{\text{in}} \rightarrow \eta^2 \epsilon_{\text{in}}$. Clearly, this also leads to a change in the output energy: $\epsilon_{\text{out}} \rightarrow \eta^2 \epsilon_{\text{out}}$. Table 2.2 recapitulates the scaling of the basic parameters in the wave equation.

2.6 Scaling of hollow capillaries

2.6.1 Scaling of the basic parameters

Let us consider a hollow capillary of length L, and inner radius a, filled with gas at a pressure $p \propto \rho$. The energy of the incident pulse is ϵ_{in}, leading to an output energy ϵ_{out}. This capillary fulfils the conditions for self-focusing ($P_{\text{Laser}} < P_{\text{crit}}$) and ionization ($\gamma < 10$ %). The scaling invariance of Equation 2.11 tells us that we can scale up the output energy, $\epsilon_{\text{out}} \rightarrow \eta^2 \epsilon_{\text{out}}$, and maintain the same spectral broadening if $L \rightarrow \eta^2 L$, $a \rightarrow \eta a$, $p \rightarrow p/\eta^2$ and $\epsilon_{\text{in}} \rightarrow \eta^2 \epsilon_{\text{in}}$.

We will now check that this scaled-up capillary fulfils the condition for self-focusing. Since $n_2 \propto p$, to a good approximation, the critical power for self-focusing scales as $P_{\text{crit}} \rightarrow \eta^2 P_{\text{crit}}$ (see Equation 2.23). Since the energy is scaled as $\epsilon_{\text{in}} \rightarrow \eta^2 \epsilon_{\text{in}}$, the power scales as $P_{\text{in}} \rightarrow \eta^2 P_{\text{in}}$. Therefore, the ratio $P_{\text{in}}/P_{\text{crit}}$ is conserved and the condition for self-focusing is fulfilled.

We will now check that it fulfils the condition for ionization. Since $\epsilon_{\text{in}} \rightarrow \eta^2 \epsilon_{\text{in}}$ and $a \rightarrow \eta a$, the intensity does not change and, therefore, neither does the ionization probability γ (see Equation 2.33). The ionization condition is thus also fulfilled.

The only part that does not scale is the attenuation, α (see Equation 2.42), which varies as $1/\eta^3$. Therefore, the transmission $Tr = H \exp(-\alpha L)$ will become $Tr = H \exp(-\alpha L/\eta)$, where H is the coupling coefficient which remains constant with scaling. Therefore, when scaling up a capillary, a slightly higher output energy than $\eta^2 \epsilon_{\text{out}}$ should be expected. However, the losses arising from the practical difficulties of handling a longer capillary usually outweigh this small gain.

Table 2.3: Scaling of the characteristic parameters of hollow capillaries

	Parameter	**Scaled parameter**
Input energy	ϵ_{in}	$\eta^2 \epsilon_{\text{in}}$
Output energy	ϵ_{out}	$\eta^2 \epsilon_{\text{out}}$
Length	L	$\eta^2 L$
Inner radius	a	ηa
Gas pressure	p	p/η^2
Critical power for self-focusing	P_{crit}	$\eta^2 P_{\text{crit}}$
Ionization probability	γ	γ

2.6.2 Two hollow-capillary systems

Two different hollow-capillary post-compression systems were implemented on the laser setup presented in Section 1.2.2. The first system was based on a 1 m long capillary, and the second was a scaled-up version of it, with a 2 m long capillary. Both

systems successfully delivered ultrashort, sub-4 fs NIR pulses. Figure 2.9 shows the capillary chamber for both systems, Table 2.4 lists the characteristics of these systems, and Figure 2.10 shows the results of the characterization of compressed ultrashort pulses obtained with these systems. Both systems are described thoroughly below.

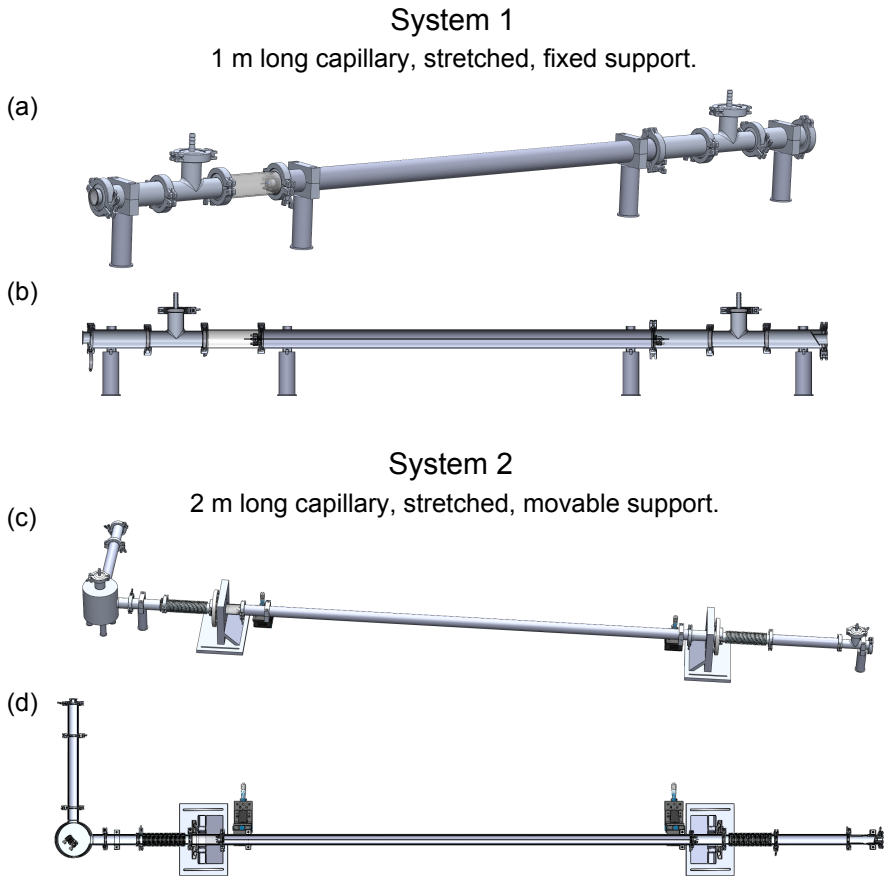

Figure 2.9: a) Global view of the first system. b) Vertical cross section of the first system. c) Global view of the second system. d) Horizontal cross section of the second system.

First system

The capillary used in the first system was a 1 m long hollow-core, rigid fused-silica capillary with an inner radius of 125 μm. The capillary was stretched to optimize the transmission of the fundamental mode (using an earlier and simpler version of the device shown in Appendix, Figure A.8). The system was differentially pumped, using a scroll pump connected to the capillary tube by a hose of diameter $\Phi = 6$ mm. The capillary tube was fixed to the table, therefore, the beam had to be aligned with the capillary by walking two mirrors. The beam was collimated after the capillary using a curved mirror of focal length 1.25 m.

Table 2.4: Characteristics of the two systems

	System 1	**Scaling of System 1** ($\eta = \sqrt{2}$)	**System 2 (low energy)**	**System 2 (higher energy)**
L	1 m	2 m	2 m	2 m
a	125 μm	177 μm	175 μm	175 μm
Gas	helium	helium	helium	helium
Pressure	3 bars	1.5 bars	3.5 bars	3 bars
ϵ_{in}	2.5 mJ	5 mJ	1.9 mJ	2.9 mJ
ϵ_{out} (in the mode only)	0.8 mJ	1.6 mJ	0.3 mJ	0.6 mJ
Efficiency	32 %	32 %	16 %	21 %
Pulse duration after compression	3.2 fs	3.2 fs	3.0 fs	4.0 fs (TOD not compensated for)
Coupling method	A curved mirror	-	An astigmatism-free telescope	An astigmatic telescope
Coupling focusing	$f = 1.5$ m (after a 2-to-1 telescope)	-	$f = 3.92$ m	$f = 3.92$ m
Coupling focus size	Not measured	-	$w_0 = 115$ μm $= 0.66a$	$w_0 = 200$ μm $= 1.14a$
Alignment method	Walking two mirrors	-	Aligning the capillary to the beam	Aligning the capillary to the beam
Pumping method	Differential pumping	-	Differential pumping	Differential pumping
Pumping hose diameter	$\Phi = 6$ mm	-	$\Phi = 6$ mm	$\Phi = 40$ mm
Problems	We could not couple in more energy while maintaining such ultrashort pulses.	-	The alignment was not very good.	The coupling focus was much too large and the output window was too close to the capillary.
Applications	Paper III	-	Paper I	Paper II

Coupling was performed using a curved mirror of focal length 1.5 m placed after a 2-to-1 telescope. The theoretical size of the focus was $w_0 = 79$ μm $= 0.63a$. The real focus must have been slightly larger due to the astigmatism introduced by the curved mirror, but this was not measured. The coupling system was placed on a breadboard with the possibility of sliding it along the optical axis so that the focus could be positioned exactly at the entrance of the capillary. The beam pointing was stabilized using a system called Aligna from TEM Messtechnik (see Appendix, Figure A.4). Day-to-day realignment of the system was not usually required. An aperture was placed in front of the entrance window of the capillary tube to tune the incoming power of the beam. This solution, although decent, was not optimal since the aperture affected the coupling.

The system was first aligned in air at low energy ($\epsilon_{\text{in}} = 81.4$ μJ) to avoid nonlinear effects. An efficiency of 78 % ($\epsilon_{\text{out}} = 63.5$ μJ) was achieved, which is close to the theoretical transmission of 85 %. The difference must have arisen from inadequacies in the coupling, mostly the shape and size of the beam profile at the entrance of the capillary.

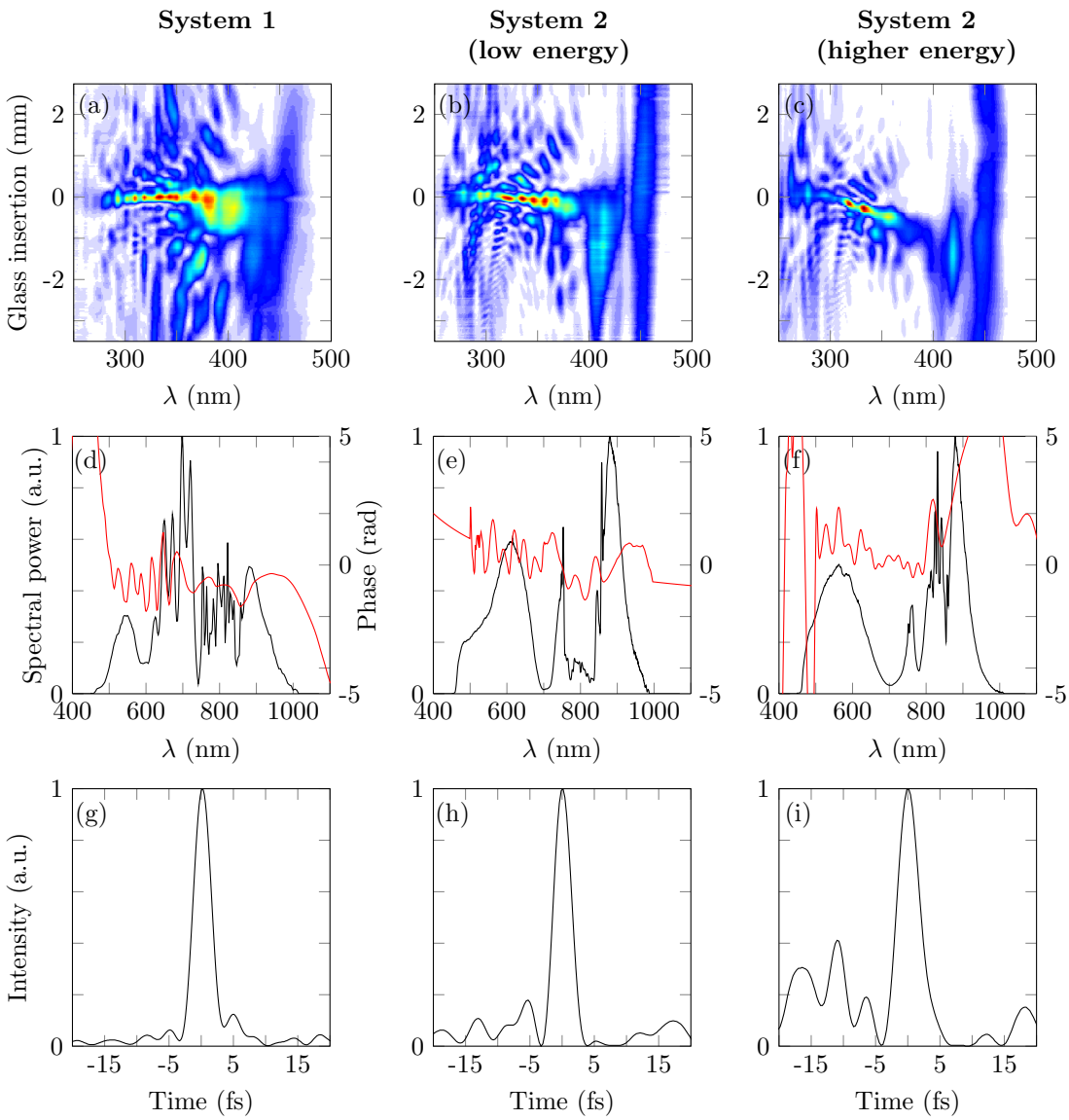

Figure 2.10: Characterization of compressed ultrashort pulses produced with the two hollow-capillary systems. In the first row, d-scans of pulses from the first system (a), the second system at low energy (b) and the second system at higher energy (c), are displayed. The third trace (c) has a greater slope because the TOD was not compensated for. In the second row, the measured spectra (black) and the retrieved spectral phases (red) of the pulses, are displayed. It can be seen that for the second system, the spectrum at higher energy (f) is blue-shifted compared to the spectrum at low energy (e). In the third row, retrieved temporal profiles of the pulses, are displayed. The last profile (i) shows stronger satellites because the TOD was not compensated for.

The system was then pumped down to vacuum, and both neon and helium were investigated for spectral broadening. The resulting broadening was much more promising with helium. After careful alignment, an energy of $\epsilon_{\text{in}} = 2.5$ mJ could be sent into the capillary, and relatively clean pulses of 3.2 fs with only small satellites were observed (see Figure 2.10). The fundamental mode was selected with an aperture, and energies of $\epsilon_{\text{out}} = 0.8$ mJ after the capillary and $\epsilon_{\text{comp}} = 0.5$ mJ after compression were measured. These pulses were used in the experiment described in Paper III.

This system was satisfactory, repeatedly providing sub-4 fs pulses with an efficiency of 32 %. However, no more than 2.5 mJ could be sent into the capillary without provoking the propagation of higher order modes, which degraded the spatial and temporal profile of the pulse.

Second system

To generate ultrashort pulses with higher energy, the previous system was scaled up. A scaling parameter $\eta = \sqrt{2}$ allows the energy to be doubled. This indicates a 2 m long capillary with an inner radius of 177 μm.

The capillary used in the second system was a 2 m long hollow-core, rigid fused-silica capillary with an inner radius of 175 μm. The capillary was also stretched (using the device described in Appendix, Figure A.8). The system was still differentially pumped using a scroll pump connected to the capillary tube by a hose of diameter $\Phi = 6$ mm. In this system, each end of the capillary tube was fixed to translation stages, in such a way that the capillary could be aligned with the beam (see Appendix, Figure A.2). The beam was collimated after the capillary, using a curved mirror of focal length 2 m.

Coupling was performed using a detuned telescope ($f_1 = 0.5$ m, $f_2 = -0.4$ m, $e_1 2 = 151$ mm), which takes into account the focusability of the beam ($M^2 = 1.24$) and corrects the astigmatism of the laser (see Appendix, Figure A.1). The coupling system was, once again, placed on a breadboard with the possibility of sliding it along the optical axis. The beam pointing was still stabilized using the Aligna system. Slight day-to-day realignment of the system was usually needed due to mechanical deformations caused by switching between gas and vacuum at the capillary exit. A half-wave plate and a polarizer were inserted in the laser system, between the last amplifier and the compressor, to fine-tune the energy of the incoming beam.

This system was much longer than the previous one, and required a much longer focal length for the coupling. Therefore, in order to place the windows at a sufficient distance from the capillary to avoid nonlinear effects in the glass, and still fit on the laboratory table, it was necessary to use folding chambers, i.e., vacuum chambers containing a mirror at 45° to fold the beam before and after the capillary. To avoid damage, a special hard reflection coating was used for the mirror in the folding chamber before the capillary. A standard silver-coated mirror was considered adequate after the capillary. However, when starting to align the capillary, it was realized that it was very difficult to aim for the output window, when using a fixed mirror in the folding chamber after the capillary, which was, of course, inaccessible when the system was under vacuum. A motorized mirror would solve this problem, but as this was deemed rather complicated to implement, it was decided, for the time being, to simply place the output window closer to the capillary.

Lower energy

When this system was first implemented, the pump laser of the last amplifier in the laser system was malfunctioning, limiting the incoming energy to 1.9 mJ. The astigmatism compensation of the detuned telescope was optimized for this particular beam, and an adequate focal size of $w_0 = 115\ \mu\text{m} = 0.66a$ was measured.

Ultrashort pulses of 3.0 fs were obtained. The energy, in the fundamental mode only, after the capillary, was 0.3 mJ. This low efficiency (16 %) was deemed to be probably due to imperfect alignment of the system. These pulses were used in the experiment described in Paper I.

Higher energy

The malfunctioning pump laser was repaired, making energies up to 5 mJ available again. However, this led to a change in the beam profile and the astigmatism, making the design of the detuned telescope obsolete, i.e., the focal size was much too large: $w_0 = 200\ \mu\text{m} = 1.14a$. Moreover, the higher energy generated a series of new problems.

Firstly, the pumping system, could not generate a sufficient vacuum in front of the capillary to prevent the formation of a filament at incoming energies over 2 mJ. The pumping hose was replaced by one with a larger diameter (40 mm). However, this led to a stiffer connection between the pump and the capillary, which led to the transfer of more vibration. To solve this problem, the hose was embedded in a bucket filled with concrete, which provided a satisfactory solution.

Secondly, it became clear that the output window was located too close to the capillary. Slight spectral broadening was already visible in vacuum, indicating that nonlinear effects were taking place in the window. When helium was added, this resulted in a blue-shift of the spectrum (see Figure 2.10f).

Finally, considering, that the focus was larger than the core of the capillary, due to the obsolete design of the focusing telescope, it was not deemed possible to inject pulses with energies above 3 mJ into the capillary, as it was feared that this could cause serious damage to the capillary.

However, it was still possible to obtain ultrashort pulses of 4.0 fs. The pulses could have been compressed to a shorter duration, by compensating for TOD, as was done on the previous cases (this will be discussed in the next chapter), however, for the particular experiment (Paper II) that was performed at the time, we could not deal with the additional glass insertion that would result from the TOD compensation. The energy, in the fundamental mode only, after the capillary, was 0.6 mJ. The low efficiency (21 %) was most likely due to the poor coupling. Scaling the first system and accounting for the size of the focus (assuming a Gaussian profile $H \approx 0.65$) give an expected transmission of 22 %.

These results are very promising, and the values predicted by the scaling of the first system should be accessible, providing a few modifications of the system. We are planning to redesign the focusing telescope to achieve an adequate focal size, and then to implement a second folding chamber with a motorized mirror. This should allow us to achieve a much better efficiency and to use the full power of the laser.

2.7 Scaling of filaments

The characteristic parameters of a filament are the critical power for self-focusing P_{crit}, the distance at which the beam collapses due to self-focusing, z_{cr}, and the ionization probability, γ. In the previous section, it was shown that the critical power scales as $P_{\mathrm{crit}} \rightarrow \eta^2 P_{\mathrm{crit}}$. The collapsing distance depends on the Rayleigh length, z_{R}, and the ratio $P_{\mathrm{in}}/P_{\mathrm{crit}}$ (see equation 2.46). For a Gaussian beam, the beam waist scales as $w_0 \rightarrow \eta w_0$, therefore, the Rayleigh length scales as $z_{\mathrm{R}} \rightarrow \eta^2 z_{\mathrm{R}}$ (see Equation 2.45). P_{in} and P_{crit} scale in the same way, so the ratio $P_{\mathrm{in}}/P_{\mathrm{crit}}$ does not change. The collapsing distance will then scale as $z_{\mathrm{cr}} \rightarrow \eta^2 z_{\mathrm{cr}}$. The intensity does not change because the power scales quadratically and the beam waist linearly. Therefore, the ionization probability does not change.

Table 2.5: Scaling of the charateristic parameters of filamentation.

	Parameter	Scaled parameter
Input energy	ϵ_{in}	$\eta^2\epsilon_{\mathrm{in}}$
Output energy	ϵ_{out}	$\eta^2\epsilon_{\mathrm{out}}$
Length	L	$\eta^2 L$
Beam waist	w_0	ηw_0
Gas pressure	p	p/η^2
Critical power for self-focusing	P_{crit}	$\eta^2 P_{crit}$
Rayleigh length	z_{R}	$\eta^2 z_{\mathrm{R}}$
Collapsing length	z_{cr}	$\eta^2 z_{cr}$
Ionization probability	γ	γ

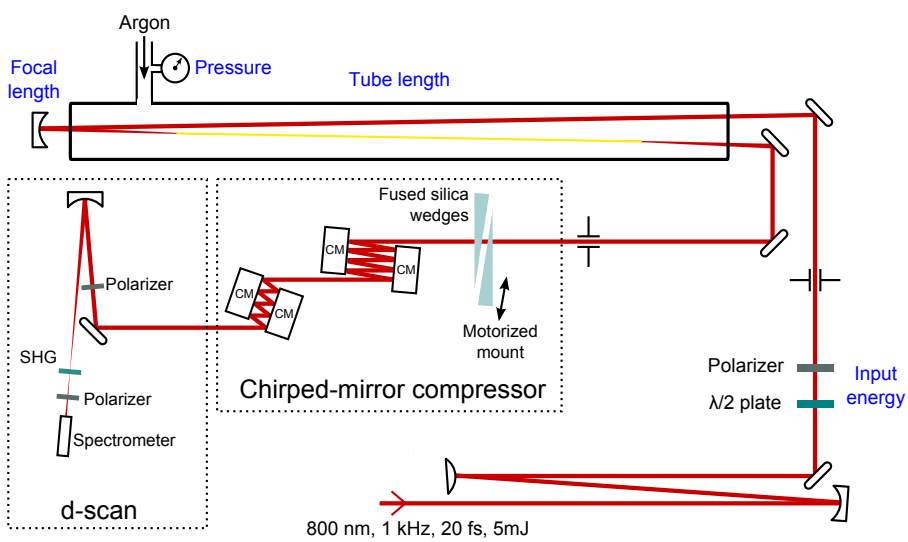

Figure 2.11: Schematic of the experimental setup used to demonstrate the scale invariance of filamentation. The parameters indicated in blue were changed upon scaling. CM: Chirped mirror. SHG: Second harmonic generation.

In the study described in Paper IV,the scale invariance of filamentation was experimentally demonstrated for input energies from 0.12 mJ to 2.7 mJ. Figure 2.11 shows the experimental setup used. Pulses from the laser were adapted to a beam diameter of approximately 11 mm, at $1/e^2$ of the intensity, using a reflective telescope. They were then focused by a spherical mirror into an argon-filled tube to create a filament. The tube was sealed with thin (0.5 mm) fused silica windows placed as far as possible from the filament itself to minimize undesirable nonlinear interactions. After the filament, the pulses were compressed using a chirped-mirror compressor together with fused silica wedges, and characterized using the d-scan technique (see Chapter 3 for details). To investigate the effects of scaling, the spatial dimensions of the beam were changed by varying the focal length of the spherical mirror, from 0.5 to 2.5 m, in six steps. Since the filament becomes longer as it is scaled up, the upper limit was defined by the available laboratory space. The gas pressure was set according to the scaling calculations and the pulse energy was fine-tuned using a half-wave plate followed by a polarizer in order to obtain similar spectra for every step.

Figure 2.12 shows the measured temporal intensity profiles, spectral powers and spectral phases for different values of the scaling parameter η. The overall pulse characteristics after post-compression, including the pulse duration, are very similar, indicating good scalability of all the linear and nonlinear propagation processes relevant in filamentation. The resulting input energies were also very close to the scaling predictions, and no upper fundamental limit was found.

2.8 Conclusions

All nonlinear processes for which the nonlinear polarization is proportional to the gas density ($\hat{P} \propto \rho$) are scale-invariant and can therefore be scaled up with no fundamental upper limit. Furthermore, this scaling formalism preserves the CEP. Scalable processes include SPM, self-focusing, wave mixing, ionization, plasma defocusing, HHG, propagation in waveguides and processes involving stimulated Raman scattering. Processes relying critically on plasma dynamics, such as avalanche ionization and the acceleration of electrons in relativistic light fields [54], are not scale-invariant, according to this theory.

This chapter described the generation of ultrashort pulses using spectral broadening in hollow-core capillaries or filaments. Moreover, it was shown that this process is scalable in energy with no fundamental upper limit. However, its experimental implementation remains challenging (see the Appendix). Although post-compression using hollow capillaries has been proven to work very well, only a few laboratories in the world can generate sub-4 fs NIR pulses on a daily basis.

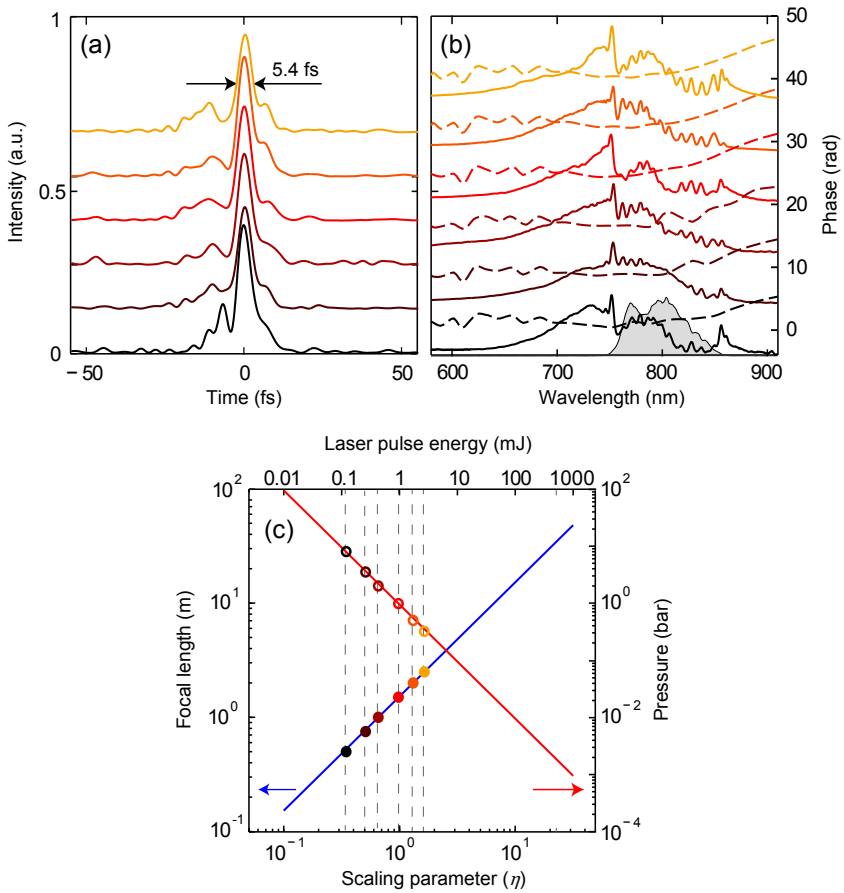

Figure 2.12: Measurements showing the scale invariance of filamentation. Measured temporal intensity profiles (a), spectral powers [(b) solid lines] and spectral phases [(b) dashed lines] for 6 different parameters set as indicated in (c) and fitted by the scaling relations (solid lines). The datasets are plotted vertically offset for clarity. The grey area in (b) shows the input spectrum. (Figure from Paper IV)

Chapter 3

Compression and characterization of ultra-broadband femtosecond pulses

3.1 Introduction

After spectral broadening, a laser pulse is usually chirped because different frequency components have travelled at different speeds, due to dispersion, and because different frequency components were created at different times during the nonlinear interaction. Because of this chirp, the pulse is not ultrashort in time. To achieve as short a pulse duration as allowed by the Fourier limit, the pulse must be compressed, i.e., all the frequency components must be in phase at a given time. To do this, it is necessary to manipulate the spectral phase. Optimal compression, i.e., Fourier-limited pulse duration, corresponds to a flat spectral phase. A particularly suitable way to compress ultra-broadband pulses created in a hollow capillary is to use a chirped-mirror compressor. Complete temporal characterization is required to determine how well compressed a pulse is. This requires measurements of both the intensity and the phase of the electric field, either in the time domain or the frequency domain.

In this chapter, the compression of ultra-broadband pulses with a chirped-mirror compressor is described. The use of the d-scan technique to fully characterize pulses in time will then be presented. Finally, the CEP measurements and stabilization in the laser system used for this work will be addressed.

3.2 Compression using a chirped-mirror compressor

3.2.1 Concept

A chirped mirror is a type of Bragg mirror, i.e., an alternating sequence of layers of two different optical materials. For conventional Bragg mirrors (Figure 3.1a), the optical thickness of all the layers is the same, and is determined by the chosen angle of incidence such that the optical path difference between the Fresnel reflections from subsequent interfaces is equal to $\lambda/2$, thus leading to constructive interference of the reflections from different pairs of layers. The reflectivity and the supported bandwidth of the mirror depend on the number of pairs of layers and the difference in refractive index between the two optical materials.

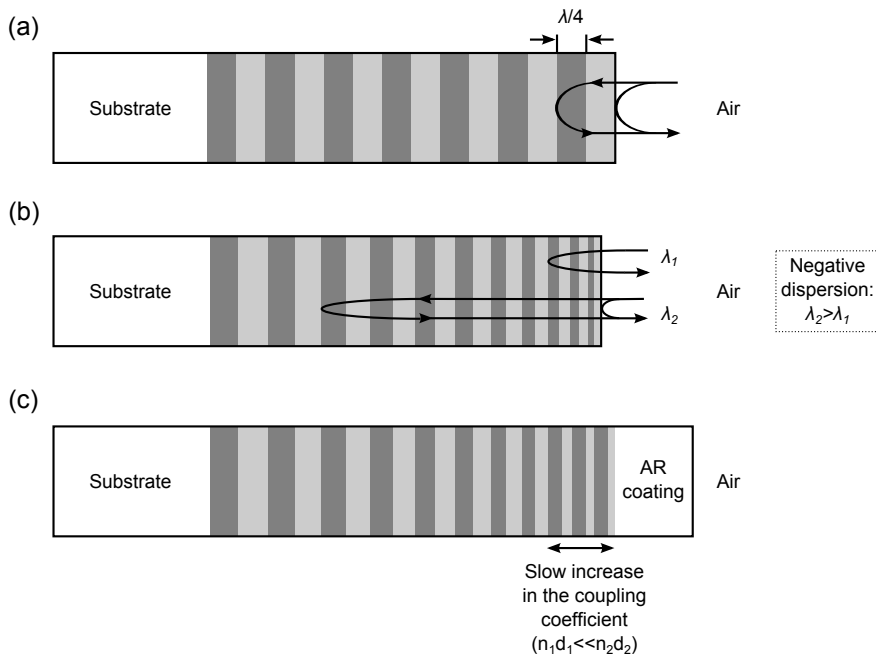

Figure 3.1: Schematic of different types of Bragg mirrors with two different optical materials with refractive indices n_1 (light grey) and n_2 (dark grey), and thickness d_1 (light grey) and d_2 (dark grey). a) Standard dielectric quarter-wave Bragg mirror with $d_1 = d_2 = \lambda/4$. b) Simple-chirped mirror where the Bragg wavelength is chirped to higher values so that longer wavelengths penetrate deeper than shorter wavelengths, generating a negative GDD. c) Double-chirped mirror. A section of slow increase in the coupling coefficient and an anti-reflection (AR) coating minimize the oscillations of the GDD.

The idea behind the chirped mirror [9] (Figure 3.1b) is to vary the thickness of the pairs of layers with depth so that different wavelengths will be reflected in different depths inside the mirror, changing the phase difference between the different spectral components. A monotonic increase in the multilayer period leads to a monotonic increase in the penetration depth with wavelength, thus creating a monotonic increase

in the GD with wavelength. This results in a negative GDD which can compensate most of the chirp of a pulse.

However, such a simple design typically generates strong oscillations of the GDD. One of the reasons for this is that the longer wavelengths have to pass through the front section of the mirror (which is designed for shorter wavelengths). Slight reflections from the front section interfere with the strong reflection from the back, creating Fabry-Perot-like resonances.

These oscillations can be minimized using a double-chirped-mirror design [10, 55] (Figure 3.1c). An anti-reflection coating is placed on top of the mirror to minimize the first reflection, and the coupling coefficient in the front section of the mirror is increased more slowly to minimize Fresnel reflections is this section.

The oscillations can be further decreased when the chirped mirrors are used in pairs. A complementary pair of mirrors, where the two different mirrors have the same GDD oscillations, but shifted by half a period, can be used. However, perfect matching of the mirrors is difficult, and some residual ripples usually remain. Another solution is to use double-angle chirped mirrors [56]. Since the incidence angle has almost no impact on the nominal GD but a great impact on the phase of the GDD oscillations, two identical mirrors can be used in combination at two different angles of incidence to minimize the GDD oscillations.

A set of chirped mirrors can be used to introduce a negative phase, which can minimize the chirp of the pulse. A different amount of GDD will be introduced depending on how many times the beam is reflected from the chirped mirrors. Therefore, a chirped pulse can be compressed by choosing the appropriate number of reflections. However, this approach is clearly discrete, and to achieve optimal compression, fine-tuning of the GDD is needed. The number of reflections is chosen so that the nominal GDD of the beam after the chirped mirrors is negative, and additional tunable dispersion is inserted into the beam path using, for example, a motorized glass wedge (tunable glass insertion).

This technique is very efficient but perfect pulse compression, i.e. Fourier limited pulse duration, is unlikely, since higher order chirp can usually not be compensated for. However, negative TOD can be compensated for by inserting a material with a lower GVD/TOD ratio than that used to fine-tune the GDD into the beam path, where GVD is the GDD per unit length, e.g., [57]. By adding some of the new material and removing some of the other, TOD can be added for a certain value of GDD.

3.2.2 Design of a chirped-mirror compressor for a hollow capillary post-compression system

In a chirped-mirror compressor, the beam must be collimated and linearly polarized in the direction required by the specific chirped mirrors. Therefore, the divergent beam exiting a capillary must be collimated using, for example, a silver-coated curved mirror at a low angle of incidence. Moreover, the polarization may have to be rotated.

The same compressor was used for all the capillary systems described in Section 2.6.2 (with minor differences on how to compensate for TOD). The compressor is shown in Figure 3.2. It consists of two pairs of double-chirped mirrors in double-angle configuration (PC70, Ultrafast Innovations). Two pairs of mirror were used to allow two mirrors with the same angle of incidence to face each other, allowing several reflections from each mirror, making the system more compact. The spectral range of

the chirped mirrors extends from 500 nm to 1050 nm with a nominal GDD of -40 fs^2. Two fused silica wedges were used for fine-tuning of the dispersion. One wedge is fixed to add a dispersion offset, and the other is on a motorized mount so it can be moved in and out to vary the glass thickness in the beam path.

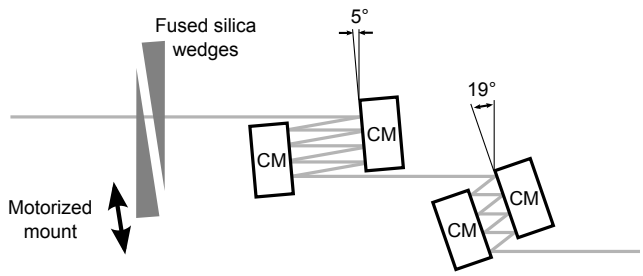

Figure 3.2: Schematic of the chirped-mirror compressor used for the hollow-capillary post-compression systems. Two pairs of double-chirped mirrors (CM) were used in double-angle configuration. The first mirror of each pair is placed at an incidence angle of 5°, both mirrors facing each other, and the second of each pair at 19°. This allowed several reflections on each mirror. A pair of fused silica wedges was used for fine-tuning of the dispersion, one was fixed and the other was motorized so that the insertion could be fine-tuned.

The first step in designing such a compressor is to choose the necessary number of reflections from the chirped mirrors. It is necessary to know the approximate targeted GDD, and then somewhat over-compensate for it so that wedges can be added for fine-tuning. A total of 16 reflections, 4 reflections from each mirror, leading to a GDD of -640 fs^2, was chosen.

The second step is to set the appropriate angles of incidence on each pair of mirrors to minimize the GDD oscillations. The angles are given in the specifications of the chirped mirrors, in this case, 5° and 19°. To verify the specified values and analyse the sensitivity of the GDD fluctuations to the angles of incidence, a chirped mirror was characterized by measuring its GD for different angles using a white light interferometer (see Figure 3.3). In the interferometer, unaltered white light interferes with the white light reflected from the chirped mirror at a tunable angle θ. The GD induced by the chirped mirror can be extracted from the interference fringes [58, 59]. The GDD can then be obtained by differentiating the GD with respect to angular frequency.

In a double-angle configuration, the GDD oscillations of one mirror are in phase opposition with the GDD oscillations of the other, thus minimizing them. To study this compensation, the mean GDD of the GDDs for different pairs of angles of incidence was calculated. Figure 3.4 shows the GD and GDD of mirrors at 5° and 19° together with the mean GD and GDD of the pair. It can be seen that the oscillations are in phase opposition, leading to a considerable reduction in the GDD oscillations. The mean value of the resulting GDD together with its root mean square (RMS) are given in Table 3.1. The specified angles of 5° and 19° are indeed the angles leading to the smallest GDD oscillations (lowest RMS value) and the mean value is close to the specified value of -40 fs^2.

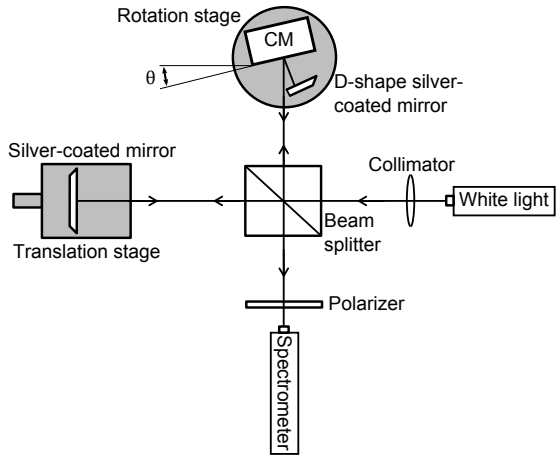

Figure 3.3: Schematic of the white light interferometer used to measure the dispersion of a chirped mirror. A tungsten lamp generates white light which is split by a beam splitter. In one arm, the chirped mirror (CM) is placed on a rotation stage to allow the dispersion to be measured at different angles of incidence, θ. The length of the other arm is adjustable to compensate for the dispersion of the chirped mirror. The light from both arms is recombined in the beam splitter and sent to a spectrometer. A polarizer is used to extract only the polarization of interest.

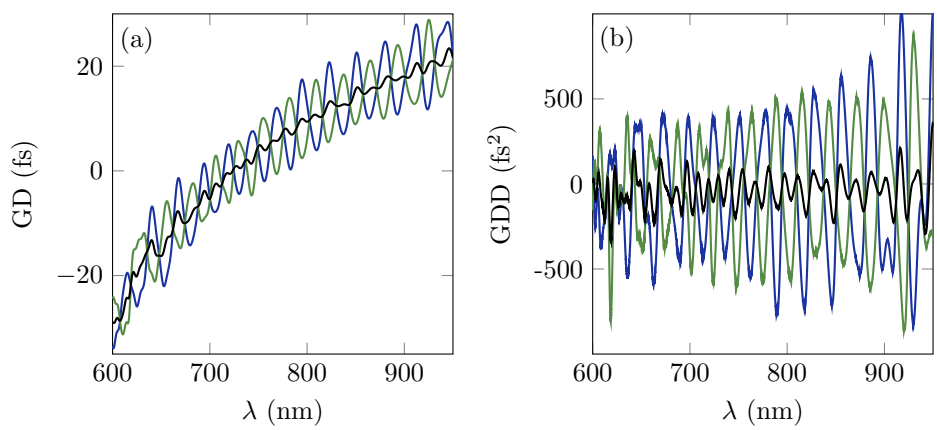

Figure 3.4: Measured GD (a) and GDD (b) of a chirped mirror, with angles of incidence of 5° (blue) and 19° (green), and the calculated, mean GD and GDD of the pair (black).

The final step is to align the compressor. The chirped mirrors are placed at approximately the correct angles, and the angles are then fine-tuned by minimizing the oscillations of the total GDD. The oscillations of the GDD can be observed by performing a d-scan, as described in the next section. When doing this, it is useful to have pulses with a clean spectral phase, i.e., no orders higher than the GDD, quite a broad bandwidth, and low energy. Such pulses are available directly from the oscillator of our laser system. They have an energy of 2 nJ at 800 nm and a bandwidth greater

than 300 nm. The compressor can be aligned on a breadboard using these pulses, and then carefully moved to its final position.

Table 3.1: RMS values (black) and mean values (grey), in fs^2, of the mean GDD of a pair of mirrors over the spectral range 600 nm to 950 nm for different pairs of angles of incidence

Mirror 2 \ Mirror 1	3°	4°	5°	6°	7°
17°	133 (-43.3)	153 (-45.1)	146 (-44.6)	158 (-41.9)	167 (-42.2)
18°	116 (-41.8)	119 (-43.6)	116 (-43.1)	133 (-40.3)	158 (-40.7)
19°	107 (-42.2)	113 (-44.1)	104 (-43.5)	121 (-40.8)	136 (-41.1)
20°	150 (-44.4)	131 (-46.2)	140 (-45.7)	124 (-42.9)	141 (-43.3)
21°	153 (-45.5)	146 (-47.3)	142 (-46.8)	131 (-44.1)	144 (-44.4)

When characterizing the pulses from the capillary systems used in this work, a systematic negative TOD was observed. The TOD increases the duration of the main pulse and creates several pre-pulses, which remove a significant amount of energy from the main pulse. This can be observed in the third column of Figure 2.10. The TOD probably arises from SPM or poor matching of the chirped mirrors due to alignment or fluctuations in manufacturing. To compensate for this, it was necessary to find a material with a lower GVD/TOD ratio than fused silica (< 1.3 fs^{-1}). Adding the correct amount of this material will then compensate for the measured TOD. The amount of fused silica is then reduced by moving the wedges to obtain optimal compression. The first material we found to have a satisfactory GVD/TOD ratio was water [57], with a ratio of 0.7 fs^{-1}. A water cell was used for compression of the pulses from the first capillary system. The results were satisfactory (as can be seen in the first column of Figure 2.10). However, the water has to be contained requiring the introduction of glass windows into the beam path. Furthermore, strong thermal effect are generated in water, it evaporates, and may be subject to contamination due to the growth of organisms, all of which may lead to a poor beam profile and reduction of the transmission with time. A solid material, namely a z-cut potassium dihydrogenphosphate (KDP) crystal, where the light travels with polarization on the ordinary axis (as opposed to the KDP crystals normally used for nonlinear optics), was found to be more suitable. Its GVD/TOD ratio is 0.65 fs^{-1}. This KDP crystal was used for compression of the pulses from the second capillary system (described above). The results were also satisfactory, and can be seen in the second column of Figure 2.10.

3.3 Temporal characterization using the d-scan technique

Temporal characterization of ultrashort pulses is necessary to understand and further develop both ultrashort pulse generation techniques and experiments using these

pulses. Firstly, it allows the verification of theoretical models of pulse generation, the identification of current limitations, and the development of techniques to create even shorter pulses. Secondly, it provides critical information that can be used to determine the temporal resolution of an experiment, as well as the outcome, for example, the impact of chirp. Finally, it opens up possibilities to shape the pulse in time to better meet the needs of a particular experiment.

A great deal of work has been devoted to the characterization of ultrashort pulses over recent decades [60]. Techniques such as frequency-resolved optical gating (FROG) [61–63], spectral phase interferometry for direct electric field reconstruction (SPIDER) [64] and their multiple variants (see, e.g. [65–68]), allow measurements of the spectral phase and intensity of the pulse.

FROG is based on spectrally resolved autocorrelation. A pulse and its temporally delayed replica are noncollinearly focused into a nonlinear crystal. The time delay is scanned, and the spectrum resulting from the nonlinear interaction is measured, as a function of the delay, with a spectrometer. The intensity and phase of the pulse can then be retrieved using, for example, an algorithm based on general projections [69] (see Figure 3.5). An optimized algorithm can perform a retrieval under one second. Moreover, redundancy in the measurement allow to verify the validity of the information retrieved. If the spectrometer measures N points in frequency, the information retrieved will consist of two vectors of N points: the spectral power and the spectral phase, as a function of frequency. However, if M delay points are scanned, the FROG trace will consist of $N \times M$ points. Therefore, the result of the retrieval can be cross-checked by comparing it to the redundant information in the measurement. FROG measurements are easy to perform and yield a robust retrieval. Complex pulses from the mid-IR to the XUV can be characterized.

SPIDER is another nonlinear self-referencing technique. It is based on spectral shearing interferometry. A pulse followed by its temporally delayed replica, on one arm, and a spectrally stretched replica, on the other, are sent into a nonlinear crystal for SHG, creating a pulse followed by its spectrally shifted replica. The two pulses interfere in a spectrometer. The spectral phase can be retrieved from the spectral interferogram using a direct (noniterative) routine requiring only two one-dimensional Fourier transforms. The retrieval is fast, easy and robust. SPIDER requires no moving components and is an inherently single-shot technique.

FROG and SPIDER allow robust measurements of the phase and amplitude of the pulse. However, to obtain pulses with Fourier-limited duration, an external compression of the pulse is necessary. A different approach is adopted in other techniques, such as multiphoton intrapulse interference phase scan (MIIPS) [70], chirp scan [71], and d-scan [17], where simultaneous measurement and compression of the pulse are performed. A controlled spectral phase is added to the pulse and the second harmonic spectrum is measured with a spectrometer. Different spectral phases are scanned, and the best compression of the pulse corresponds to the spectral phase that best compensate for the original spectral phase of the pulse.

MIIPS uses a pulse shaper to add a controlled spectral phase. A scan is performed and an approximate spectral phase corresponding to the highest second-harmonic signal is retrieved. The pulse shaper compresses the original pulse using this information and a new scan is performed giving a better approximation of the spectral phase. After 3 to 5 iterations, a flat spectral phase is obtained, and the original spectral phase corresponds to the opposite of the added spectral phase.

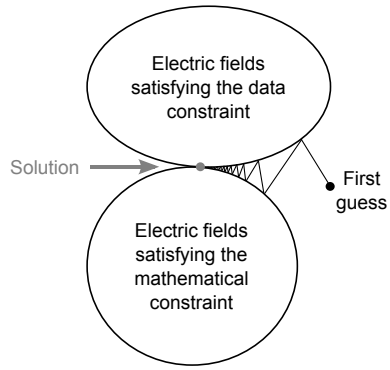

Figure 3.5: Illustration of a FROG algorithm based on general projections. Of all the possible electric fields, there exists only one that satisfies the following two constraints: 1) the electric field has the correct spectral intensity, I_{FROG}, to match the FROG trace, called the data constraint, and 2) the electric field as a function of the time delay, Δt, can be expressed using the mathematical form of the nonlinear interaction used (e.g., for SHG $E_{\mathrm{sig}}(t, \Delta t) = E(t)E(t - \Delta t)$), called the mathematical constraint. First, an electric field $E = E_0 e^{i\varphi}$ is guessed. This field is then projected onto the set of electric fields that verifies the data constraint, i.e., $E' = \sqrt{I_{\mathrm{FROG}}} e^{i\varphi}$. This new field is then projected onto the set of electric fields that verifies the mathematical constraint. This process is repeated iteratively until the field converges to the solution, i.e., when the error between the field satisfying the mathematical constraint and that satisfying the data constraint reaches a target value.

The d-scan technique is based on the MIIPS concept of applying a controlled spectral phase to the pulse, but the method of retrieval is different. An iterative numerical algorithm is used to precisely retrieve the spectral phase from a single scan. The setup is compact, simple to implement, and provides robust and precise measurements. Furthermore, the recorded d-scan traces are intuitive and easy to interpret, even without retrieval.

3.3.1 The d-scan technique

Concept

A controlled spectral phase is applied to the pulse by inserting a linearly varying amount of material in the beam path. In this way, the scanned spectral phase is simply the phase introduced by propagation through the material: $\hat{\varphi}(\omega, z) = zk(\omega)$, where $k(\omega)$ is the wavenumber of the material, i.e., the frequency-dependent phase of the material per unit length, and z is the thickness of the material (absorption in the material is considered negligible).

The electric field of the pulse to be measured can be written in frequency space as a product of an amplitude and a phase: $\hat{E}(\omega) = |\hat{E}(\omega)| e^{i\hat{\varphi}(\omega)}$. After propagating through the material, its spectral phase is changed.

$$\hat{E}_2(\omega, z) = |\hat{E}(\omega)| e^{i\hat{\varphi}(\omega)} e^{izk(\omega)} \tag{3.1}$$

In order to compare the pulse to itself, a nonlinear interaction must take place. For the d-scan technique, SHG was chosen. If instantaneous and frequency-independent

nonlinearity is assumed, then SHG can be modelled by taking the square of the field in the time domain.

$$E_3(t,z) = E_2(t,z)^2 = \left(\mathcal{F}^{-1}[\hat{E}_2(\omega,z)]\right)^2 = \left(\int_{-\infty}^{\infty} |\hat{E}(\omega)| e^{i\hat{\varphi}(\omega)} e^{izk(\omega)} e^{i\omega t} d\omega\right)^2 \quad (3.2)$$

This assumption is not valid in the depletion regime. Therefore, a moderate energy should be used in d-scan measurements.

Finally, the spectral intensity is measured with a fibre spectrometer, and can be expressed as a function of the original field.

$$\hat{I}_{\text{ideal}}(\omega,z) = |\mathcal{F}[E_3(t,z)]|^2 = \left|\int_{-\infty}^{\infty} \left(\int_{-\infty}^{\infty} |\hat{E}(\Omega)| e^{i\hat{\varphi}(\Omega)} e^{izk(\Omega)} e^{i\Omega t} d\Omega\right)^2 e^{-i\omega t} dt\right|^2 \quad (3.3)$$

where $\hat{I}_{\text{ideal}}$ is the spectral intensity measured when SHG follows the simple model of Equation 3.2.

For ultra-broadband, few-cycle pulses, the second-harmonic signal may not follow this simple model, due to fundamental reasons, e.g., the bandwidth within which the phase matching is preserved and the frequency dependency of the SHG process; or technical reasons, e.g., possible contamination by the fundamental spectrum (in the case of an octave spanning spectrum), the calibration of the spectrometer, etc. A good approximation of the second-harmonic signal is obtained by multiplying Equation 3.3 by an appropriate spectral filter $\hat{R}(\omega)$:

$$\hat{I}_{\text{meas}}(\omega,z) = \hat{R}(\omega)\hat{I}_{\text{ideal}}(\omega,z) \quad (3.4)$$

Calibration of the d-scan allows the determination of $\hat{R}(\omega)$ (as explained below). The phase and intensity of the pulses can then be retrieved from the measured d-scan traces, i.e., 2D scans consisting of the second-harmonic spectra as a function of the thickness of material inserted (examples are shown in Figure 3.6).

Retrieval

MIIPS analysis could be used to retrieve the spectral phase. However, an iterative phase correction, which would lead to a more precise measurement, is not possible in the absence of a pulse shaper. Therefore, algorithms able to retrieve the spectral phase from a single d-scan trace were developed.

The first is an iterative algorithm that uses an accurately measured fundamental spectrum to deduce the spectral intensity, and then finds the spectral phase that best recreates the measured scan. This can be treated as a general multi-dimensional optimization problem. The spectral phase is described by a set of parameters. This can be done, for example, by decomposing the phase into a Fourier series basis in order to minimize the number of dimensions and the coupling between the different functions (to avoid convergence to local minima) [73] or, by using a grid of equally spaced control points (the phase is the interpolation of these points) which number is arbitrarily chosen, and increased if the algorithm converge to a local minimum [17]. The parameters are then iteratively optimized to minimize an error between the measured scan, $\hat{I}_{\text{meas}}$, and the simulated scan, $\hat{I}_{\text{sim}}$. The error, G, is a merit function

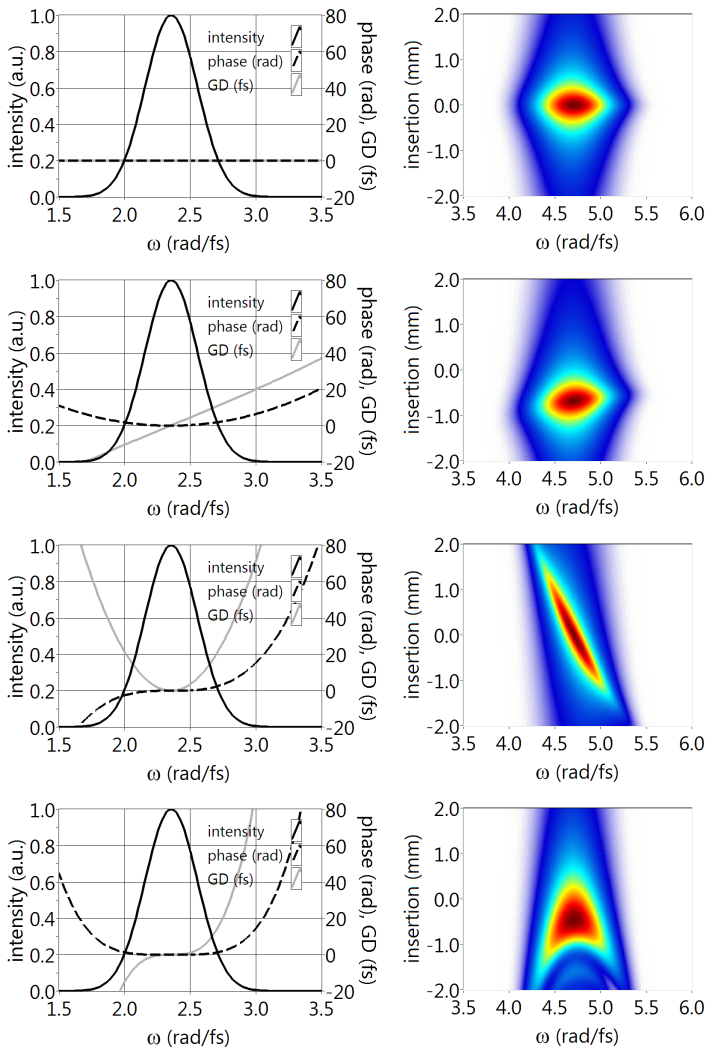

Figure 3.6: Simulated d-scan traces for some representative spectra with different spectral phases. The Fourier-limited spectrum has a FWHM of 6 fs. (Figure provided by Miguel Miranda [72]).

corresponding to the RMS error commonly used in FROG:

$$G = \sqrt{\frac{1}{N_i N_j} \sum_{i,j} \left(\hat{I}_{\text{meas}}(\omega_i, z_j) - \mu \hat{I}_{\text{sim}}(\omega_i, z_j) \right)^2} \tag{3.5}$$

where N_i and N_j are the number of frequency and material insertion points, respectively. Only the relative spectral intensity is retrieved, therefore, in order to minimize the error, the factor μ is used, and must be updated at each iteration. Differentiating

the error with respect to μ, gives:

$$\mu = \frac{\sum_{i,j} \hat{I}_{\mathrm{meas}}(\omega_i, z_j)\hat{I}_{\mathrm{sim}}(\omega_i, z_j)}{\sum_{i,j} \hat{I}_{\mathrm{sim}}(\omega_i, z_j)^2} \tag{3.6}$$

This algorithm is very robust and, in some cases, can still work well even when the second-harmonic signal is not phase-matched at some frequencies or simply absent. This is due to the fact that, for ultra-broadband pulses, SHG is more like sum-frequency generation. Therefore, all the frequency components generated depend, to some degree, on the generating frequency components, i.e., the fundamental spectrum, creating a redundancy of information. However, it is not easy to formulate a mathematically strict criterion to quantify the necessary bandwidth for a correct retrieval.

A variation of the algorithm has been presented, allowing retrieval of the spectral intensity from the d-scan trace, relaxing the need for a separate measurement of the fundamental spectrum [71]. However, the spectral response of the system must be known, i.e., the system must first be calibrated using the original algorithm (as explained below). Moreover, appropriate phase matching is needed and a signal must be present at all frequencies.

The second algorithm, presented in Paper I, is an iterative retrieval algorithm similar to FROG and ptychographic algorithms. The concept is similar to FROG: the algorithm iterates between a data constraint and a mathematical constraint (see Figure 3.5). As a first guess, the spectral intensity profile is assumed to be Gaussian with a width estimated from the d-scan trace, and the spectral phase is approximated by a MIIPS analysis. From this guess, a complex d-scan trace is calculated by taking into account the phase induced by the material, and the SHG process. The spectral amplitude is then substituted by the measured one, but the spectral phase is kept (data constraint step). To obtain a better guess of the phase, the field is multiplied, in the time domain, by the complex conjugate of the original guess, i.e., the field before the d-scan trace was calculated (this is the part of the algorithm based on ptychography). The amplitude, modified by the last step, is then corrected, by taking its cube root. Finally, in the frequency domain, the phase from the material is removed, and a new guess for the field is obtained by averaging over the different material insertions. This loop is repeated until the error given in Equation 3.5 reaches a target value.

The second algorithm allows the retrieval of calibrated traces without a measured fundamental spectrum. This algorithm is much faster than the first algorithm but retrieval is less robust in the case of noisy scans. A variant of the second algorithm, using a measured fundamental spectrum in the same way as the first algorithm, provides robust phase retrieval from non-calibrated traces. If the fundamental spectrum is not available, a composite algorithm can be used. The spectral phase is retrieved using the second algorithm (phase retrieval is reasonably accurate, even for noisy traces) and the spectral intensity is optimized using the first algorithm. This results in considerably better phase retrieval from noisy scans, and it is still faster than using only the first algorithm.

Calibration

Since the overall error is used as a merit function, it is crucial to calibrate the signal accurately, i.e., to calculate $\hat{R}(\omega)$. A first approximation can be obtained using the frequency marginal i.e. by integrating the second-harmonic signal along z:

$$\hat{M}_{\mathrm{meas}}(\omega) = \int_{-L}^{L} \hat{I}_{\mathrm{meas}}(\omega, z) dz \tag{3.7}$$

where $-L$ is the minimum material insertion and L the maximum. For sufficiently large L, this quantity does not depend on the spectral phase (as shown in the appendix of Paper I), thus, comparing $\hat{M}_{\mathrm{meas}}$ to $\hat{M}_{\mathrm{sim}}$ for a Fourier-limited pulse allows the calculation of $\hat{R}(\omega)$.

Using this first approximation together with the measured fundamental spectrum allows the precise calculation of $\hat{R}(\omega)$ by defining μ for each frequency during the retrieval of a d-scan trace:

$$G = \sqrt{\frac{1}{N_i N_j} \sum_{i,j} \left(\hat{I}_{\mathrm{meas}}(\omega_i, z_j) - \mu_i \hat{I}_{\mathrm{sim}}(\omega_i, z_j) \right)^2} \tag{3.8}$$

and

$$\mu_i = \frac{\sum_j \hat{I}_{\mathrm{meas}}(\omega_i, z_j) \hat{I}_{\mathrm{sim}}(\omega_i, z_j)}{\sum_j \hat{I}_{\mathrm{sim}}(\omega_i, z_j)^2} \tag{3.9}$$

If the retrieval is successful, μ_i gives the complete spectral response:

$$\hat{R}(\omega_i) = \mu_i \tag{3.10}$$

which can be used to calibrate the next trace that will be retrieved.

Experimental implementation

Figure 3.7 shows an experimental implementation of the d-scan technique. The chirp of the pulse is over-compensated using a chirped-mirror compressor, which adds a constant negative GDD to the spectral phase. Two fused silica wedges adding positive GDD are used to finely compensate for the chirp. One wedge is fixed on a motorized stage so that the wedge can be moved in and out to linearly vary the amount of glass in the beam path. The beam is then focused into a KDP crystal for SHG. Since the second harmonic is generated polarized at 90° from the fundamental, the residual fundamental field, which generates background noise during the measurement, can be suppressed with a polarizer. Another polarizer is placed before the SHG crystal to ensure that the fundamental field is completely linearly polarized. Finally, the spectral power is measured with a fibre spectrometer. A computer controls the insertion of the wedge and performs phase and intensity retrieval.

One of the striking advantages of the d-scan technique is that most of the components required, i.e., the glass wedges and the chirped mirrors, are already present in a typical pulse post-compression setup.

Some experimental d-scan traces are presented in Figure 2.10. Traces (a) and (b) are similar to the first trace in Figure 3.6, and show pulses compressed very close to the

Fourier limit, while (c) shows a tilt similar to the third trace in Figure 3.6, indicating TOD. Retrieval of traces (a) and (c) was performed using the first algorithm, and retrieval of trace (b) using the second algorithm.

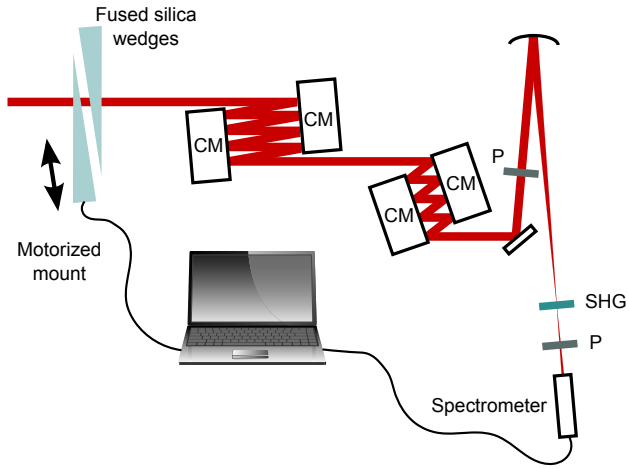

Figure 3.7: Experimental setup including a chirped-mirror compressor and a d-scan apparatus. One of the wedges is controlled by the computer to scan the glass insertion, and the second-harmonic signal is recorded at each step by a fibre spectrometer. CM: chirped mirror, P: polarizer.

3.3.2 Single-shot d-scan

Multi-shot pulse characterization techniques are often sufficient. However, for low repetition-rate sources, these may take an inconveniently long time, or even yield meaningless results if there are significant shot-to-shot fluctuations. It is therefore sometimes necessary to use single-shot techniques that can characterize individual pulses. Moreover, such measurements allow instant feedback, which can be very useful during the alignment and optimization of a system.

Single-shot versions of FROG have existed since its introduction [74], and SPIDER is inherently a single-shot technique. However, single-shot versions of the d-scan technique for few-cycle pulses [75] and longer (10 to 70 fs) [76] were demonstrated only recently. Paper II presents a novel, patent-pending, compact, single-shot d-scan setup that allows robust measurements of few-cycle pulses.

In order to apply the d-scan technique to single-shot measurements, the same trace, i.e., the second-harmonic spectrum as a function of glass insertion, must be obtained without any moving parts. The main idea is that if the beam is sufficiently homogeneous, one can make different parts of the beam go through different thicknesses of glass and then measure the second-harmonic spectrum of each part simultaneously, thus obtaining the desired trace.

Figure 3.8 shows the experimental implementation of the single-shot d-scan setup presented in Paper II. The pulses are first compressed using a chirped-mirror compressor and two wedges. The beam is then expanded by a factor 6 with a telescope,

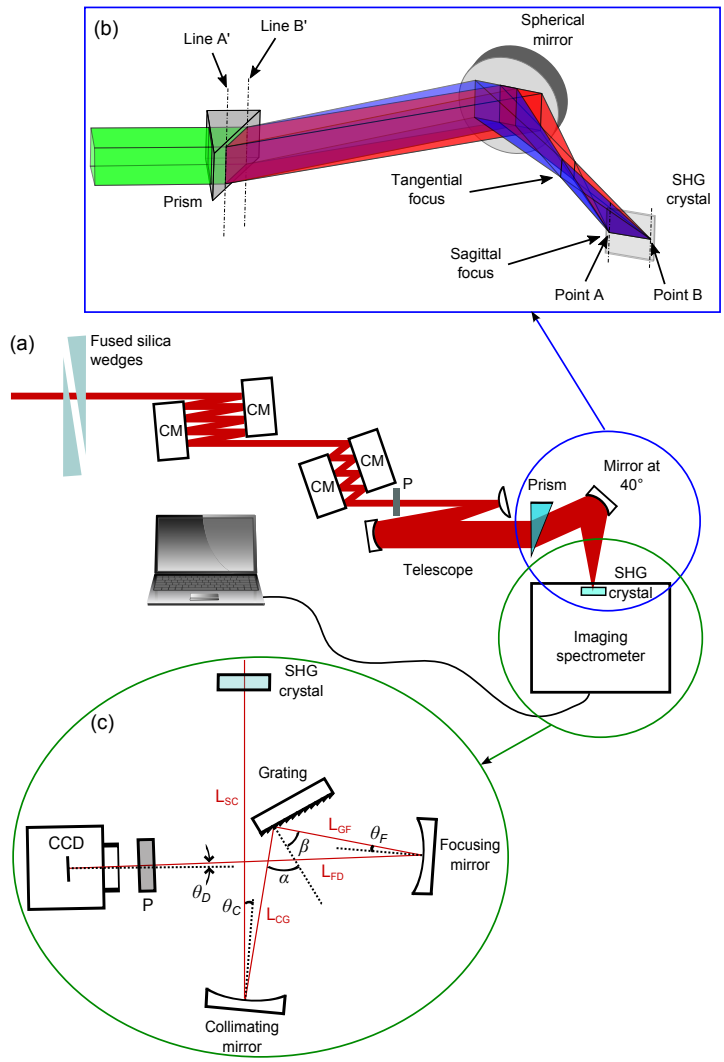

Figure 3.8: a) Schematic of the complete setup for single-shot d-scans. CM: chirped mirror, P: polarizer. b) 3D schematic of the setup used to generate SHG as a function of glass insertion. The off-axis geometry leads to different focusing in the vertical and horizontal planes, resulting in focusing in one plane and imaging in the other, in the SHG crystal. Lines A' and B', on the exit face of the prism, are imaged to points A and B, respectively, in the SHG crystal. c) Schematic of the crossed Czerny–Turner, astigmatism-free, imaging spectrometer. The spherical collimating mirror has an incidence angle in the tangential plane θ_{C}, and a radius R_{C}. L_{SC}: distance between the slit and the collimating mirror. The grating has a pitch Γ, an incidence angle α, and a diffraction angle β. L_{CG}: distance between the collimating mirror and the grating. The spherical focusing mirror has an incidence angle θ_{F}, and a radius R_{F}. L_{GF}: distance between the grating and the focusing mirror. CCD: charge-coupled device detector with an incidence angle θ_{D}. L_{FD}: distance between the focusing mirror and the detector.

to allow selection of the homogeneous centre of the beam for the measurement. The beam then passes through a prism so that each vertical slice of the spatial beam profile passes through a different thickness of glass.

The next step is the most critical step of the single-shot d-scan, namely the SHG. Because of angular dispersion after the prism, its exit surface must be imaged onto the SHG crystal, so that a second-harmonic spectrum is generated for each glass insertion. Furthermore, it must be imaged as a horizontal thin line so that the second-harmonic spectrum as a function of glass insertion can then be observed with an imaging spectrometer. In a previous implementation [75], a slit was used before the prism to select a horizontal line. The work described in Paper II focused on increasing the efficiency of the measurement (and therefore the signal-to-noise ratio) to make single-shot measurements more feasible. The most straightforward way of improving the signal-to-noise ratio is not to have a slit before the prism and to focus the beam in the vertical plane, while imaging on the horizontal plane. This could be done with a combination of spherical and cylindrical mirrors, but a simpler, more compact approach was chosen.

A spherical mirror was placed off-axis to make use of the fact that astigmatism leads to a different effective focal length in the sagittal and tangential planes, thus enabling focusing in one plane while imaging in the other (see Figure 3.8b). When a spherical mirror of radius R is used off-axis, the focal length is shortened in the tangential plane (incidence plane) and lengthened in the sagittal plane (perpendicular). The effective focal lengths in the tangential and sagittal planes, are given by:

$$f_{\mathrm{T}} = R\cos\varphi/2 \tag{3.11a}$$

$$f_{\mathrm{S}} = R/(2\cos\varphi) \tag{3.11b}$$

where φ is the angle of incidence on the spherical mirror. Since the aim is to image the exit face of the prism onto the SHG crystal in the tangential plane, this imaging equation must be verified:

$$\frac{1}{s_1} + \frac{1}{s_2} = \frac{1}{f_{\mathrm{T}}} \tag{3.12}$$

where s_1 is the distance between the prism and the mirror, and s_2 is the distance between the mirror and the SHG crystal ($s_2 = f_{\mathrm{S}}$). Thus,

$$s_1 = \frac{R\cos\varphi}{2\sin^2\varphi}. \tag{3.13}$$

A simple solution is found for $\varphi = 45°$ giving $s_1 = s_2 = 2f_{\mathrm{T}} = f_{\mathrm{S}}$, with $f_{\mathrm{T}} = R/(2\sqrt{2})$ and $f_{\mathrm{S}} = R/\sqrt{2}$. This solution leads to one-to-one imaging in the tangential plane and focusing in the sagittal plane. The magnification can be changed by choosing a different angle. In the experiment described in Paper II, an angle of $\varphi = 40°$ was used. This analysis is very simplified and only astigmatism was considered. Furthermore, due to the refraction of the prism, the object plane has an angle of about 40° in respect to the optical axis, thus not all points in the plane can exactly verify the imaging equation. Therefore, ray tracing simulations were performed to validate the approximations, and satisfactory results were obtained (see Paper II).

Once this imaging has been performed, the second-harmonic spectrum is measured as a function of horizontal position, i.e., glass insertion. However, imaging spectrometers are not readily available for this wavelength range (260 to 460 nm), and one had

to be designed for this purpose. A crossed Czerny–Turner design [77–79] was chosen because it is very compact, requires only off-the-shelf components, and can be made astigmatism-free. A schematic of the imaging spectrometer is shown in Figure 3.8c. The spectrometer is rotated of 90° in respect to the rest of the setup, i.e., it stands on a vertical breadboard. Therefore, the beam enters as a vertical line in respects to the spectrometer. The first component of an imaging spectrometer is usually a slit to select a thin line from the beam. Here, it was replaced by the SHG crystal since the beam is focused as a line onto the crystal. A spherical mirror is used to collimate the beam, followed by a grating to angularly disperse frequencies for each point of the slit. Another spherical mirror then focuses the beam into a detector. An imaging is performed from the slit (here SHG crystal) to the detector. Therefore, an image of the spectrum at each point of the slit is obtained.

In a standard crossed Czerny–Turner design, astigmatism occurs on both the collimating and focusing mirrors, leading to different effective focal lengths in different planes (as can be seen from Equations 3.11). This astigmatism can be corrected to the first order at one chosen wavelength by using divergent illumination of the grating. The grating acts like a mirror in the sagittal plane and follows the grating equation in the tangential plane:

$$\sin\beta = \sin\alpha + \Gamma\lambda \tag{3.14}$$

where α is the angle of incidence, β the diffraction angle, and Γ the pitch of the grating. Under divergent illumination, the diffracted beam in the tangential plane is more divergent than the incident beam and, since the diffraction angle exceeds the incident angle, the transverse reflected beam size is smaller than the incident beam size. The combination of these effects brings the apparent image closer to the grating than the object, leading to a closer apparent image in the tangential plane than in the sagittal plane. It is therefore possible to correct the astigmatism caused by the two spherical mirrors by tuning the divergence on the grating.

A brief presentation of the procedure to design the imaging spectrometer will now be given. All the equations necessary to calculate the different parameters will be given, but not demonstrated. A complete derivation of these equations can be found in Reference [78]. The design of the imaging spectrometer is as follows. First, the mirror radii, R_C and R_F, and angles, θ_C and θ_F, as well as the grating pitch, Γ and angle, α, are chosen. The zeroth order condition is then used to determine the distance between the slit (or SHG crystal) and the collimation mirror (L_SC), and the distance between the focusing mirror and the detector (L_FD). In order to image the SHG crystal onto the detector, the distances between the focusing mirror and the image in the sagittal plane, S_S, and in the tangential plane, S_T, were calculated by sequentially applying imaging conditions.

$$S_\mathrm{S} = \frac{R_\mathrm{C} R_\mathrm{F} L_\mathrm{SC}}{2L_\mathrm{SC}(R_\mathrm{C}\cos\theta_\mathrm{F} + R_\mathrm{F}\cos\theta_\mathrm{C}) - R_\mathrm{C} R_\mathrm{F}} \tag{3.15}$$

$$S_\mathrm{T} = \frac{R_\mathrm{C} R_\mathrm{F} L_\mathrm{SC}}{2L_\mathrm{SC}\left(R_\mathrm{C}\sec\theta_\mathrm{F} + R_\mathrm{F}\frac{\cos^2\alpha}{\cos^2\beta}\sec\theta_\mathrm{C}\right) - R_\mathrm{C} R_\mathrm{F}\frac{\cos^2\alpha}{\cos^2\beta}} \tag{3.16}$$

A stigmatic image is achieved when $S_\mathrm{S} = S_\mathrm{T}$. This corresponds to:

$$L_\mathrm{SC} = \frac{\frac{1}{2}R_\mathrm{C}R_\mathrm{F}\left(\frac{\cos^2\alpha}{\cos^2\beta} - 1\right)}{R_\mathrm{C}(\sec\theta_\mathrm{F} - \cos\theta_\mathrm{F}) + R_\mathrm{F}\left(\frac{\cos^2\alpha}{\cos^2\beta}\sec\theta_\mathrm{C} - \cos\theta_\mathrm{C}\right)} \tag{3.17}$$

This gives the position of the detector: $L_\mathrm{FD} = S_\mathrm{S} = S_\mathrm{T}$.

Finally, the first-order condition was used to calculate the remaining parameters, i.e., the distance between the grating and the focusing mirror, L_GF, and the angle of the detector, θ_D. The distance between the collimating mirror and the grating, L_CG, is irrelevant at this level of approximation and can be chosen arbitrarily, with some considerations for compactness.

All wavelength dependence arises from the wavelength dependence of β, and changes S_T directly, and also affects the incidence angle on the focusing mirror, θ_F, altering S_T and S_S. A stigmatic image will be maintained if the tangential and sagittal images move at the same rate, i.e., $dS_\mathrm{S}/d\beta = dS_\mathrm{T}/d\beta$. Using algebraic differentiation together with wavelength-dependent ray tracing analysis (see [78] for details), allows the calculation of L_GF and θ_D.

$$L_\mathrm{GF} = R_\mathrm{F}\cos\theta_\mathrm{F}\left(1 - \frac{d\theta_\mathrm{F}}{d\beta}\right) \tag{3.18}$$

with

$$\frac{d\theta_\mathrm{F}}{d\beta} = \frac{\frac{\partial S_\mathrm{T}}{\partial\beta}}{\left(\frac{\partial S_\mathrm{S}}{\partial\theta_\mathrm{F}} - \frac{\partial S_\mathrm{T}}{\partial\theta_\mathrm{F}}\right)} \tag{3.19}$$

where

$$\frac{\partial S_\mathrm{S}}{\partial\theta_\mathrm{F}} = \frac{2S_\mathrm{S}L_\mathrm{SC}R_\mathrm{C}\sin\theta_\mathrm{F}}{2L_\mathrm{SC}(R_\mathrm{C}\cos\theta_\mathrm{F} + R_\mathrm{F}\cos\theta_\mathrm{C}) - R_\mathrm{C}R_\mathrm{F}} \tag{3.20}$$

$$\frac{\partial S_\mathrm{T}}{\partial\beta} = \frac{-2S_\mathrm{T}R_\mathrm{F}(2L_\mathrm{SC}\sec\theta_\mathrm{C} - R_\mathrm{C})\cos^2\alpha\tan\beta\sec^2\beta}{2L_\mathrm{SC}\left(R_\mathrm{C}\sec\theta_\mathrm{F} + R_\mathrm{F}\frac{\cos^2\alpha}{\cos^2\beta}\sec\theta_\mathrm{C}\right) - R_\mathrm{C}R_\mathrm{F}\frac{\cos^2\alpha}{\cos^2\beta}} \tag{3.21}$$

$$\frac{\partial S_\mathrm{T}}{\partial\theta_\mathrm{F}} = \frac{-2S_\mathrm{T}L_\mathrm{SC}R_\mathrm{C}\sec\theta_\mathrm{F}\tan\theta_\mathrm{F}}{2L_\mathrm{SC}\left(R_\mathrm{C}\sec\theta_\mathrm{F} + R_\mathrm{F}\frac{\cos^2\alpha}{\cos^2\beta}\sec\theta_\mathrm{C}\right) - R_\mathrm{C}R_\mathrm{F}\frac{\cos^2\alpha}{\cos^2\beta}} \tag{3.22}$$

Moreover,

$$\tan\theta_\mathrm{D} = \frac{\frac{dS_\mathrm{S}}{d\beta} + L_\mathrm{GF}\tan\theta_\mathrm{F}}{L_\mathrm{FD} + L_\mathrm{GF} - \frac{2L_\mathrm{GF}L_\mathrm{FD}}{R_\mathrm{F}\cos\theta_\mathrm{F}}} \tag{3.23}$$

with

$$\frac{dS_\mathrm{S}}{d\beta} = \frac{\partial S_\mathrm{S}}{\partial\theta_\mathrm{F}}\frac{d\theta_\mathrm{F}}{d\beta} \tag{3.24}$$

Table 3.2 gives the chosen and calculated parameters for the imaging spectrometer described in Paper II. The parameters were chosen so that the resulting magnification would give a spectral range from 273 nm to 459 nm on our 2/3 inch CCD sensor. This spectral range is slightly smaller than that required to record the full second-harmonic spectrum. However, due to the robustness of the first algorithm, accurate retrieval was possible if the fundamental spectrum was measured separately. The single-shot d-scan

system was successfully tested by comparing it to the standard d-scan technique (see Paper II). The resulting traces were very similar and yielded similar spectral phases and temporal profiles, showing that this single-shot system not only measures the main peak of the temporal profile of the pulse accurately, but also its wings and satellites.

Table 3.2: Imaging spectrometer parameters

Chosen parameter	Value	Calculated parameters	Value
Central wavelength (nm)	350	β (°)	48.4
R_{C} (mm)	200	L_{SC} (mm)	93.3
R_{F} (mm)	200	L_{GF} (mm)	33.2
θ_{C} (°)	5	L_{FD} (mm)	109.1
θ_{F} (°)	7	θ_{D} (°)	8.68
α (°)	40		
Γ (mm^{-1})	300		
L_{CG} (mm)	56		

3.4 Carrier–envelope phase

In the time domain, the electric field associated with an optical pulse can be described as the product of a fast sinusoidal oscillation, called the carrier, and a more slowly varying function, called the envelope. The carrier propagates at a velocity called the phase velocity, and the envelope, at the group velocity. When optical pulses propagate through a medium, dispersion and possible nonlinearities lead to a difference between the phase velocity and the group velocity. The resulting offset phase, ϕ_{CE}, between the carrier and the envelope is called the CEP. The CEP difference between consecutive pulses, $\Delta\phi_{\mathrm{CE}}$, is called the carrier–envelope phase offset (CEO). The CEP and CEO are illustrated in Figure 3.9.

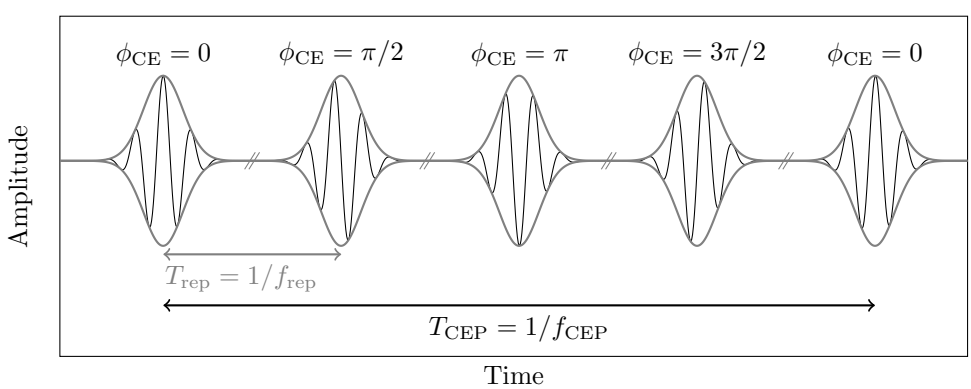

Figure 3.9: Typical pulse train of a mode-locked oscillator. The carrier is shown in black and the envelope in grey. The CEP, ϕ_{CE}, depends on the delay between the carrier and the envelope. The CEP is linearly varying, i.e., constant CEO of $\Delta\phi_{\mathrm{CE}} = \pi/2$.

Typically, in a CPA laser system the oscillator produces pulses with a high-repetition rate (~ 80 MHz). The repetition rate is then lowered before amplification by selecting pulses with, e.g., a picker Pockels cell. In a CEP-stable system, the CEO is stabilized in the oscillator so that all the selected pulses have the same CEP, this is called the fast loop. In the pulse train shown in Figure 4.16, for example, the CEO is stabilized to $\pi/2$ and thus every fourth pulse has the same CEP. Therefore, if the repetition rate is lowered by a factor of four (or a multiple of four) every selected pulse would have the same CEP. After amplification, the CEP is further stabilized in order to minimize CEP fluctuations, this is called the slow loop [80].

Methods have been developed to measure the CEO in a pulse train or the CEP fluctuations [81–84]. Typically, the pulse is first spectrally broadened by SPM to reach an octave spanning spectrum, for example, by nonlinear propagation through glass. Then, using SHG or difference frequency generation (DFG), a second pulse, with higher frequency (doubled) or, lower frequency, respectively, is created. In this section, we will study the case of SHG. In the region where the spectrum of the new pulse overlaps with the fundamental spectrum, spectral interference, yielding information on the CEP, will occur. The CEP can be actively modified by, e.g, adjusting the pump power of the oscillator to change nonlinear dynamics or using an acousto-optic modulator to change the spectral phase of the pulse.

3.4.1 The fast loop

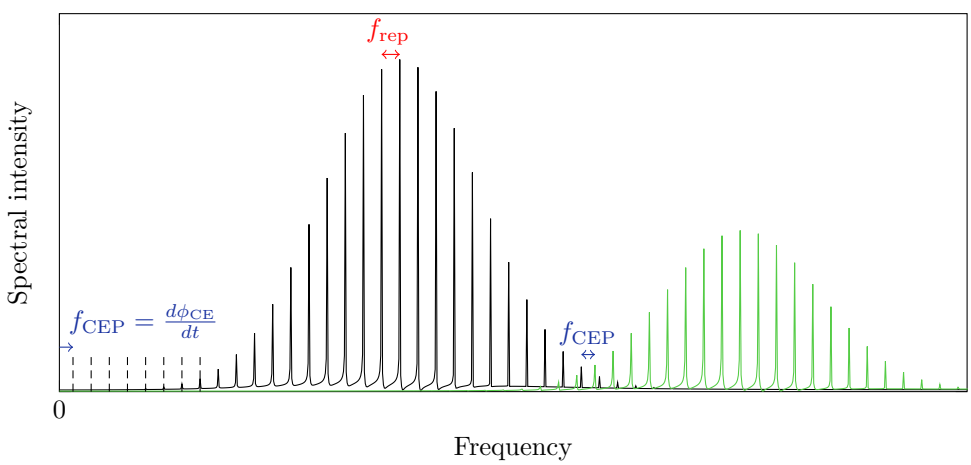

Figure 3.10: The frequency comb associated with the pulse train (black) and its frequency doubled spectrum (green). The line spacing of the combs is determined by the repetition rate and the offset frequency is exactly the carrier–envelope frequency $f_{\mathrm{CEP}} = d\phi_{\mathrm{CE}}/dt$ which is also the beating frequency at the overlap of the two combs.

In the frequency domain, a pulse train of short pulses is associated with a frequency comb, i.e., an optical spectrum that consists of equidistant lines separated by the repetition rate. The offset frequency is exactly the carrier–envelope frequency, $f_{\mathrm{CEP}} = d\phi_{\mathrm{CE}}/dt$ (see Figure 3.10). Therefore, the frequency of a peak in the spectrum can be expressed as: $f_n = f_{\mathrm{CEP}} + nf_{\mathrm{rep}}$, where n is an integer and f_{rep} is the repetition

rate. The pulse train created by SHG is also associated with a frequency comb, only the frequency is doubled. The frequency of a peak in the spectrum can thus be expressed as: $2f_m = 2f_{\mathrm{CEP}} + 2mf_{\mathrm{rep}}$, where m is an integer. In the region where the high-frequency wing of the original comb overlaps with the low-frequency wing of the frequency-doubled comb, interference beating with $n = 2m$ will occur, and the beating frequency will be $f_n - 2f_m = f_{\mathrm{CEP}}$.

The CEO can be obtained by measuring the beating frequency of the two combs. This can be done by recording the intensity as a function of time in the region of spectral overlap of the fundamental and second-harmonic spectra. In the laser system used in this work, the CEO is measured in-line after the oscillator, using a 0-to-f interferometer based on DFG [85] together with a photodiode. The frequency of the recorded oscillation is f_{CEP} and thus, gives the CEO. Feedback is sent to an acousto-optic modulator that controls the pump power of the oscillator in order to stabilize the CEO to $\pi/2$.

3.4.2 The slow loop

To stabilize the CEP after the amplifier so that each pulse of the train has the same CEP, a different approach is necessary since the repetition rate is lower. A temporal delay, Δt, between the fundamental pulse and its frequency-doubled replica can be added. The spectral intensity in the overlapping region will then exhibit spectral interference fringes which position is CEP-dependent (see Figure 3.11).

The electric field of the fundamental pulse can be written, in the time domain, as the product of an amplitude and a complex phase:

$$E_{\mathrm{F}}(t) = |E_{\mathrm{F}}(t)|\exp\left(i\omega_0 t - i\varphi(t)\right) \tag{3.25}$$

where ω_0 is the carrier frequency and $\varphi(t)$ a time-dependent phase. Let us assume that only the zeroth order of the phase, i.e., the CEP, varies between consecutive pulses. The field of a certain pulse of the train can then be written as:

$$E_1(t) = E_{\mathrm{F}}(t)\exp\left(i\phi_{\mathrm{CE}}\right) \tag{3.26}$$

This is valid when the energy of the laser is stable (energy fluctuations lead to phase variation through the SPM process when the pulse is spectrally broadened). SHG can be modelled by taking the square of the field.

$$E_2(t) = E_{\mathrm{F}}^2(t)\exp\left(2i\phi_{\mathrm{CE}}\right) \tag{3.27}$$

Going to the frequency domain, the fields of the fundamental and the temporally delayed second harmonic can be written as:

$$\hat{E}_1(\omega) = \hat{E}_{\mathrm{F}}(\omega)\exp\left(i\phi_{\mathrm{CE}}\right) \tag{3.28a}$$

$$\hat{E}_2(\omega) = \hat{E}_{\mathrm{SHG}}(\omega)\exp\left(2i\phi_{\mathrm{CE}} - i\omega_0\Delta t\right) \tag{3.28b}$$

where $\hat{E}_{\mathrm{SHG}} = \mathcal{F}[E_{\mathrm{F}}^2(t)]$. The spectral intensity in the overlapping region, resulting from spectral interference, can be expressed.

$$\hat{I}_{\mathrm{tot}} = \hat{E}_1^2 + \hat{E}_2^2 + 2\hat{E}_1\hat{E}_2\cos(\phi_{\mathrm{CE}} + \omega_0\Delta t) \tag{3.29}$$

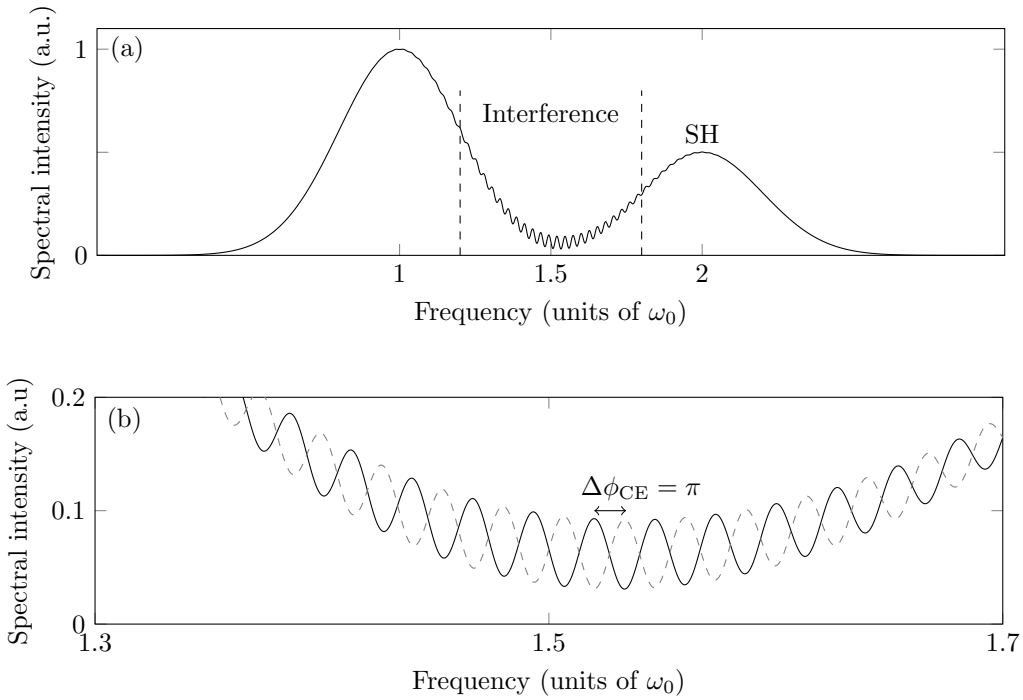

Figure 3.11: a) A pulse with an octave spanning spectrum and its second harmonic (SH) interfere in the spectral region where their spectra overlap. If the pulses are temporally delayed, the spectral intensity in the region of spectral overlap will exhibit fringes oscillating as $\cos(\phi_{\mathrm{CE}} + \omega_0 \Delta t)$. b) Magnified view of the fringes for $\phi_{\mathrm{CE}} = 0$ (solid line) and $\phi_{\mathrm{CE}} = \pi$ (dashed line). The position of the fringes yields a relative CEP.

Changes of the CEP can be measured by recording the position of the interference fringes. If the complete phase of the octave-spanning pulses is known and the nonlinear generation process can be exactly modelled, the absolute CEP can be extracted from the measurement [86]. In the laser system used in this work, an f-to-2f interferometer is used. The laser beam is tightly focused in a nonlinear crystal for SHG, and then imaged onto a fibre spectrometer to record the fringes arising from the spectral interference. The temporal delay between the fundamental and the second harmonic is inherently induced by the dispersion in the SHG crystal. For the feedback loop, two options were considered: either measuring the CEP just after the compressor of the main laser chain, or after the capillary. In both cases, feedback was sent to the DAZZLER placed after the stretcher, which can control the spectral phase of the pulses. Figure 3.12 shows the resulting stability after the capillary for both options. It is clear that the capillary adds instability to the CEP, and thus, the feedback signal should be sent from after the capillary to achieve the best stability.

The stability of the CEP is very sensitive to noise. To improve the CEP-stability, the sources of noise were identified and reduced to a minimum. Vibration measurements were performed at several places in our laboratory, and the frequencies of the different vibrations were analysed to identify their causes. Beam pointing drift can cause

changes in dispersion in the stretcher and the compressor, leading to low-frequency (< 10 Hz) fluctuations. Mechanical vibrations arising, for example, from the vacuum pumps, or human voice vibrations, can range from 10 Hz to 1 kHz. The energy fluctuations of the pump laser can have a high frequency (~ 1 kHz). Several measures have been taken to reduce vibrations to a minimum: the cold head of the laser's cryogenic amplifier is not fixed to the optical table, the pre-vacuum pumps are stored in an adjacent room with a vibration-isolated floor, the turbo pumps fixed to the HHG chambers are magnetically supported, and the tube connecting the capillary to the vacuum pump is passed through a bucket filled with concrete to attenuate vibrations, while the pump is placed on a support that absorbs vibrations.

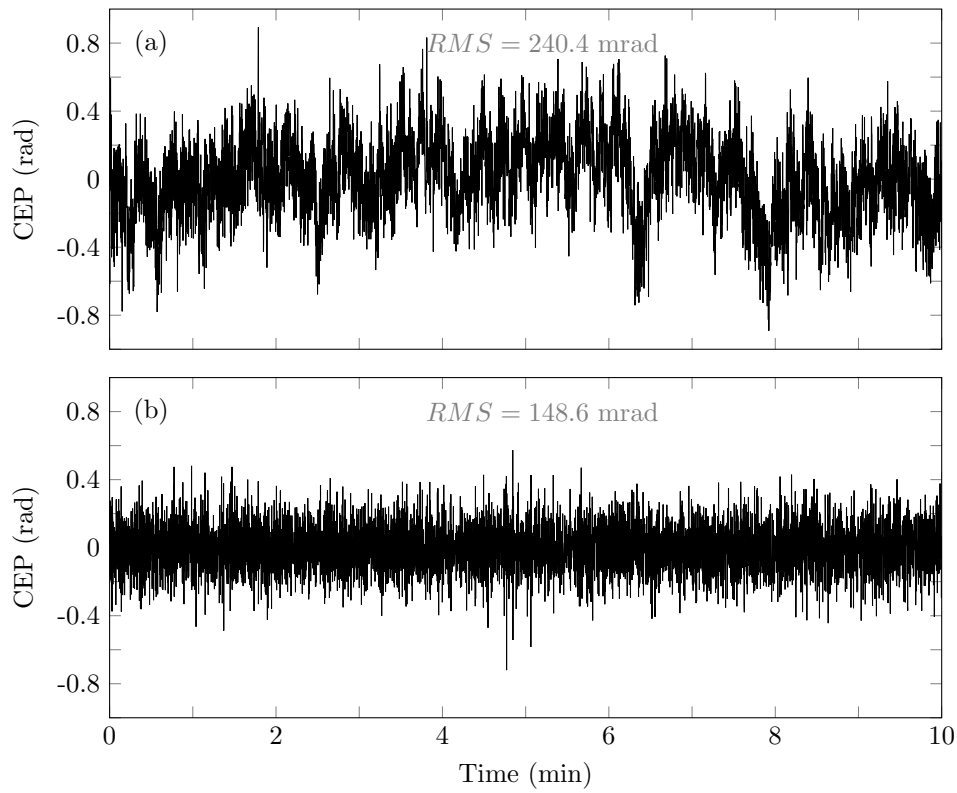

Figure 3.12: CEP measured after the capillary (second setup) with an f-to-2f interferometer. a) Out-of-loop measurement of the CEP fluctuations when the feedback to the DAZZLER is sent from a measurement performed after the compressor of the main laser chain. b) In-loop measurement of the CEP fluctuations when the feedback to the DAZZLER is sent from a measurement performed after the capillary.

Chapter 4

High harmonic generation

4.1 Introduction

Femtosecond pulses can be used to generate coherent XUV radiation via HHG. When a short intense laser field is focused into a gas, it induces a highly nonlinear electronic response and high-order harmonics of the driving field can be generated. When such harmonics were first observed, at the end of the 1980s [18, 19], their spectral behaviour came as a surprise. For the first few harmonics, the intensity decreased rapidly, as expected from a perturbative approach. However, this was followed by an unexpected, far-reaching, plateau where the harmonics exhibited almost constant intensity, ending in an abrupt cut-off (see Figure 4.1). These observations called for the development of new theoretical models.

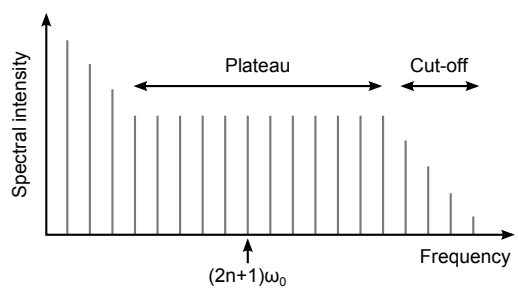

Figure 4.1: Schematic of a typical spectrum produced by HHG in a gas. In the plateau region, the harmonic intensity remains essentially constant. In the cut-off region, the intensity falls abruptly. Typically, only odd-order harmonics of the driving frequency, ω_0, are generated.

The XUV radiation from HHG is usually emitted as a train of phase-locked pulses along the propagation axis, where each pulse has a bandwidth that can support about a hundred attoseconds pulse duration. Since such pulses are on the attosecond timescale, they can be used to study electron dynamics. The temporal characterization of these pulses was not straightforward, and an interferometric method called RABBIT was developed, which could be used to retrieve the spectral phase of the attosecond pulses

[87–89]. Later, it was discovered that this method could also be used to measure the phase of electron dynamics in atoms [90–94], molecules [95, 96], and solids [97].

Although attosecond pulse trains have many applications, they are inherently restricted by their periodicity. Therefore, the need for broadband IAPs has grown. Commonly-used techniques require spectral filtering of the harmonic radiation and extensive manipulation of the fundamental field. A new technique called NOG [98] was developed in Lund. These limitations can be overcome with this technique, and it allows the generation of several spatially separated, synchronized IAPs, making it suitable for XUV-pump–XUV-probe experiments. Moreover, this technique is a promising candidate for intra-cavity HHG [99, 100].

The principles of HHG are described in this chapter, after which the scalability of HHG, presented in Paper IV, is discussed. RABBIT is then introduced, and emphasis placed on its use to measure the spectral phase of a Fano resonance, as described in Paper V. Finally, the generation of IAPs is presented with emphasis on NOG, which was experimentally demonstrated in the study described in Paper III.

4.2 Principles of HHG

The theoretical description of the characteristic plateau in the high-harmonic spectrum requires a theory that extends beyond lowest-order perturbation theory [101].

4.2.1 The time-dependent Schrödinger equation

The first calculations to successfully reproduce the plateau and cut-off of high-harmonic spectra were based on simulating the behaviour of an atom in a strong laser field, by solving the time-dependent Schrödinger equation (TDSE) within the single-active-electron approximation [102, 103]:

$$-\frac{\hbar^2}{2m_e}\nabla^2\Psi + [V(r) + e\mathbf{E}.\mathbf{r}]\Psi = i\hbar\frac{\partial\Psi}{\partial t} \tag{4.1}$$

where $V(r)$ is the atomic potential and e, m_e are the charge and mass of the electron. The interaction between the laser and the atom is described within the dipole approximation. The linearly polarized electromagnetic field, $\mathbf{E}$, can be written as $E_0 \sin(\omega_0 t)\mathbf{x}$, where $\mathbf{x}$ is the polarization direction and E_0 is the slowly varying envelope (this variation is neglected in the following calculations). The dipole moment can be calculated from the time-dependent wave function $\Psi(t)$:

$$d(t) = < \Psi(t) \mid ex \mid \Psi(t) > \tag{4.2}$$

The harmonic spectrum emitted by a single atom can then be calculated, and is equal to the square of the Fourier transform of the acceleration, which corresponds to the second derivative of the dipole moment. The dipole moment can be developed as a Fourier series:

$$d(t) = \sum_q d_q e^{iq\omega_0 t} \tag{4.3}$$

yielding the single-atom, nonlinear dipole moment, d_q, of each harmonic, q, with an angular frequency $q\omega_0$.

4.2.2 The three-step model

Following the success of TDSE-based calculations, a very intuitive semi-classical model, called the three-step or simple man's model, was derived [104–106]. Figure 4.2 shows a schematic of this model.

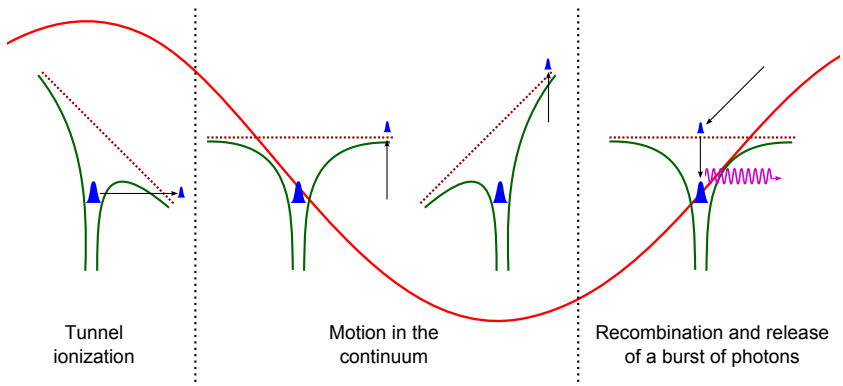

Figure 4.2: Schematic of the three-step model. The intense driving field (red) distorts the atomic potential (green). At each crest of the field, an electron (blue) can be ionized by tunnelling through the distorted barrier. The electron is then driven away by the field before being brought back, when the field changes sign. Finally, if the electron recombines with its parent ion, the kinetic energy acquired during its motion in the continuum can be released in the form of a burst of high-energy photons with sub-cycle duration (purple).

The first step of the model has a purely quantum mechanical origin. When a femtosecond laser pulse is focused onto a gas target and its peak intensity reaches about 10^{14} W/cm^2, the laser field becomes strong enough to distort the atomic potential seen by the valence electron. The potential barrier is so strongly distorted in a narrow region around the crest of the field, that there is a high probability that the valence electron will tunnel into the continuum. The rate of this tunnel ionization depends exponentially on the field amplitude.

Once the electron has tunnelled, it is free to move in the continuum. This motion is driven by the linearly polarized driving field. The electron is first accelerated away from its parent ion. When the field changes sign, the electron is decelerated and its direction of motion eventually changes. Finally, it may be driven back to its original position, i.e., the ionic core. This second step of the model, i.e., the motion of the electron in the continuum, can be described classically (at least to a first approximation) using Newton's second law. If we assume that the electron was freed at a time: $t = t_i$ and position: $x(t_i) = 0$ with zero velocity: $\dot{x}(t_i) = 0$, then we can easily solve Newton's equation:

$$\ddot{x}(t) = -\frac{eE_0}{m_e}\sin(\omega_0 t) \tag{4.4}$$

which gives:

$$\dot{x}(t) = \frac{eE_0}{m_e\omega_0}[\cos(\omega_0 t) - \cos(\omega_0 t_i)] \tag{4.5}$$

and

$$x(t) = \frac{eE_0}{m_e\omega_0^2}[\sin(\omega_0 t) - \sin(\omega_0 t_i) - \omega_0(t - t_i)\cos(\omega_0 t_i)] \tag{4.6}$$

Equation 4.6 gives the electron trajectories in the continuum. These trajectories are shown in Figure 4.3. Some electrons will never return to the ionic core, and will only contribute to ionization. Others, however, will return to the ionic core with the high kinetic energy they acquired during their motion in the continuum. These electrons can recombine with their parent ion and release their kinetic energy in the form of a burst of high-energy photons with sub-cycle duration. This is the last step in the model.

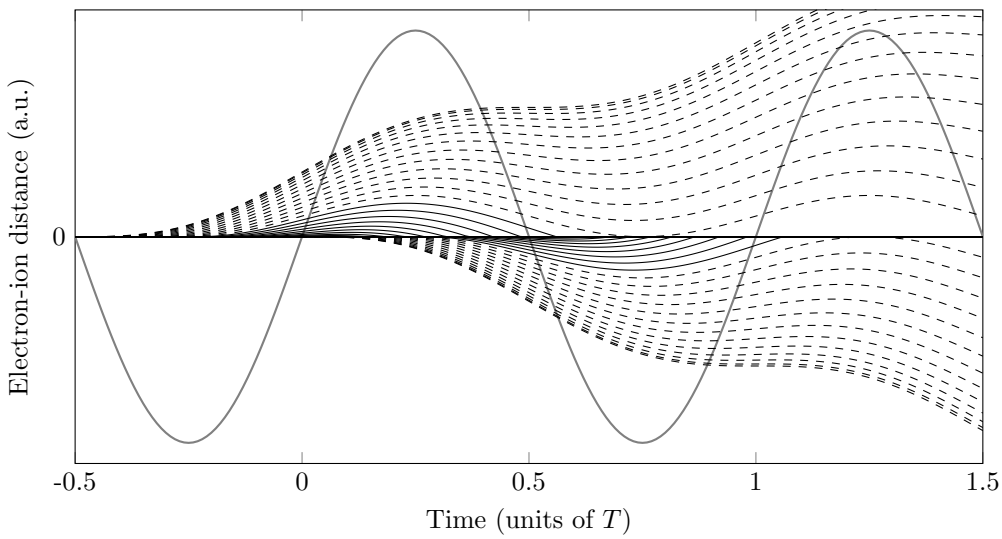

Figure 4.3: Electron trajectories. The solid grey sinusoidal line represents the intense driving field. Electrons trajectories for electrons freed between $-0.5T$ and $0.5T$ are shown. The trajectories in solid black are those of the electrons returning to the ionic core, and thus contributing to HHG. The trajectories shown as dashed black lines are those of the electrons that never return to the ionic core, and thus contribute only to ionization.

The kinetic energy acquired by an electron during its motion in the continuum depends on its trajectory and, therefore, on its ionization time, t_i, and return time, t_r, and can be calculated from Equation 4.5.

$$E_{\text{kin}} = \frac{1}{2} m_e \dot{x}^2(t_r) = \frac{e^2 E_0^2}{2 m_e \omega_0^2} [\cos(\omega_0 t_r) - \cos(\omega_0 t_i)]^2 = 2U_{\text{p}} [\cos(\omega_0 t_r) - \cos(\omega_0 t_i)]^2 \tag{4.7}$$

where U_{p} is the ponderomotive energy, i.e., the mean kinetic energy of an electron oscillating in the driving field:

$$U_{\text{p}} = \frac{e^2 E_0^2}{4 m_e \omega_0^2} \tag{4.8}$$

and the return times, t_r, are solutions of $x(t_r) = 0$. Following Equation 4.6, the return times are solutions of:

$$\sin(\omega_0 t_r) - \sin(\omega_0 t_i) - \omega_0 (t_r - t_i) \cos(\omega_0 t_i) = 0 \tag{4.9}$$

Figure 4.4 shows the kinetic energy as a function of ionization time and return time. The maximum kinetic energy is equal to 3.17 U_{p}. All energies (except the maximum)

can be reached by two different trajectories, called the long and the short trajectories. It is possible to select short or long trajectories experimentally by changing the position of the gas target with respect to the focus of the driving beam, and by using suitable spatial filters in the XUV beam path.

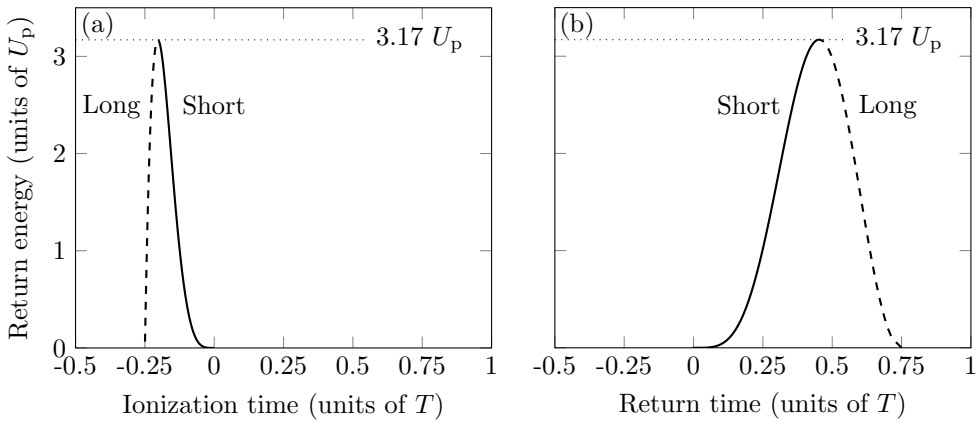

Figure 4.4: Kinetic energy of the recombining electrons, normalized to the ponderomotive energy (U_p), as a function of the ionization time (a) and of the return time (b). The short trajectories are shown in solid lines and the long trajectories, in dashed lines.

The XUV emission upon recombination of the free electron can be described as the radiation emitted by an oscillating dipole. An electric dipole is formed by the coherent overlap of the portion of the electron wave function that has tunnelled out, and the portion that remained bound to the parent ion. During a small fraction of an optical cycle of the driving field, this dipole acts as an atomic antenna [107], thus leading to high harmonic radiation.

The energy of the emitted burst of photons upon recombination is directly related to the kinetic energy of the recombining electron:

$$E = E_{\text{kin}} + I_p \tag{4.10}$$

where I_p is the ionization potential of the atom. All possible photon energies up to the maximum energy have approximately equal probability, leading to the long plateau in the harmonic spectrum (see Figure 4.1). The maximum energy that can be emitted by HHG is:

$$E_{\text{max}} = 3.17\ U_p + I_p \tag{4.11}$$

This is called the cut-off law. Depending on the intensity and wavelength of the driving field, the emitted radiation may extend in the XUV from a few electronvolts to a few hundred electronvolts.

It can be seen from Figure 4.4b that different return energies correspond to different return times. This means that radiation with different frequencies will be emitted at different times, i.e., the XUV radiation is chirped ($GDD \neq 0$). Furthermore, short and long trajectories will have an opposite chirp. Emission from the short trajectories shows a positive, almost linear chirp, while that from the long trajectories exhibits a negative chirp.

From Figures 4.2 and 4.3 it can be seen that the process can occur every half-cycle of the driving field, leading to the emission of an XUV pulse every half-cycle, thus forming a pulse train of attosecond pulses. Since the generation medium is isotropic, the sign flip of the driving field leads to consecutive pulses having an opposite sign, i.e., a phase opposition. Their interference results in a frequency comb of phase-locked high-order harmonics. Since the temporal periodicity is half a cycle ($T/2$), this results in a periodicity of $2\omega_0$ in the frequency domain (or $2\hbar\omega_0$ in energy), and only odd harmonics are observed because of the phase opposition. The longer the pulse train, i.e., the more consecutive harmonics interfere with each other, the smaller the spectral width of the harmonics.

Although simple, the three-step model predicts the cut-off energy and the main characteristics of the trajectories of the electrons between ionization and recombination. A quantum mechanical model, based on an approximate solution of the TDSE, called the strong-field approximation or Lewenstein model [108, 109], was derived soon after the three-step model to provide a more complete description of the HHG process.

4.2.3 Phase matching

In the models described above, only the single-atom response was taken into account. However, in HHG, many atoms contribute to the XUV emission. To achieve the maximum XUV signal, constructive interference is necessary between the XUV radiation emitted from different atoms, i.e., the XUV field emitted by each atom must oscillate in phase with the others (see Figure 4.5). The condition for this coherent addition is called phase matching [110], and can be described by the wave vector mismatch, $\Delta k = k_q - qk$, i.e., the difference between the propagating q^{th} harmonic field and the polarization field induced by the driving field at the harmonic frequency. Perfect phase matching is achieved for $\Delta k = 0$.

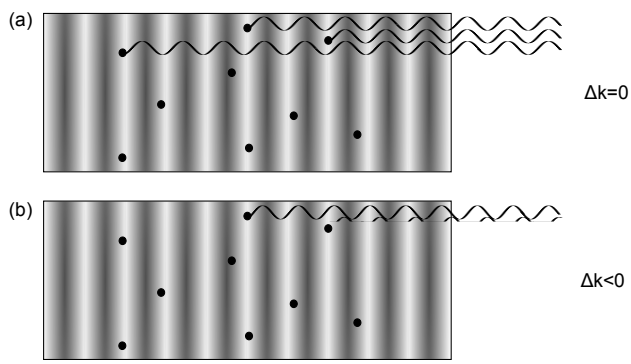

Figure 4.5: Illustration of the phase matching of harmonic generation using the second harmonic as an example. The shading represents the real part of the driving field, the dots some atoms, and the oscillations the second harmonic generated by each atom. a) Phase-matched generation: the harmonic fields from the different atoms are in phase and add constructively. b) Non-phase-matched generation: the harmonic fields from the different atoms are out of phase and do not add constructively.

There are four main contributions to wave vector mismatch (all terms are approximated for HHG close to the focus [111]).

[1] **Gouy phase.** When a free focus geometry is used for HHG, it leads to a phase offset between the phase front of the beam and a plane wave, that increases linearly with wavelength. The small Gouy phase of the harmonic beam can be neglected, and the total Gouy phase mismatch between the driving field and the q^{th} harmonic beam can thus be expressed as:

$$\Delta k_{\mathrm{G}} = q\frac{\lambda}{w_0^2\pi} \tag{4.12}$$

where w_0 is the driving beam waist radius at $1/e^2$.

[2] **Dipole phase.** The phase of the dipole induced by the interaction between the driving field and the atom depends on the intensity within the medium and thus varies with spatial position:

$$\Delta k_{\mathrm{D}}(x,z) = -\alpha\frac{\partial I(x,z)}{\partial z} \tag{4.13}$$

where I is the driving laser intensity and α is a constant that depends on whether the trajectory is short or long.

[3] **Neutral dispersion.** A phase mismatch arises from dispersion in the neutral gas since the driving field and the harmonic field experience different refractive indices.

$$\Delta k_{\mathrm{n}} = q\frac{\omega_0}{c}(n_1 - n_q) \tag{4.14}$$

where n_1 is the refractive index experienced by the driving field and n_q that experienced by the q^{th} harmonic.

[4] **Plasma dispersion.** Similarly to the neutral gas, a phase mismatch arises from dispersion due to the free electrons in the plasma:

$$\Delta k_{\mathrm{p}} = q\frac{\omega_0}{c}(n_1^e - n_q^e) \tag{4.15}$$

where n_1^e is the refractive index of the plasma for the driving field and n_q^e the refractive index of the plasma for the q^{th} harmonic.

The total wave vector mismatch can thus be expressed as:

$$\Delta k = \Delta k_{\mathrm{G}} + \Delta k_{\mathrm{D}} + \Delta k_{\mathrm{n}} + \Delta k_{\mathrm{p}} \tag{4.16}$$

It is possible to adjust Δk such that it is ~ 0 within a significant volume of the gas and a certain time interval (phase matching is a transient process), by changing the gas pressure, the driving beam intensity, and the position of the focus.

4.3 Scaling of HHG

HHG is a nonlinear optical phenomenon in gases and can be scaled using the formalism presented in Paper IV and Section 2.5. The scaling of HHG has been investigated previously in a phenomenological manner [112–114] but, to the best of the author's knowledge, no rigorous model had been presented. Paper IV presents a formalism for the scaling of the generation of attosecond pulse trains as well as IAPs. The scalability was verified using a simulation code based on the strong-field approximation, and including the propagation effects of the driving field, as well as the XUV field. Almost perfect scaling behaviour was observed.

During HHG, when the intense driving field propagates through the extended nonlinear medium, it induces a polarization, $\hat{P}_q = 2d_q\rho$, for each harmonic frequency, where d_q is the dipole moment (Equation 4.3) and ρ the gas density. The induced polarization leads to the generation of the harmonic field $\hat{E}_q$. If we choose the moving frame of the driving field as the reference frame, the harmonic field becomes $\hat{\mathcal{E}}_q \equiv \hat{E}_q \exp(-iq\omega_0 z/c)$, where z is the longitudinal position in the moving frame of reference. The propagation of $\hat{\mathcal{E}}_q$, including the phase-matching effects, can be described by Equation 2.49 using $\hat{P}_q$ as the nonlinear polarization. This equation is scalable and thus, so are the phenomena it describe. Therefore, considering a scaling parameter η, the harmonic energy follows the same scaling as the input energy, $\epsilon_q \to \eta^2\epsilon_q$, leading to a scale-invariant conversion efficiency, ϵ_q/ϵ_{in}. This means that HHG driven by intense laser pulses with loose focusing will yield the same conversion efficiency as much weaker laser pulses with tight focusing, if the parameters are chosen appropriately.

4.4 Reconstruction of attosecond beating by interference of two-photon transitions

RABBIT was the first technique allowing the measurement of the spectral phase of attosecond pulses (averaged over the pulse train) and, therefore, was the first technique allowing temporal characterization of attosecond pulses [87–89]. However, this technique has several other possibilities. The spectral phase is acquired through photoionization of a target medium and, thus, carries information not only about the phase of the pulse, but also about the temporal dynamics of photoionization in this medium. Therefore, this technique can be used for fascinating applications, such as the determination of relative photoelectron time delays [90–97], or measurements of the complete temporal dynamics of autoionizing resonances (Paper V,[115, 116]). Such measurements pave the way for the control of electron dynamics.

4.4.1 The principle of RABBIT

An XUV attosecond pulse train is focused into a target medium, together with a time-delayed, weak replica of the NIR field that drove the HHG. Electrons from the medium are photoionized by two-photon processes consisting of the absorption of an XUV photon from the harmonics, and the absorption or emission of a NIR photon. Electrons are thus released into the continuum with a kinetic energy $E_{\text{kin}} = (2q+1)\hbar\omega_0 \pm \hbar\omega_0 - I_p$, where I_p is the ionization potential. The NIR field is kept weak to avoid high-order

multiphoton processes. The kinetic energy of the free electrons is then measured with an electron spectrometer. The time delay between the XUV and the NIR pulses is scanned, and a photoelectron spectrum is recorded for each delay.

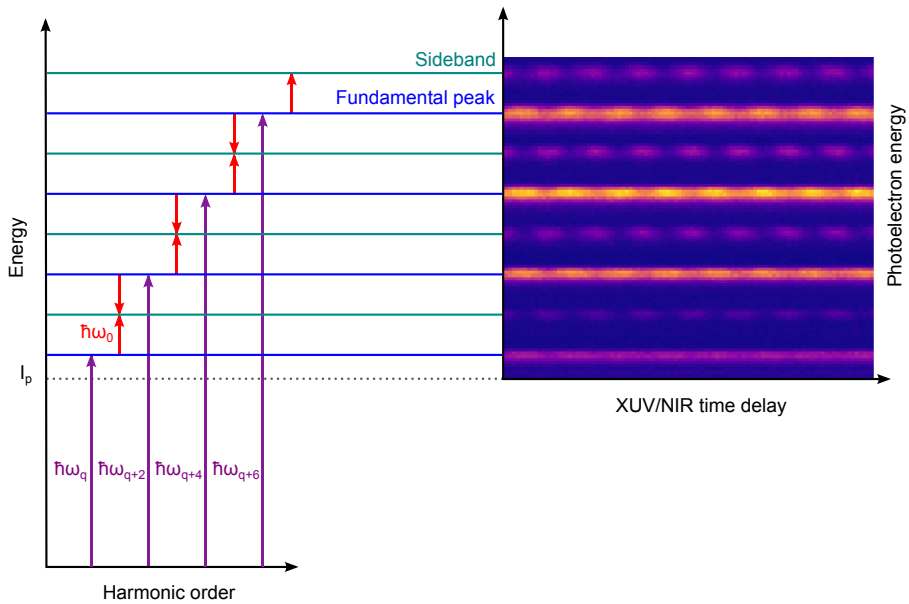

Figure 4.6: Schematic of the process behind a RABBIT measurement. Left: harmonics (purple arrows) photoionize electrons, creating fundamental peaks in the spectrum. Two-photon ionization consisting of the absorption of an XUV photon (purple arrows) and the absorption or emission of a NIR photon (red arrows) creates the sidebands. Right: example of a RABBIT scan obtained in argon. When the time delay between the XUV and NIR fields changes, the amplitude of the sidebands oscillates at twice the frequency of the NIR field. The phase difference between different sidebands can provide information on the spectral phase of the attosecond pulses and the temporal dynamics of the atom.

Such a scan is shown in Figure 4.6. Harmonic peaks, separated by $2\hbar\omega_0$, are observed due to one-photon ionization from the harmonics. Two-photon ionization (XUV+NIR) leads to sidebands separated from the fundamental peaks by $\hbar\omega_0$. The energy of each sideband, q, can be reached by two different paths: absorption of one XUV photon from harmonic $q-1$ and absorption of one NIR photon or the absorption of one XUV photon from harmonic $q+1$ and the emission of one NIR photon. The two paths interfere and, as a result, the amplitude of the sidebands, SB, shows a periodic modulation with the time delay Δt between the XUV and the NIR pulses [117, 118]:

$$SB = A\cos(2\omega_0\Delta t - \Delta\phi_q - \Delta\phi_{\text{atom}}) \tag{4.17}$$

where A depends on the matrix dipole moments between the initial and final states, $\Delta\phi_q = \Delta\phi_{q+1} - \Delta\phi_{q-1}$ is the phase difference between the harmonics $q+1$ and $q-1$, and $\Delta\phi_{\text{atom}}$ is the intrinsic phase difference of the matrix elements corresponding to photoionization from the harmonics $q+1$ and $q-1$.

To characterize XUV pulses temporally, the phase difference between harmonics, $\Delta\phi_q$, is required. The intrinsic phase, $\Delta\phi_{\text{atom}}$, can be calculated precisely for a suitable

choice of target gas. Furthermore, its contribution is usually small. In this case, it is possible to extract the phase difference between consecutive harmonics, $\Delta\phi_q$, over the full harmonic spectrum from the RABBIT scan.

On the other hand, to study photoionization dynamics, one is interested in the intrinsic phase, $\Delta\phi_{\text{atom}}$. Photoemission time delays can be measured relatively if electrons are ionized from two different shells (e.g. $3s$ and $3p$ in argon). Then $\Delta\phi_{\text{atom}}$ will vary depending on the state from which the recorded electrons originated, while $\Delta\phi_q$ can be independently measured for each harmonic. Therefore, the RABBIT scan will yield, in this example, $\Delta\phi_{\text{atom}_{3s}} - \Delta\phi_{\text{atom}_{3p}}$.

4.4.2 Spectral phase measurements of a Fano resonance

During photoionization due to electron correlation, an electron can first be excited to a resonant bound state with an energy higher than the ionization potential, before it is spontaneously released into the continuum. This phenomenon is called autoionization. Electrons that have passed through this resonant state will interfere with electrons that were directly ionized. This results in a characteristic spectral line shape, called a Fano resonance [119]. The effect of the $3s^2 3p^6 \rightarrow 3s^1 3p^6 4p$ autoionizing resonance in argon on the photoemission time delay was investigated by measuring the spectral phase of the continuum wave-packet close to a Fano resonance (Paper V).

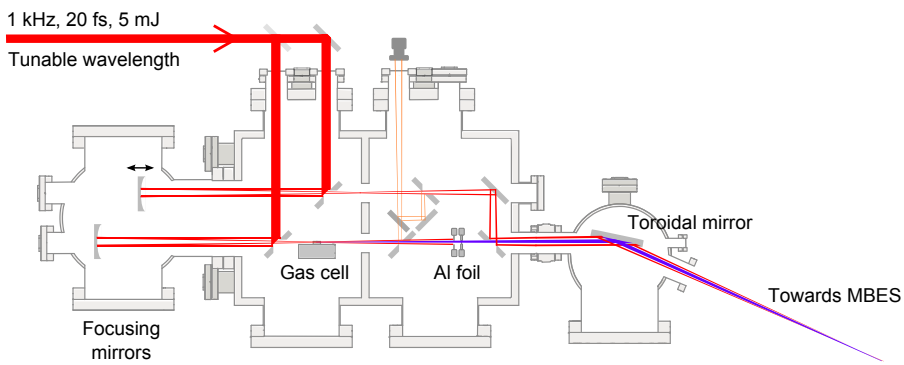

Figure 4.7: Schematic of the setup used for HHG and RABBIT (Paper V). The red lines indicate the NIR beams, the purple lines the XUV beam, and the orange lines the interferometer used to stabilize the XUV/NIR time delay. Al: aluminium, MBES: magnetic bottle electron spectrometer. (Chamber drawing courtesy of Samuel N. Bengtsson.)

The measurement was performed using NIR pulses from the laser system presented in Section 1.2.2. These pulses have a tunable wavelength with a range up to 50 nm for a reduced bandwidth of about 50 nm. The full setup for RABBIT is shown in Figure 4.7. The NIR pulses were directed into a Mach–Zehnder interferometer. In one of the arms, HHG was performed in an argon pulsed-gas cell. After HHG a 200 nm thick aluminium foil was used to filter out the remaining fundamental field from the XUV. In the other arm, a weak portion of the NIR field was selected and directed through a delay stage. The XUV and the NIR pulses were collinearly recombined with a tunable, stabilized, delay. Both were sent into a diffusive gas target for the

RABBIT measurement. The photoionized electrons were then collected in a magnetic bottle electron spectrometer.

To measure the phase of the Fano resonance, the wavelength of the NIR field was tuned in order to scan the resonance with harmonic 17. The interference with the resonant state induced dephasing of sidebands 16 and 18 (see Figure 4.8). When harmonic 17 was detuned far off the resonance, $\Delta\phi_q - \Delta\phi^{\text{atom}}_{\text{off-resonance}}$ could be measured for sidebands 16 and 18, where $\Delta\phi_q$ mainly represents the chirp of the attosecond pulses and $\Delta\phi^{\text{atom}}_{\text{off-resonance}}$ the intrinsic phase in the absence of resonance.

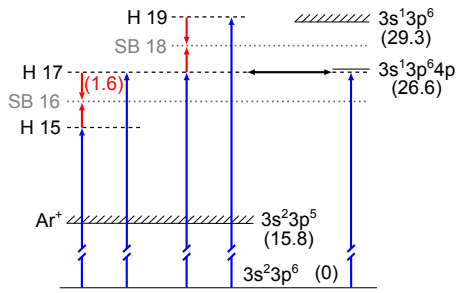

Figure 4.8: Energy diagram of argon showing the different states, channels and processes involved in the measurement of the phase of the autoionizing resonance. The blue arrows indicate absorption at the harmonic frequencies. The red arrows indicate the absorption or emission of a NIR photon. Energies (in eV) are given in brackets. The black arrow indicates the decay of the resonant state by autoionization. (Figure from Paper V.)

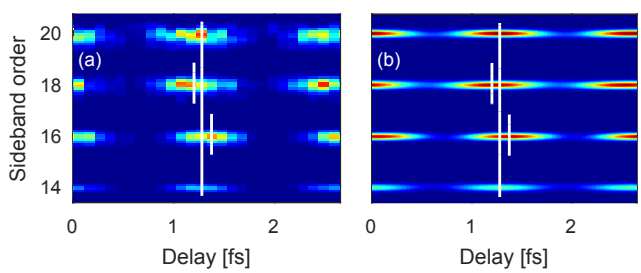

Figure 4.9: a) RABBIT scan on a Fano resonance. The spectral contribution of the harmonics has been removed for clarity, leaving only the sidebands. The scan is also corrected for the harmonic phase (mainly chirp) and the intrinsic phase off-resonance, which is why sidebands 14 and 20, which are not affected by the resonance, are in phase in this scan. The central energy of harmonic 17 is 26.63 eV, which is on the $3s^2 3p^6 \rightarrow 3s^1 3p^6 4p$ autoionizing resonance in argon. Sidebands 16 and 18 are strongly affected by the resonance, towards positive delays for sideband 16 and the opposite way for sideband 18. b) Theoretical calculations based on a two-photon resonant model [92]. This model uses the formalism developed by Fano to account for the autoionization, and generalizes it to include the influence of the weak NIR field, in the perturbative limit. Further details on these calculations are given in Paper V. These calculations are in good agreement with the experimental data. (Figure from Paper V.)

When harmonic 17 is tuned onto the resonance, dephasing is induced, which can

be seen as an additional phase, ϕ_{Fano}, contributing to the sideband modulation:

$$SB = A\cos(2\omega_0\tau - \Delta\phi_q - \Delta\phi^{\text{atom}}_{\text{off-resonance}} - \phi_{\text{Fano}}) \tag{4.18}$$

Since $\Delta\phi_q - \Delta\phi^{\text{atom}}_{\text{off-resonance}}$ was measured previously, it can be corrected to give only the additional phase induced by the resonance ϕ_{Fano}.

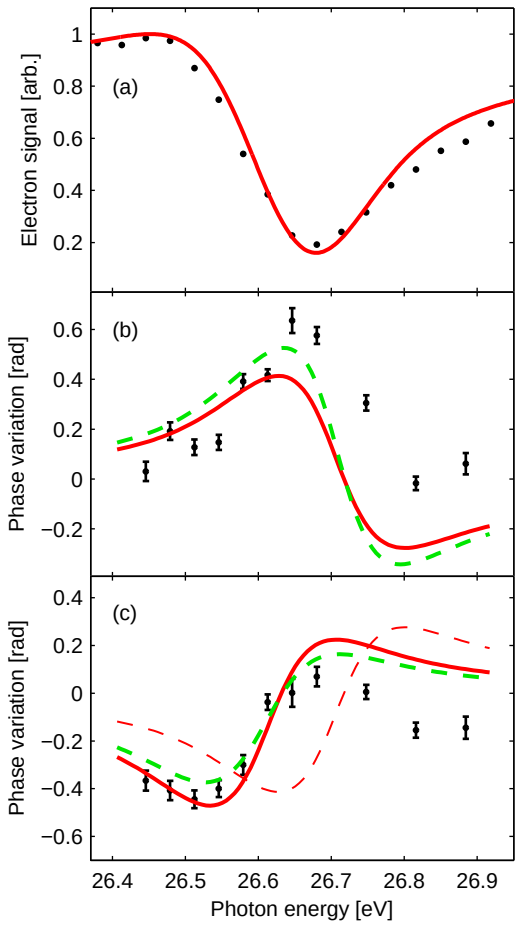

Figure 4.10: Spectral intensity (a), and phase (b) and (c), of the $3s^2 3p^6 \rightarrow 3s^1 3p^6 4p$ autoionizing resonance in argon. The black symbols represent experimental results and the red and green curves theoretical calculations based on the two-photon resonant model. (Further details about these calculations are given in Paper V.) a) Photoionization signal as a function of the photon energy of harmonic 17. b) Phase variation of sideband 16. c) Phase variation of sideband 18. The dashed red line is the opposite of the red line for sideband 16 which, apart from an energy shift, is close to the results for sideband 18. (Figure from Paper V.)

A RABBIT scan with harmonic 17 tuned to the Fano resonance is shown in Figure 4.9. The fundamental peaks have been removed, and $\Delta\phi_q - \Delta\phi^{\text{atom}}_{\text{off-resonance}}$ has been corrected for all harmonics, leading to the sidebands not affected by the resonance (14 and 20) being perfectly in phase. Therefore, the remaining dephasing of sidebands 16

and 18 directly gives ϕ_{Fano} for the photon energy of harmonic 17. Figure 4.10 shows the amplitude of harmonic 17 and ϕ_{Fano} for sidebands 16 and 18, as a function of the energy of harmonic 17.

Such a measurement provides complete characterization, both in phase and amplitude, of the electron interaction between a discrete state and the ionization continua, paving the way for future control of such interactions.

4.5 Generation of isolated attosecond pulses by noncollinear optical gating

The periodicity of the HHG process with the driving field leads to a pulse train in the temporal domain and a frequency comb of odd harmonics in the spectral domain. When the driving field has a duration of a few cycles, fewer attosecond pulses are generated, and the frequency comb is smeared out, i.e., each harmonic becomes spectrally wider. A continuous spectrum is obtained if the HHG process is confined to a single event. In the temporal domain, this corresponds to an IAP.

The continuous broadband spectrum of IAPs makes them the ultimate tool for attosecond science. They are typically used in XUV-pump–NIR-probe schemes together with the fundamental NIR field. IAPs are, for example, ideally suited for transient absorption measurements [120]. However, the interpretation of some pump–probe measurements, such as streaking [121], can be difficult since the intense NIR field can induce strong-field processes. An ideal experiment would consist of using IAPs for both pump excitation and the time-delayed probe (XUV-pump–XUV-probe) [122]. However, due to the experimental difficulties in generating two IAPs with sufficient intensity and a controllable delay, this scheme has only been used in a few experiments [123–125].

4.5.1 Generation of IAPs

To generate IAPs, the HHG process must be confined to a single event. Therefore, it would be necessary to drive the HHG with single-cycle NIR pulses with a stable CEP equal to 0 or π. However, such pulses are very difficult to produce. An alternative would be to use few-cycle NIR pulses together with gating of the harmonic radiation or of the harmonic generation process.

The principles of the main gating techniques can be divided into three categories: spectral, temporal and spatial gating. Several reviews on these techniques can be found in the literature [126–129].

Spectral gating

The first IAPs were generated [130] immediately after the first demonstration of attosecond pulse trains. This was achieved using the amplitude gating technique [131]. The cut-off section of the harmonic spectrum corresponds to the attosecond pulse generated by the most intense half-cycle of the driving field. Therefore, it is possible to select an IAP, by spectrally selecting the cut-off region.

Temporal gating

The idea behind temporal gating is to produce an ultrashort window, shorter than a half-cycle of the driving field (or a complete cycle in the case of two-colour excitation), in which HHG is allowed. Several schemes can be used to produce such a window.

Polarization gating is based on the strong dependence of the HHG process on the polarization of the driving field. The generation efficiency decreases strongly with ellipticity since, for such polarization, the electron wave packet that tunnelled into the continuum cannot be brought back to its parent ion by the driving field. If a pulse has a time-dependent polarization state [132], i.e. circularly polarized on the edges and linearly polarized in the centre, only the central peak of the pulse will yield harmonic radiation. Pulses with a time-dependent polarization state can be created by combining two perpendicularly polarized pulses with slightly detuned frequencies or, in a simpler manner, with single-colour pulses together with two birefringent plates [133]. Double-optical gating (DOG) and generalized DOG lower the requirement on polarization gating by increasing the separation between the generation of two consecutive attosecond pulses to a full cycle of the driving field. This is done by driving the HHG using two-colours: the fundamental field and its second harmonic [134, 135].

Ionization gating is based on the use of the ionization of the generation medium by the intense driving field. The plasma density increases rapidly on the leading edge of the pulse, creating a phase mismatch, suppressing HHG for all the following half-cycles [136].

Spatial gating

Another approach for the generation of IAPs is to generate an attosecond pulse train, in which each pulse propagates in a different direction, and to spatially filter the XUV radiation to select an IAP. XUV pulses are emitted in the instantaneous propagation direction of the driving field, therefore, if the wavefront of the driving laser rotates with time, consecutive XUV pulses will be emitted in slightly different directions. Two different methods have been demonstrated for the generation of such a wavefront rotation (WFR). In the attosecond lighthouse (ALH) [121, 137–139], the WFR is generated by focusing an angularly chirped field, achieved by, e.g., tilting a glass wedge in the beam. In NOG [98], the WFR is generated by noncollinearly focusing two identical, delayed pulses.

All the gating techniques place strict requirements on the driving pulses. Firstly, to ensure a sufficiently short gate, few-cycle pulses are required. This requirement can be relaxed by combining different gating techniques (e.g. DOG). Secondly, since the HHG process is confined to a single event, the CEP stability of the driving pulses is critical. For spatial gating, additional restrictions are placed on the spatial-temporal pulse distortions as spatio-temporal coupling is used through the WFR.

4.5.2 NOG

NOG, proposed by C. M. Heyl et al. [98] and demonstrated in the experiment reported in Paper III, is based on an angular streaking concept [121], similar to the ALH [137], providing IAPs angularly separated from the fundamental field, and whose direction of emission can be controlled by the CEP of the driving pulses.

Figure 4.11 shows the main principle of NOG. Two identical, temporally delayed, pulses are noncollinearly superimposed in the generation medium, resulting in a field with ultrafast WFR driving the HHG. XUV pulses are emitted perpendicularly to the instantaneous wavefront direction, and consecutive pulses are thus emitted in slightly different directions. As a result, the pulse train is angularly streaked over the angle sector $[-\gamma, \gamma]$, where 2γ is the small noncollinear angle, and IAPs, naturally separated from the fundamental field, can be selected by spatial filtering.

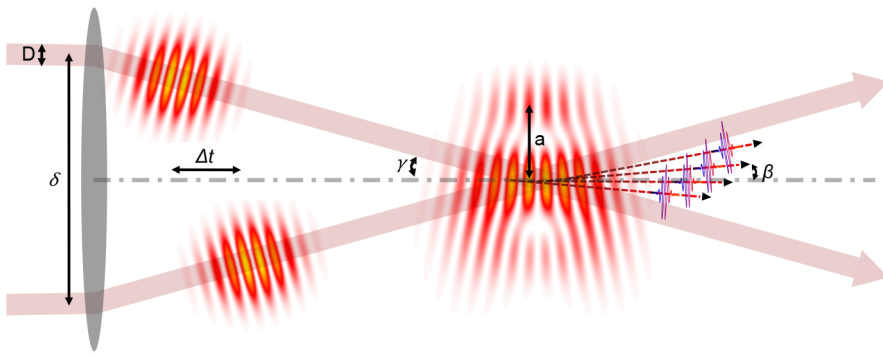

Figure 4.11: Schematic illustrating NOG. A few-cycle pulse and its temporally delayed replica are noncollinearly focused into a medium for HHG. Their interference in the medium leads to an ultrafast WFR. Consecutive attosecond pulses, originating from different half-cycles of the driving field, are emitted in different directions following the wave front angle. The attosecond pulse train is streaked across the angle sector $[-\gamma, \gamma]$ leading to a wide angular spread of the emitted XUV radiation.

WFR

When two identical pulses are superimposed at the position of the geometrical focus, their interference results in a transverse intensity grating with periodicity:

$$a \approx \frac{\lambda}{2\gamma} \tag{4.19}$$

The transverse envelope of the grating corresponds to the focal spot size of either pulse (w_0 at $1/e^2$). Such gratings are shown in Figure 4.12 for different initial conditions.

The transverse intensity grating collapses into a single maximum with weak satellites when its periodicity is approximately equal to its transverse envelope width ($a \approx w_0$). This corresponds to a spatial separation between the two fundamental pulses, before focusing, of $\delta \approx \pi D/2$ (independent of the focal length), where D is the diameter at $1/e^2$ of either beam. At complete temporal overlap, HHG will lead to an attosecond pulse train being emitted along the bisector angle of the two fundamental beams, i.e., the optical axis. If a temporal delay is introduced, the wavefront direction will rotate with time, and the XUV emission will be angularly streaked, mapping time into spatial position in the far field.

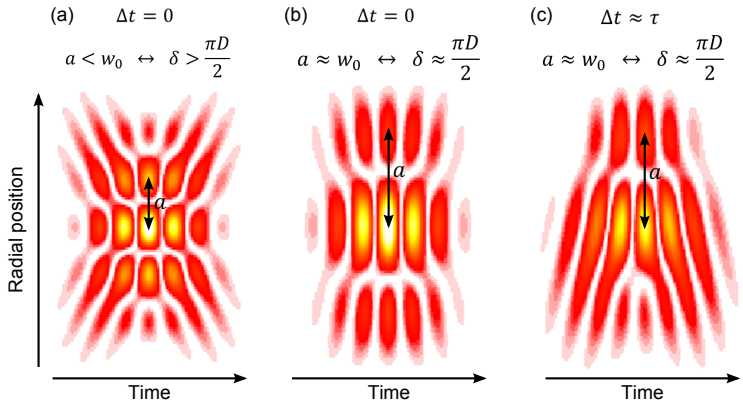

Figure 4.12: Different intensity gratings generated in different noncollinear focusing conditions. When such a grating is used to drive HHG, each peak with sufficient intensity will emit an attosecond pulse in the direction perpendicular to its wavefront. a) Two identical pulses, with considerable spatial separation, are simultaneously focused. The resulting transverse intensity grating, at the position of the geometrical focus, has a periodicity smaller than its transverse envelope ($a < w_0$). Such a grating will generate several attosecond pulse trains, spatially separated by a and collinearly propagating. b) Two identical pulses, with a spatial separation of $\delta \approx \pi D/2$, are simultaneously focused. The resulting transverse intensity grating, at the position of the geometrical focus, has a periodicity close to its transverse envelope width ($a \approx w_0$). Such a grating will only generate one pulse train along the optical axis. c) Two identical pulses, with a spatial separation of $\delta \approx \pi D/2$ and a temporal delay of about their pulse duration ($\Delta t \approx \tau$), are focused. The resulting transverse intensity grating, at the position of the geometrical focus, exhibits an ultrafast WFR, i.e., each intensity peak has a different wavefront direction. Such a grating will generate an angularly streaked pulse train, i.e., each pulse is emitted in a different direction.

The wavefront rotation angle can be expressed as a function of temporal overlap:

$$\beta(t, \Delta t) = \gamma \frac{1 - \xi(t, \Delta t)}{1 + \xi(t, \Delta t)} \tag{4.20}$$

where $\xi(t, \Delta t) = \mathcal{E}_2/\mathcal{E}_1$ is the ratio of the amplitudes of the two driving field envelopes $\mathcal{E}_{1,2}$.

The WFR resulting in the best gating is achieved for $\Delta t \approx \tau$ [98] (provided that both pulses are in phase), where τ is the pulse duration (FWHM) of the fundamental pulses.

Method and results

Figure 4.13 illustrates the experimental setup used to demonstrate NOG (Paper III). Ultrashort pulses from the first hollow-capillary post-compression system (see Section 2.6.2), with a pulse duration of 3.2 fs, were sent into an interferometer consisting of a dispersion-balanced beam splitter and two translation stages to separate the beams both spatially and temporally. After the interferometer, the pulses enter vacuum and are focused with a curved mirror (f = 400 mm) into an argon gas cell, where HHG

takes place. A flat-field XUV spectrometer was used to record, in the far field, the XUV intensity as a function of energy and propagation angle.

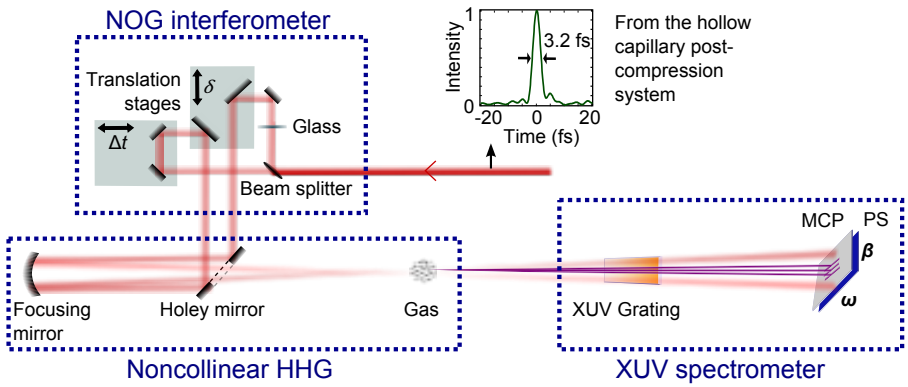

Figure 4.13: Schematic of the NOG experimental setup (Paper III). Ultrashort pulses from a hollow-capillary post-compression system are sent into an interferometer where they are split into two, and the resulting pulses are spatially and temporally separated using two translation stages. A glass plate was inserted in one arm to compensate for the dispersion of the beam splitter. Both pulses are focused, using the same curved mirror ($f = 400$ mm), into an argon gas cell for HHG. The XUV radiation was observed with a XUV spectrometer consisting of a curved grating, to spatially separate different energies in one direction and focus the harmonics in the other, and a 2D detector, consisting of a multichannel plate (MCP) and a phosphor screen (PS).

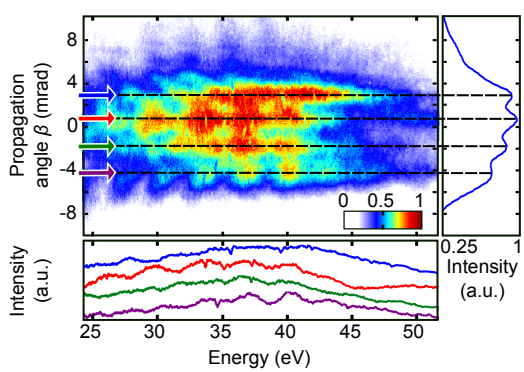

Figure 4.14: Results of a measurement showing several spatially separated IAPs. Main panel: measured angularly resolved far-field XUV spectrum under gating conditions ($|\Delta t| \approx T$). Right panel: spectral integration of the spatial profile. Bottom panel: line-outs taken along the black dotted lines indicated by the coloured arrows. (Figure from Paper III.)

For the extremely short pulses used in this experiment, the best gating was obtained for $\Delta t \approx \pm T$, where T is the cycle period. The attosecond pulse train was angularly streaked over the angle sector $[-\gamma, \gamma]$, with $\gamma = 7.3$ mrad. The wide angular spread of the XUV emission led to spatially separated IAPs on the detector. The fundamental pulses continued to propagate along $\pm\gamma$, thus being naturally separated

from the XUV emission and there was no need for spectral filtering. Figure 4.14 shows a measured spectrum under gating conditions. Several emission maxima with almost continuous spectra are visible, indicating the detection of several spatially separated IAPs.

Delay dependence

The dependence of the gating on the temporal delay between the two driving pulses was investigated (Paper III). Simulations of the time-to-space mapping, achieved by the WFR, as a function of delay, were performed.

Let us consider the total driving electric field on-axis:

$$E = E_1 + E_2 \tag{4.21}$$

with

$$E_{1,2} = \mathcal{E}_{1,2} \exp\left[i(\omega_0 t \pm \Delta t/2) + \phi_{\mathrm{CE}}^{1,2}\right] \tag{4.22}$$

where $\phi_{\mathrm{CE}}^{1,2}$ denote the CEPs of the two fundamental pulses, and $\mathcal{E}_{1,2}$ their assumed Gaussian envelopes:

$$\mathcal{E}_{1,2} = \exp\left[-2\ln 2\frac{(t \pm \Delta t/2)^2}{\tau^2}\right] \tag{4.23}$$

The temporal distribution of the electric field $|\Re[E(t)]|$ can be mapped onto its angular distribution $|\Re[E(\beta)]|$ using the mapping function $\beta(t)$ introduced in Equation 4.20. Such mapping will give the driving field intensity as a function of the angle at which the XUV pulses would be emitted.

Figure 4.15 shows this time-to-space mapping as a function of the temporal delay, together with a measurement of the XUV emission, integrated over energy, as a function of the temporal delay. It can be seen that for long delays (no temporal overlap), each driving pulse will emit an attosecond pulse train along its direction of propagation, i.e., $\pm\gamma$. Under gating conditions, i.e., around $\Delta t = T$, the XUV emission is angularly streaked. At complete temporal overlap, an intense attosecond pulse train is emitted along the optical axis.

CEP dependence

The direction of emission of the IAPs can be controlled by the CEP of the fundamental laser pulses. An identical change in CEP for both pulses leads to a temporal shift of the driving field maxima and, due to the time-to-space mapping process, results in an angular shift in the direction of XUV emission.

Figure 4.16 shows the impact of a change in CEP on the angular streaking. Comparing the first angular electric field distribution map with the map in Figure 4.15 shows that an identical change in CEP for both fundamental pulses leads to an angular shift of the XUV emission, in opposite directions for negative and positive delays. The measured CEP scan further demonstrates this dependence, as a clear downward shift of the XUV emission maxima is observed as the CEP decreases. The second map shows that a different change in CEP for the fundamental pulses leads to a shift in the best gating position with respect to the time delay and a modification of the XUV angular spread for the best gating.

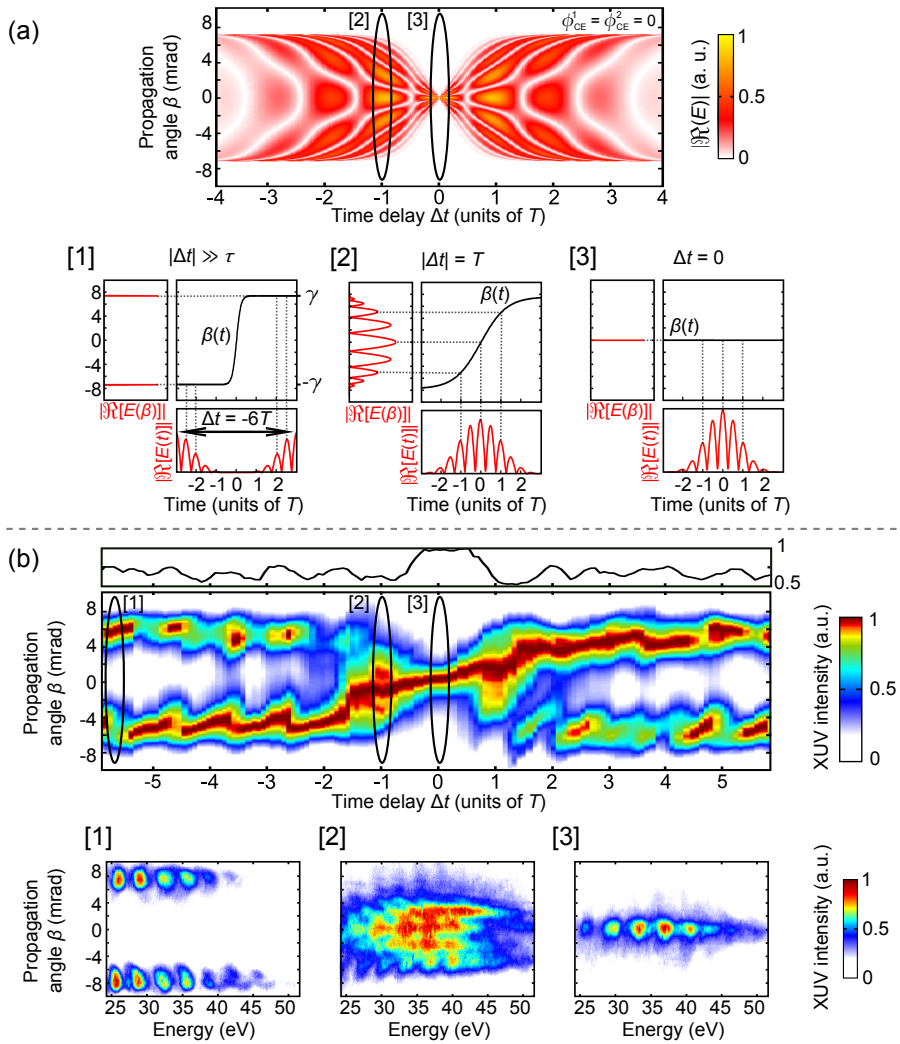

Figure 4.15: Dependence of NOG on the temporal delay for $\tau = 3.2$ fs, $\phi_{\mathrm{CE}}^{1,2} = 0$ and $\gamma = 7.3$ mrad. a) Angular electric field distribution map showing $|\Re[E(\Delta t, \beta)]|$, i.e., the driving field intensity as a function of time delay and the angle at which XUV pulses would be emitted. The insets display the time-to-space mapping for three characteristic values of the time delay. b) Measured spectrally integrated XUV emission as a function of time delay. Each vertical line-out shows an angularly resolved XUV spectrum, spectrally integrated (25-50 eV) and normalized. The normalization factors are given in the top panel. The insets display measured XUV spectra for the three characteristic values of the time delay. Insets 1 and 3 show modulated harmonic spectra characteristic of attosecond pulse trains. Inset 2, on the other hand, shows continuous spectra indicating IAPs.

Comparison with the attosecond lighthouse

Both the ALH and NOG generate an angularly streaked attosecond pulse train by mapping time into space with an ultrafast WFR. However, the mapping function β

is different. For the ALH, it varies linearly with time, while for NOG it is nonlinear. Interestingly though, around $\beta = 0$ (and $\Delta t = \pm\tau$ for NOG), the streaking process is equally efficient for both techniques, i.e., the same $\partial\beta/\partial t$ and thus the same angular divergence can be expected. However, although the WFR speed is limited to that in ALH [137], it can be faster for NOG if $|\Delta t| > \tau$ and thus, better separation of the IAPs can be achieved (at the expense of intensity). To date, ALH and NOG are the only techniques producing several synchronized IAPs that could be used for XUV-pump–XUV-probe measurements. A unique advantage of NOG is that, due to its noncollinear geometry, the fundamental fields are naturally separated from the generated IAPs, relaxing the need for spectral filtering and thus saving photon flux.

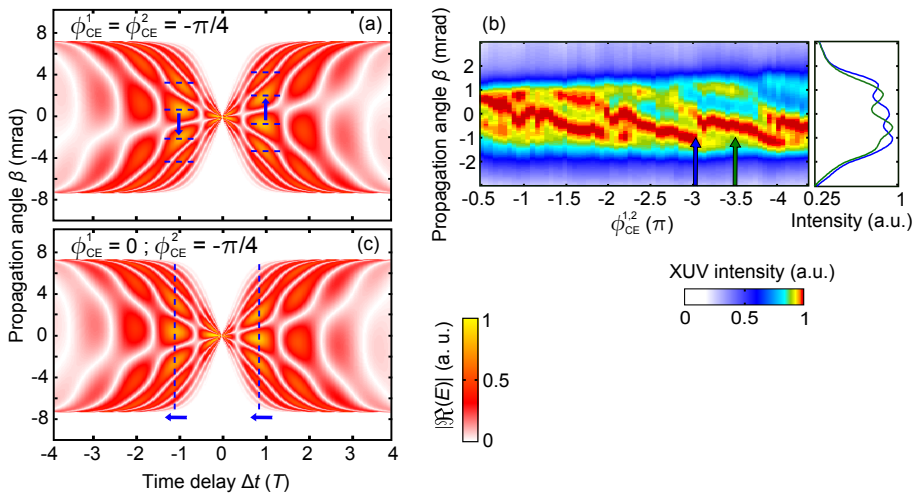

Figure 4.16: Dependence of NOG on the CEP. a) Angular electric field distribution map for $\phi^{1,2}_{\mathrm{CE}} = -\pi/4$. The direction of emission of the XUV pulses is angularly shifted. b) Measured spatially resolved XUV signal integrated over photon energy as a function of CEP, showing the angular shift of the XUV emission maxima as the CEP changes. The right panel shows two line-outs (location indicated by the arrows) with a difference in CEP of $\pi/2$. c) Angular electric field distribution map for $\phi^1_{\mathrm{CE}} = 0$ and $\phi^2_{\mathrm{CE}} = -\pi/4$. The best gating position is shifted with respect to the time delay. This shift leads to a change in the WFR speed for the best gating conditions and thus the angular separation of the emitted IAPs. For the best gating at negative delay, the emitted IAPs will have a greater angular separation than if the pulses were in phase. On the other hand, for best gating at positive delay, the separation will be smaller.

Applications

As shown in Figure 4.17, NOG allows to select one or two IAPs with the same far-field aperture by simply changing the CEP by $\pi/2$. The same setup could therefore be used to produce one IAP, for example, for XUV-pump–NIR-probe measurements or two synchronized IAPs, for example, for XUV-pump–XUV-probe measurements [122]. NOG is also a promising candidate for intra-cavity HHG [99, 100] since the fundamental fields propagate in a different direction from the XUV, providing the possibility for high-repetition-rate attosecond sources.

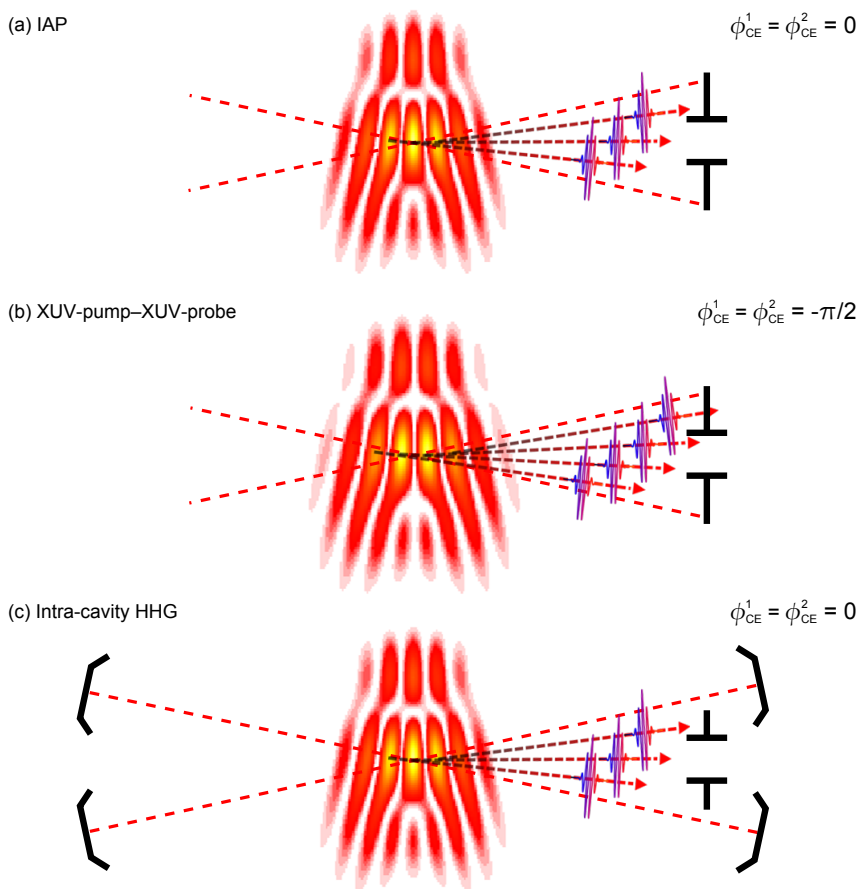

Figure 4.17: Schematic of some possible applications of NOG. a) Production of a single IAP. b) Selection of two synchronized IAPs for XUV-pump–XUV-probe measurements. c) Intra-cavity HHG.

Chapter 5

Summary and outlook

This thesis describes the work undertaken at the Attolab in Lund to routinely generate sub-4 fs NIR pulses, efficiently characterize them, and use them to generate IAPs.

A post-compression system, based on a gas-filled, hollow-core capillary together with a chirped-mirror compressor, was designed and implemented. Sub-4 fs pulses could be routinely produced. These pulses were used to demonstrate a novel gating technique (NOG) allowing the generation of several spatially separated, synchronized IAPs [Paper III]. The ultrashort femtosecond pulses were characterized using the d-scan technique.

Scaling-up of the energy in the post-compression and gating systems was investigated as a step towards increasing the XUV intensity. The scaling of the HHG process and post-compression by filamentation were investigated first. The scale invariance of these techniques was experimentally demonstrated, and a general model showing the scale invariance of most nonlinear optics phenomena in gases (including post-compression with a hollow capillary and NOG) was developed [Paper IV].

In light of these results, a scaled-up, hollow capillary post-compression setup was developed and implemented. Preliminary results, presented in this thesis, showed that sub-4 fs pulses could be routinely produced. A few modifications remain to be implemented (in the focusing system and vacuum chamber) before the system can achieve its full potential in terms of efficiency and input energy. The CEP stability was also analysed and significantly improved by the implementation of a feedback loop based on a CEP characterization performed behind the capillary. The pulses from the post-compression system were characterized with the d-scan technique, and were also used to experimentally test new developments of the d-scan. A new, faster retrieval algorithm was developed and demonstrated using these pulses together with pulses from an OPCPA system [Paper I]. A compact design for single-shot d-scans was developed and implemented using these pulses [Paper II].

The possibility to retrieve the CEP from a d-scan trace is currently being investigated. If the fundamental pulse and its second harmonic have some spectral overlap, interference fringes appear in the d-scan trace. If the SHG process can be accurately modelled, the CEP can be retrieved from the fringes. A measurement was attempted with the pulses from the first hollow-capillary setup but, unfortunately, the chirped mirrors that were used could not support the full bandwidth of the octave-spanning

spectrum necessary for such a measurement. Recent measurements, performed at the Department of Physics and Astronomy at the University of Porto, were, however, more conclusive, although some theoretical aspects still have to be resolved.

There are plans to improve the hollow-capillary post-compression system in the future so that we can exploit its full potential, i.e., reach the pulse energy predicted by the scaling. The pulses are expected to be sufficiently short and intense to generate IAPs with the ionization gating occurring naturally in the HHG gas cell. If necessary, another gating scheme will be added, possibly a scaled-up NOG scheme. The resulting IAPs will be characterized using the streaking technique and applied to interesting IAP-pump–NIR-probe experiments in the spirit of the one reported by J. Mauritsson et al. [140].

All the work presented in this thesis has been performed at the Attolab in Lund, with a laser source delivering 800 nm, 1 kHz, 5 mJ, 20 fs pulses. However, most of the findings are general and could be implemented in other laser systems.

The Attosecond Science group in Lund is also equipped with a high-repetition-rate OPCPA laser delivering 800 nm, 200 kHz, 5 μJ, sub-7 fs pulses. In such a system, complete pulse characterization is needed for day-to-day alignment of the noncollinear optical parametric amplification stages. At the present time, the conventional d-scan technique is used, but the implementation of a single-shot d-scan apparatus would allow instantaneous feedback (since the d-scan trace is sufficiently intuitive that a retrieval is not necessary for alignment optimization), greatly simplifying day-to-day alignment.

An interesting extension of the work presented in this thesis would be to apply the powerful scaling theory as a step towards the generation of high-energy IAPs that could be used for IAP-pump–IAP-probe measurements. In most pump–probe schemes used to investigate ultrafast processes, a NIR probe has been used. This is the case, for example, in the RABBIT technique, which was used to study the phase variation across a Fano resonance [Paper V]. For this technique a weak NIR field is used, but in other techniques, such as streaking [130], the dynamics initiated by the interaction of the attosecond pulse with, for example, molecules, may be concealed by that induced by the NIR field, since the intensities typically used for the NIR field can strongly distort a molecular potential [141]. One way of circumventing this problem in order to explore unaffected molecular dynamics may be to use XUV pulses for both the pump and the probe. Their short wavelength ensures that the ponderomotive energy induced by the XUV external field is negligible compared to the energy acquired through electron–electron and electron–nucleus interactions. The use of HHG to produce attosecond pulses for such experiments, would ensure a high temporal resolution. However, IAPs generated by HHG are usually so weak that such measurements are not possible.

Our group also has access to a high-intensity beamline delivering 800 nm, 10 Hz, 100 mJ, 45 fs pulses. Most of the achievements presented in this thesis seem almost impossible at such high energies. However, the demonstrated scale invariance of these phenomena opens the door for high-energy post-compression and IAP generation. Following the experiments performed in the Attolab demonstrating the scaling of filamentation, a project was initiated with the aim of scaling up filamentation in order to generate few-cycle pulses with energies greater than 4 mJ. As a step towards achieving that, a highly scaled-up filamentation setup has been installed on the high-intensity beamline with loose focusing ($f = 10$ m) in argon. This project is ongoing. A single-shot technique is needed to characterize the pulses generated due

to the low repetition rate. The single-shot d-scan technique was chosen since this can simultaneously compress the pulses. The resulting high-energy, few-cycle NIR pulses will be used for HHG. If this could be combined with a scaled-up NOG scheme, spatially separated but synchronized, high-energy IAPs could be produced, enabling IAP-pump–IAP-probe measurements.

Our group is also involved in designing a highly scaled-up, high-intensity HHG beamline for the Extreme Light Infrastructure Attosecond Light Pulse Source (ELI-ALPS) in Szeged. This beamline will be installed after the SYLOS laser system (Light Conversion and Ekspla consortium) delivering about 950 nm, 1 kHz, up to 100 mJ, sub-5 fs pulses. NOG could be a very interesting gating scheme for IAP-pump–IAP-probe measurements.

Important progress has been made towards the generation of ultrashort pulses, and the possibility to scale up the nonlinear phenomena involved promises a bright future, where ultrashort pulses generation, in the femtosecond and attosecond regimes, can follow the fast development of femtosecond laser sources.

Appendix - Design and implementation of a hollow-capillary system

Introduction

This appendix provides details on the design, construction and operation of a gas-filled, hollow-core capillary post-compression system. It is not a synthesis of work published elsewhere, but presents a practical guide, based on our experience, for others wishing to construct their own system.

A hollow-capillary post-compression setup relies on three main components. The first is a focusing system to couple the laser beam into the capillary, the second is the capillary itself, and the third is a compressor that compensates for the chirp of the spectrally broadened pulses. In this appendix, information will be given on how to design, construct and align the two first components.

Coupling into the capillary

Coupling the laser beam into the capillary is the most critical part of a hollow-capillary setup, since it has a considerable impact on the efficiency of the system. The more energy coupled into the fundamental mode of the capillary; the more energy transmitted. As was seen in Section 2.3.1, the lowest loss mode of a capillary is the EH_{11} hybrid mode. A coupling efficiency of up to 98 % can be achieved when the laser beam is perfectly aligned with the whole capillary and focused to a perfect Gaussian with a waist of $0.65a$, where a is the inner radius of the hollow capillary.

The focusing system

Focal length

To focus the beam to the best dimensions for coupling, it is important to choose the appropriate focal length. For a Gaussian beam, the size of the waist at the focus, w_0, is related to the focal length, f, and the beam waist before focusing, w_L, by the simple relation:

$$w_0 = \frac{\lambda f}{\pi w_L} \tag{5.1}$$

Inserting $w_0 = 0.65a$ gives the desired focal length.

$$f = 0.65a\frac{\pi w_L}{\lambda} \tag{5.2}$$

However, the laser beam is often not a perfect diffraction-limited Gaussian. In this case, the focusability of the beam must be taken into account. This can be done by inserting the beam quality factor, M^2, into Equation 5.2:

$$f = 0.65a\frac{\pi w_L}{\lambda}\frac{1}{M^2} \tag{5.3}$$

Therefore, when designing the focusing system, it is necessary to measure the beam waist before focusing and the quality factor of the laser beam.

Focusing optics

The most straightforward way to focus a laser beam is to use a lens. Lenses are easy to align and do not generate astigmatism. However, at high power, nonlinear interactions, such as self-focusing, start to take place in the lens, leading to a power dependence of the focal length, which can be problematic in coupling into the capillary. A spherical mirror can be used to overcome this issue, but a single mirror must be placed at an angle, and will thus generate astigmatism, which will degrade the quality of the coupling. To avoid this, two curved mirrors can be used in a detuned telescope designed to minimize astigmatism (Figure A.1).

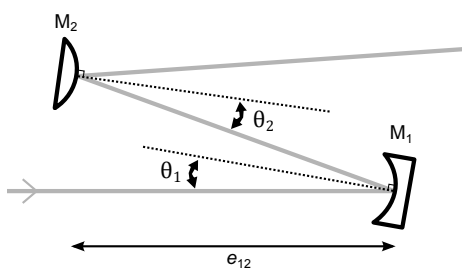

Figure A.1: The focusing telescope will be astigmatism-free if the angles of incidence, θ_1 and θ_2, are chosen appropriately.

It is possible to design an astigmatism-free telescope by setting the angles of incidence on the curved mirrors such that the astigmatism induced by the first mirror is compensated for by the second mirror. The total focal length, F, of a two-mirror telescope can, to a good approximation, be obtained from the radii of curvature of the mirrors, R_1 and R_2, and the distance e_{12} between them.

$$\frac{1}{F} = \frac{1}{2R_1} + \frac{1}{2R_2} - \frac{e_{12}}{4R_1R_2} \tag{5.4}$$

When a curved mirror is used off-axis, two different foci will be observed due to astigmatism: the tangential and the sagittal focus. For an angle of incidence θ, the effective radii of curvature for the tangential plane, R_T, and the sagittal plane, R_S,

are related to the radius of the mirror, R:

$$R_{\mathrm{T}} = R\cos\theta \tag{5.5a}$$

$$R_{\mathrm{S}} = \frac{R}{\cos\theta} \tag{5.5b}$$

Therefore, the total focal length of the telescope in the tangential and the sagittal planes will be:

$$\frac{1}{F_{\mathrm{T}}} = \frac{1}{2R_1\cos\theta_1} + \frac{1}{2R_2\cos\theta_2} - \frac{e_{12}}{4R_1R_2\cos\theta_1\cos\theta_2} \tag{5.6a}$$

$$\frac{1}{F_{\mathrm{S}}} = \frac{\cos\theta_1}{2R_1} + \frac{\cos\theta_2}{2R_2} - \frac{e_{12}\cos\theta_1\cos\theta_2}{4R_1R_2} \tag{5.6b}$$

where θ_1 and θ_2 are the angles of incidence on the first and second mirrors, respectively. For each set of parameters R_1, R_2, e_{12}, there are values of θ_1 and θ_2 such that $F_{\mathrm{T}} = F_{\mathrm{S}}$, thus leading to an astigmatism-free telescope.

Moreover, if the incident laser beam is already astigmatic, it is possible to choose θ_1 and θ_2 so that the telescope compensates for this astigmatism. It is necessary to measure the distance L_{TS} between the tangential and sagittal foci of the laser when focused with the astigmatism-free telescope. θ_1 and θ_2 can then be tuned so that $F_{\mathrm{S}} - F_{\mathrm{T}} = L_{\mathrm{TS}}$, and the telescope will compensate for the astigmatism of the laser.

Finally, regardless of the focusing optics chosen (a lens, a curved mirror or a detuned telescope), it is advisable to mount them on a breadboard that can slide along the optical axis, so that the position of the focus can be finely tuned to the position of the entrance of the capillary, to ensure the best coupling.

Alignment

The most critical aspect of the coupling is, without doubt, the alignment of the beam to the capillary. To the best of the author's knowledge, the most efficient way is still to align for the best mode. The parameters that must be optimized are: symmetry, homogeneity, broadening and output power. However, the quality of the mode can be different for different spectral regions; the blue part of the spectrum being most sensitive to alignment.

It is preferable to perform the alignment using a helium-neon (HeNe) laser first to avoid burning the tip of the capillary by directing too much power into the glass when not properly aligned. It is then recommended that the NIR beam be directed into the capillary under vacuum, to avoid the combination of nonlinear effects and misalignment effects. A transmission close to, but lower than, the value given by Equation 2.43 should be expected, as a result of additional losses due to coupling imperfections and absorption in the windows when entering and exiting the vacuum tube. Once aligned in vacuum, gas can be added and the alignment refined. The transmission should not fall drastically when the gas is added; this may be observed if the position of the capillary is affected by the pressure inside the tubes. This is mainly a problem when flexible bellows are used in the gas tubing. In such a case, complete alignment should be performed at one gas pressure and be repeated if the pressure is changed.

Alignment can be performed in two different ways: the beam can be aligned to the capillary, or the capillary can be aligned to the beam. If one chooses to align

the beam to a fixed capillary, two mirrors are needed after the focusing optics to walk the beam, so that both position and pointing can be tuned without changing the focusing conditions. The main problem associated with this method is that when trying to refine the alignment, it is easy to adjust the optics a little too far and loose the alignment completely. The second solution is better in this regard, but the mechanical implementation is more difficult. To align the capillary to the beam it is necessary to mount the capillary on translation stages. Horizontal and vertical translation of both ends of the capillary should be possible. Translation along the optical axis is not needed since this can be more easily implemented on the focusing system. The mounting designed to hold the vacuum tube in which the capillary is mounted is shown in Figure A.2. Such a holder should be placed at each extremity of the capillary.

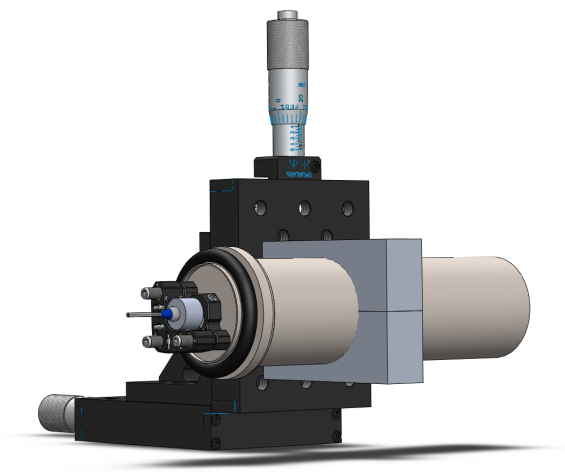

Figure A.2: Holder fixed on two translation stages enabling the alignment of the capillary to the beam. The two translation stages allow for horizontal and vertical translation of the KF40 tube in which the capillary is fixed. (Details on fixing the capillary in the tube can be seen in Figure A.8.)

The actual procedure for aligning the capillary is illustrated in Figure A.3 and is achieved in 7 steps:

1) Before the capillary is placed on the table, the laser beam is aligned. An iris is placed after the position where the capillary will be mounted and aligned to the laser. A HeNe laser is set to co-propagate with the NIR beam.

2) The capillary is placed on the table.

3) Initial alignment is performed with the HeNe laser:

   a) The entrance of the capillary is placed so that the beam couples in.

   b) The exit of the capillary is moved so as to align the output beam with the iris.

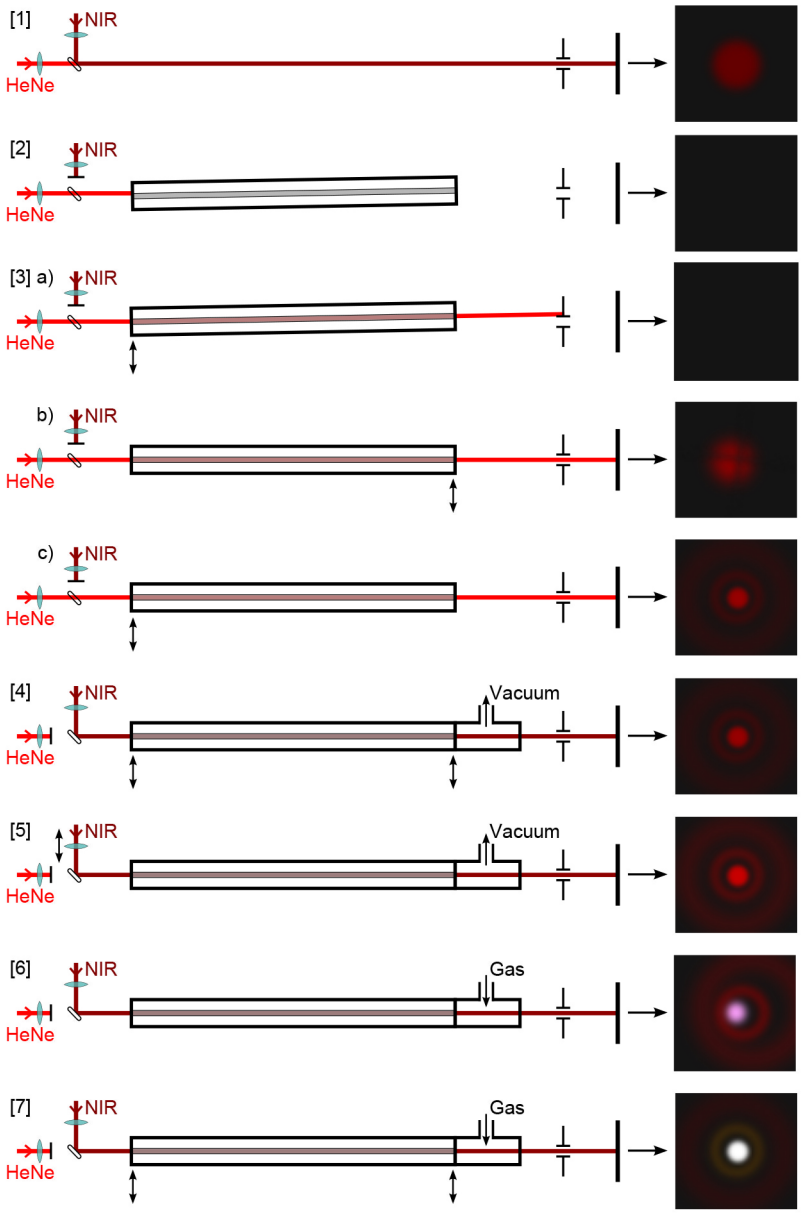

Figure A.3: Illustration of the procedure used to align the capillary.

c) The entrance of the capillary is adjusted again to optimize the mode.

4) The same procedure is performed with the NIR beam in vacuum.

5) The focusing system is moved along the optical axis to maximize the throughput.

6) Gas is added to the capillary.

7) The alignment is refined:

   a) The entrance of the capillary is adjusted to optimize the coupling and the broadening.

   b) The exit of the capillary is adjusted to optimize the mode.

   c) The two previous steps are repeated until satisfactory alignment is obtained.

Beam pointing stabilization

Since the alignment of the capillary is extremely sensitive, fluctuations in the beam pointing will have considerable effects on the quality of the coupling. Fluctuations can be caused by, for example, air flow through the laser chain or thermal drift of the beam. Shot-to-shot active stabilization of the beam makes a considerable difference in terms of the efficiency of the system and the stability of the output beam. In our experience, the generation of ultrashort pulses from our laser is almost impossible without it.

A beam stabilization system called Aligna from TEM Messtechnik was used in our setups. This consists of two motorized mirrors with piezo-driven actuators, detectors and control electronics. A feedback loop was implemented to suppress thermal drift and fast fluctuations, locking the beam pointing to sub-micrometre precision. An illustration of the beam stabilization system is shown in Figure A.4. One active mirror was placed just after the compressor at the end of the laser system, and the other before the capillary, as close as possible to it. The small leakage of the beam transmitted through the first dielectric mirror after the second active mirror was directed to the two detectors: one in the near field to measure the position of the beam, and one in the far field to measure its angle. Two additional mirrors used to align the beam to the capillary were placed before the capillary so that alignment could be performed with a stabilized beam. The Aligna system could self-learn the parameters for the feedback loop, making its implementation rather simple.

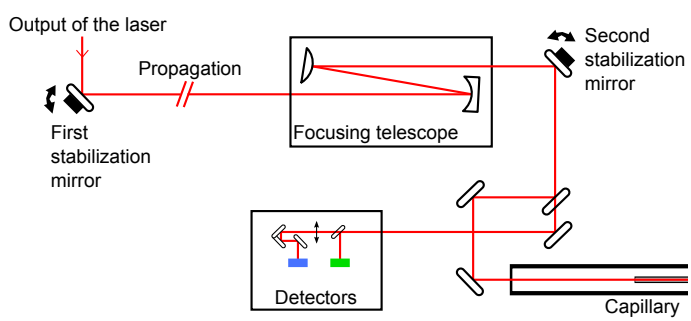

Figure A.4: Illustration of the beam stabilization system. The near-field detector is shown in green and the far-field detector in blue.

The Aligna system also stores the position and angle of the beam that have been set. The alignment of the beam relative to the capillary can be reproduced from day

to day using the motors of the actuators. The only realignment that may be necessary from one day to another is steps 6 and 7 of the alignment procedure described above.

The capillary

The capillary is the main component of the post-compression system. It is therefore important to choose the appropriate capillary and align it correctly to achieve the desired results.

Choosing the capillary

Before choosing the capillary, it is necessary to determine which gas will be used. The main limitation is self-focusing. For high-power lasers, such as that used in this work (3 mJ, 20 fs, 800 nm), it is not possible to limit the power to that under the critical peak power for self-focusing with any gas. Under these conditions, the best option is to use the gas with the lowest nonlinear refractive index, n_2 (i.e. helium), and to use differential pumping to avoid self-focusing in front of the capillary.

The inner radius of the capillary must then be decided. The main limitation here is ionization. It is desirable for the degree of ionization to be, at least, below 10 % to avoid plasma defocusing, but the inner radius should be as small as possible for maximum SPM.

The last parameter to be determined is the length of the capillary. The length mainly defines how much broadening will occur due to SPM, i.e., how short the generated pulses will be. A longer capillary should be chosen if differential pumping is used because the actual interaction length is reduced by the pressure gradient.

Moreover, since the nonlinear interactions in a capillary are scalable, a setup that has been proven to function well can be scaled up to the desired input energy.

Finally, the type of capillary must be chosen: a flexible fibre or a rigid capillary. The most important factor is keeping it straight. (This will be discussed in more detail below.)

The gas system

In order to fill the hollow core of the capillary with gas, the capillary must be mounted inside a vacuum-tight system connected to a gas bottle. Furthermore, to achieve differential pumping, the entrance side of the capillary must be connected to a pump and the exit side to a gas bottle.

Figure A.5 shows a possible system for differential pumping. The capillary is mounted in a KF40 tube in such a way that the gas can only travel from one end of the tube to the other through the hollow core of the capillary. The entrance of the capillary is connected to a transparent plastic tube so that the tip of the capillary is visible for alignment purposes. T-pieces connect the entrance side to a pump and the exit side to a gas bottle. The whole system is sealed by two fused silica windows allowing passage of the laser beam.

The windows must be placed sufficiently far from the capillary that the beam will be large enough, and thus the power low enough, to avoid nonlinear effects, such as self-focusing, in the windows. The minimum distance between the windows and

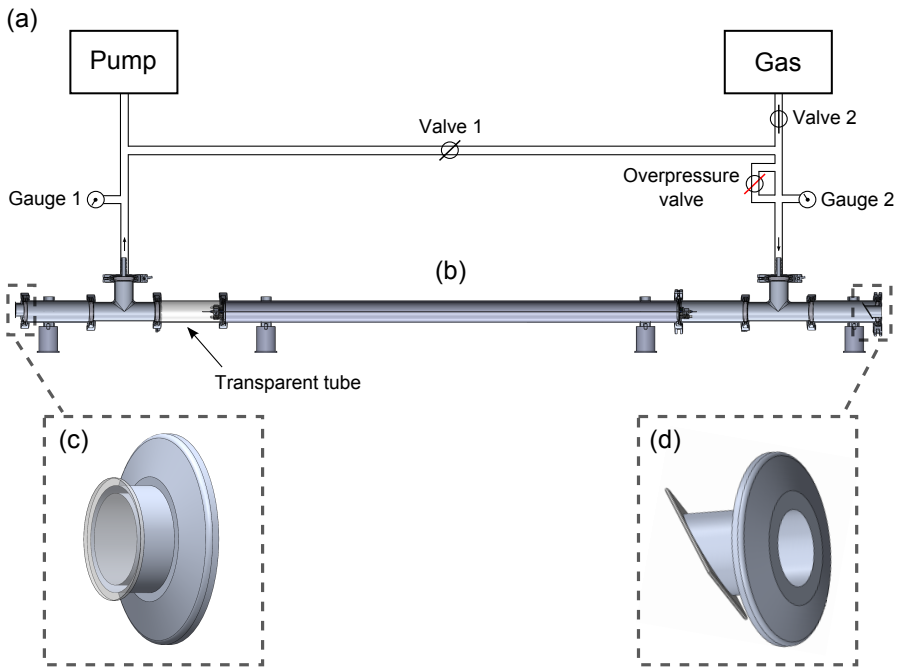

Figure A.5: a) Schematic of a possible gas system. b) Vertical cross section of a capillary mounted in KF40 tubes. c) The entrance window. d) The exit window mounted from the inside at Brewster angle.

the capillary can be determined by setting a limit on the nonlinear phase accumulated throughout the window, i.e., the B-integral (see Section 2.2.3). To avoid strong nonlinear effects, the B-integral must be less than 0.5. Neglecting absorption, the B-integral can be derived as:

$$B = \frac{2\pi}{\lambda_0} n_2 I_0 L \tag{5.7}$$

where n_2 is the nonlinear refractive index of the window (for fused silica, $n_2 = 2.48 \times 10^{-16}$ cm^2/W [142]) and L is the window thickness. For a 500 μm thick fused silica window, keeping the B-integral below 0.5 corresponds to a maximum intensity of $I_{0_{\max}} = 5.1 \times 10^{11}$ W/cm^2. For our laser (Gaussian beam, 3 mJ, 20 fs), this corresponds to a beam radius, at $1/e^2$ of the intensity, of $w_{\min} = 3.0$ mm.

Ray transfer matrices can be used to calculate the minimum distance between the first window and the capillary entrance:

$$d_{1_{\min}} = f \frac{w_{\min}}{w_L} \tag{5.8}$$

where f is the focal length with which the beam is focused into the capillary, and w_L is the beam radius before focusing (see Figure A.6). For $f = 4$ m and $w_L = 11$ mm, $d_{1_{\min}} = 107$ cm.

Using Gaussian optics, it is also possible to calculate the minimum distance between the second window and the capillary exit:

$$d_{2_{\min}} = z_{\mathrm{R}}\sqrt{1-\left(\frac{w_{\min}}{w_0}\right)^2} \tag{5.9}$$

where z_{R} is the Rayleigh length (see Equation 2.45), and $w_0 = 0.65a$ is the beam radius in the capillary. For $a = 175$ μm, $d_{2_{\min}} = 132$ cm. However, a longer distance should be chosen since self-focusing is likely to occur at the exit of the capillary, due to differential pumping, reducing the expansion rate of the beam.

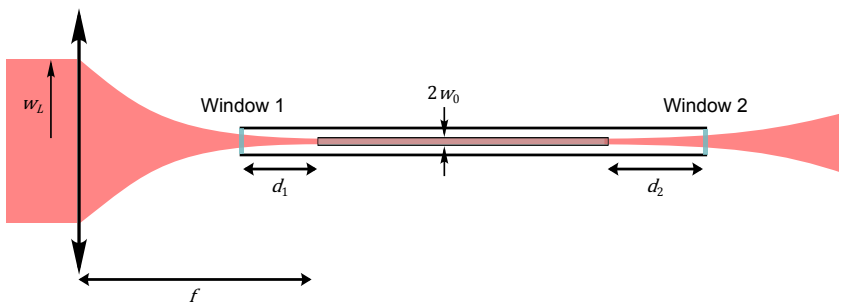

Figure A.6: Schematic of the capillary system with its windows, showing the dimensions used in the following calculations.

The entrance window has an anti-reflection coating for 800 nm. However, no such coating is possible on the exit window since we want to transmit the entire broadened spectral range. Therefore, the window is placed at Brewster angle. For helium and ultra-violet fused silica, the Brewster angle is 55.5°. The windows are simply glued onto the tubes. The exit window is glued from the inside of the tube so that the glue does not need to withstand the significant force resulting from overpressure.

Pressure gauges are placed on each side of the capillary setup to monitor the differential pumping. The pressure at the entrance should be as close to vacuum as possible, and at least below 1 mbar. A scroll pump is sufficient to achieve this pressure. The pressure at the exit side can be varied to optimize the spectral broadening. An overpressure valve is placed on the exit side for safety purposes. A hose connects both sides of the capillary setup so it is possible to by-pass the capillary by opening a valve (Valve 1 in Figure A.5). This is very useful to rapidly pump the whole system down to vacuum.

The system illustrated in Figure A.5 works very well, but does not allow the user to align the capillary to the beam. To be able to adjust the position of the capillary, the tube in which the capillary is mounted should not be rigidly connected to the rest of the system. Figure A.7 shows a system designed by our group, allowing alignment of the capillary to the beam. The tube in which the capillary is mounted is connected to the rest of the system by two flexible connectors, i.e., spring bellows. However, spring bellows deform with changing pressure, thus moving the capillary when the pressure is varied. Special holders were therefore designed, preventing movement along the optical axis, but allowing tilt and movement in the perpendicular plane. One such holder is illustrated in Figure A.7. The holder is fixed to the table with a base large

enough to withstand the force of the gas pressure. Three large screws connect the base to a hard plastic ring with an inner diameter greater than that of the tube, to allow movement in the x-y plane, but smaller than the clamp so it can rest against it preventing the capillary from moving in the opposite direction. The holder can be roughly aligned using the three large screws. A ball is fixed to the tip of each screw with a spring, allowing the tube to be tilted.

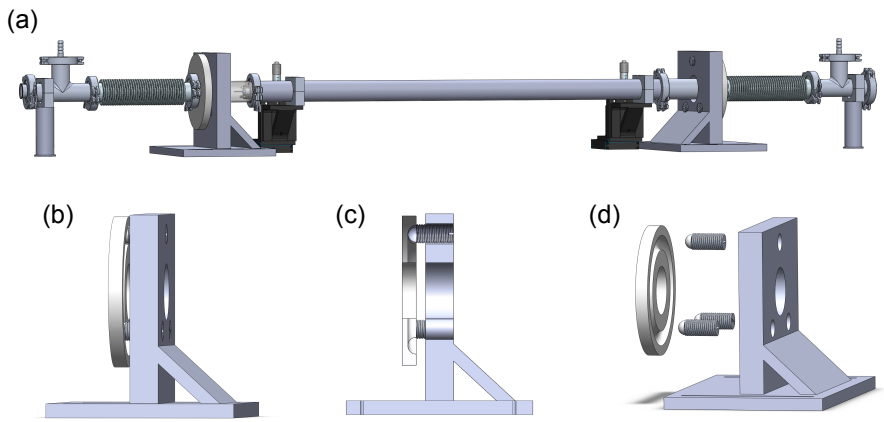

Figure A.7: a) System allowing the capillary to be moved. b) Special holder preventing movement along the optical axis, but allowing tilt and translation in the perpendicular plane. c) Vertical cross section of the holder. d) The various components of the holder.

Straightening of the capillary

Losses due to curvature

If the capillary is not kept straight, serious losses will arise [143]. The overall attenuation constant, α, of a capillary can be written as the sum of the attenuation constant of a straight capillary, α_0, and of the attenuation due to curvature, α_R.

$$\alpha = \alpha_0 + \alpha_R \tag{5.10}$$

As seen in Section 2.3.1:

$$\alpha_0 \sim \frac{\lambda^2}{a^3} \tag{5.11}$$

If R is defined as the radius of curvature of the capillary so that a straight capillary has $R \to \infty$, it can be shown [46] that:

$$\alpha_R \sim \frac{1}{R^2}\frac{a^3}{\lambda^2} \tag{5.12}$$

Thus, the lower the attenuation of a capillary; the higher its sensitivity to curvature.

Moreover, it has been shown that losses of the fundamental mode increase more rapidly with curvature than losses of the higher-order modes [46]. Therefore, curvature not only reduces the transmission of the capillary, it also degrades the quality of the mode.

Stretching

Rigid capillaries shorter than 1 m can be kept relatively straight by supporting them in a v-groove, or by resting them in a glass tube with an inner diameter that accommodates the outer diameter of the capillary. It is very difficult to construct sufficiently straight supports for longer capillaries. A convenient solution for long capillaries is to stretch them: the capillary is supported only at the extremities, and tension is applied to stretch the capillary like the string on a guitar. Such stretching is easier to achieve with a flexible fibre than a rigid capillary, since less tension is needed to keep it straight and it is less likely to break in the process. However, burning the entrance of a flexible fibre is more likely in the case of slight misalignment of the incoming beam. For this reason, we chose to use rigid capillaries.

Figure A.8 shows the device designed and built to stretch a rigid capillary of inner diameter 350 μm and outer diameter of 1.6 mm. Such a device was placed on each end of the capillary. The main idea behind this device is to be able to fine-tune the angle at which tension is applied to both ends of the capillary, so that the capillary will be straight and stretched. In order for such a system to work, two important factors must be considered. Firstly, the capillary cannot be fixed in a way that its tip might make an angle with the rest of the capillary, as it will break when it is stretched. Secondly, the whole system must be gas-tight to withstand differential pumping, i.e. no gas must be able to enter the KF40 tube in which the capillary is fixed, as the capillary should be the only path for the gas to travel from the overpressure side to the vacuum side, thus creating a pressure gradient in the capillary.

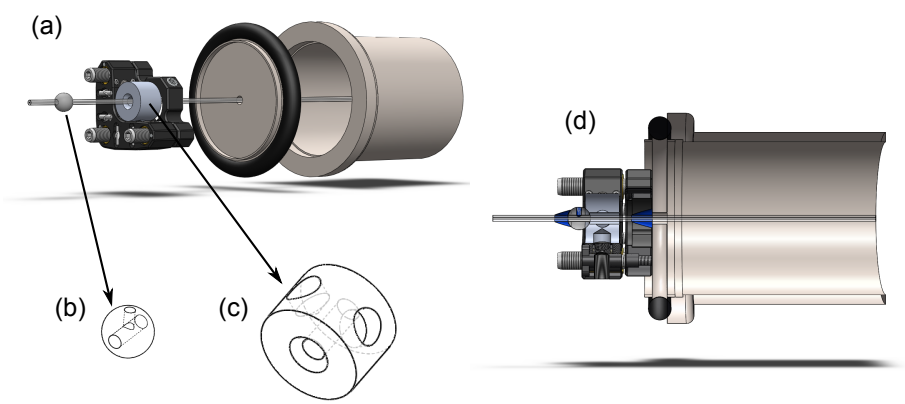

Figure A.8: Stretching device based on a standard $1/2''$ optics mount glued to a KF40 blind flange with a central hole. a) View of the different components of the stretching device. b) Sketch of the plastic ball inside which the capillary is glued. c) Sketch of the aluminium cylinder that is fixed to the mirror mount with two M4 screws using the threaded holes on the side of the cylinder. The cylinder will push on the plastic ball to stretch the capillary when the alignment screws of the mirror mount are screwed in. d) Stretching device after it has been glued. The epoxy for fibre optics is shown in blue.

To prevent the tip of the capillary from making an angle with the rest of it, the capillary is glued inside a plastic ball (Figure A.8b) which fits perfectly in a spherical groove created in an aluminium cylinder (Figure A.8d), thus allowing the direction

of the capillary to be adjusted during stretching. The plastic ball has a ∅1.7 mm hole drilled through it to accommodate the capillary, and a smaller hole on top for application of the glue. The capillary was glued inside the ball using this hole and from the front, using epoxy for fibre-optics applied with a syringe. This glue is very fluid, and the capillary had to be hung upside down so that the glue would dry symmetrically around it. During the gluing process, the tip of the capillary was protected using a flexible plastic hose with an inner diameter fitting the outer diameter of the capillary, to prevent glue from dripping into the entrance of the capillary. Gluing is quite difficult, and several capillaries were broken during this process.

The aluminium cylinder (Figure A.8c) has a ∅3 mm hole drilled all the way through it to accommodate the capillary, and two M4 threaded holes so it can be mounted on a Newport ∅1/2″ precision kinematic mirror mount. The screws from the mount are used to stretch and align the capillary, further preventing the tip of the capillary from making an angle with the rest of it. It may appear that having both the plastic ball and two alignment screws for the same purpose is redundant. However, the range of movement of the ball is limited by the length of the aluminium cylinder, so the ball cannot be used alone, and additional alignment is needed. Moreover, it is advantageous not to fix the capillary directly onto the cylinder (and therefore the mirror mount) to ensure some room for manoeuvre before stretching it, preventing it from breaking.

The mirror mount is glued to a blind KF40 flange using power epoxy. This is much easier to handle than the epoxy for fibre-optics and can be placed under strain after 5 min. The blank centring ring has a ∅3 mm hole drilled through it for the capillary. The centring ring is glued to the KF40 tube using power epoxy. It can support an O-ring so that another KF40 tube can be placed around the stretching device and connected to the first KF40 tube with a clamp, ensuring that the whole system is gas-tight.

The capillary must be stretched before making the system gas-tight because the capillary must be able to move inside the hole in the centring ring during the stretching procedure. Once stretching has been carried out, glue is applied around the capillary to seal the hole in the centring ring, to prevent gas from entering the KF40 tube. This will fix the position of the capillary preventing any further adjustments. The size of the hole in the centring ring is critical. It must be large enough for the capillary to move during stretching, without touching the edge of the hole; if it touches the edge, the capillary will break. On the other hand, the hole must be small enough to be easily sealed with glue. The epoxy for fibre-optics is too fluid to be used there, so power epoxy was used.

It is advisable to have an opening in the KF40 tube so that gas can be released in the case of a leak, underpressure or overpressure. Pumping this tube down to vacuum is an attractive option, but this may lead to deformation affecting the quality of the stretching. If one can be sure that there are no leaks, one option would be to fill the tube with water. This has several benefits: it increases the stability of the capillary, prevents vibrations, and cools the system thus minimizing thermal effects.

Based on our experience, the best procedure for stretching (illustrated in Figure A.9) is as follows.

1) Two counter-propagating HeNe lasers are aligned.

2) The capillary is placed between them.

3) The HeNe beam coming from the right is blocked. The left end (entrance side for the remaining HeNe beam) of the capillary is aligned with the HeNe beam coming from the left for best transmission.

4) The HeNe beam coming from the left is blocked. The right end (entrance) of the capillary is aligned to the HeNe beam coming from the right for best transmission.

5) The HeNe beam coming from the left is blocked. The HeNe beam coming from the right is transmitted through the capillary. The left extremity of the capillary (exit) is stretched using the three alignment screws of the stretching device. Stretching is performed to obtain the best possible mode. A fundamental mode should not be expected at this point, but most probably a higher-order mode.

6) The HeNe beam coming from the right is blocked. The left end (entrance) of the capillary is realigned for best transmission.

7) The HeNe beam coming from the left is transmitted through the capillary. The right end of the capillary (exit) is stretched using the three alignment screws of the stretching device. Stretching is performed to obtain the best possible mode.

8) The HeNe beam coming from the left is blocked. The right end (entrance) of the capillary is realigned for best transmission.

9) The four previous steps are repeated until a satisfactory fundamental mode is obtained. This procedure converges quite fast, and only 2-3 iterations should be necessary.

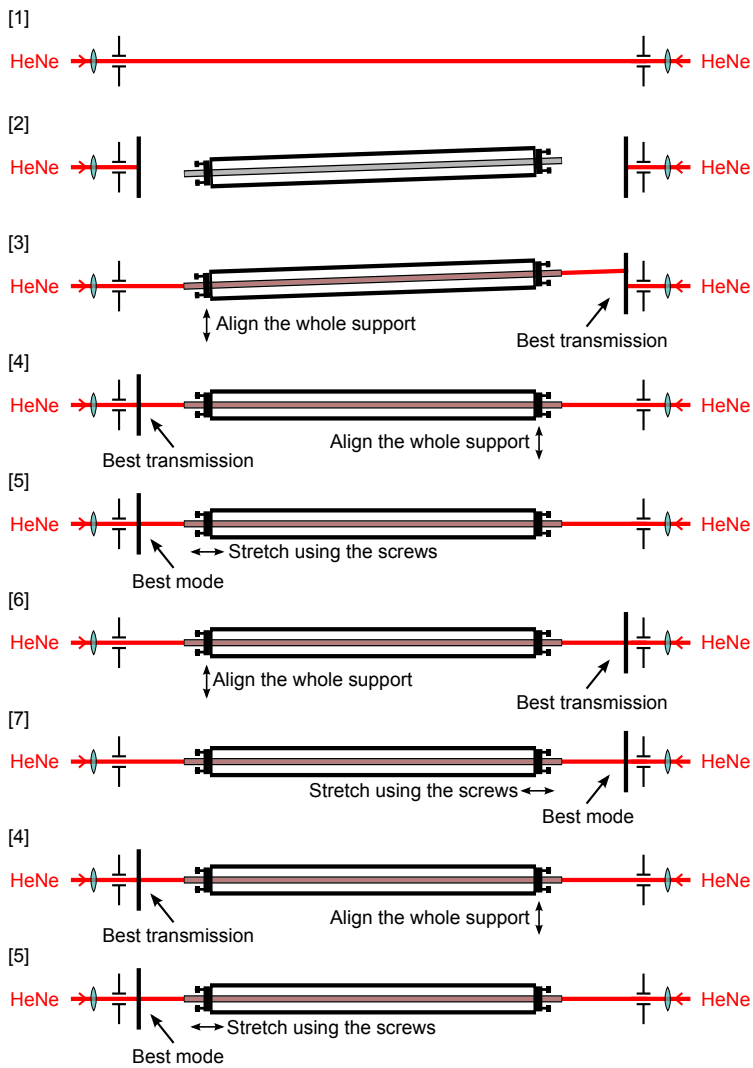

Figure A.9: Schematic illustrating the best procedure for stretching a capillary.

The author's contributions

I **Fast iterative retrieval algorithm for ultrashort pulse characterization using dispersion scans**
This paper introduces a new retrieval algorithm for d-scan traces and demonstrates its reliability with two examples: characterization of ultrashort pulses from an OPCPA and a hollow capillary. I performed most of the design and construction of the hollow-capillary setup and played a major role in performing the d-scan measurement. I did not take part in the development of the new algorithm.

II **Compact single-shot d-scan setup for the characterization of few-cycle laser pulses**
In this paper, an innovative compact design for single-shot d-scan is introduced and its reliability is demonstrated by measuring ultrashort pulses from a hollow capillary. I performed most of the design and construction of the hollow-capillary setup and played a major role in designing and constructing the single-shot d-scan setup, including the design, alignment and calibration of the imaging spectrometer. I planned the experiments and conducted them together with another student. I wrote most of the article.

III **Gating attosecond pulses in a noncollinear geometry**
In this paper, the emission of angularly separated IAPs using NOG is demonstrated experimentally. I played a major role in constructing the hollow-capillary setup and took part in constructing the NOG setup. I played a major role in performing the experiments. I performed most of the data analysis, and wrote most of the article.

IV **Scale-invariant nonlinear optics in gases**
In this paper, the scale invariance of most nonlinear optics phenomena in gases was shown for the first time, and a general scaling method for HHG and filamentation was presented. I took an active part in the experiments demonstrating the scale invariance of filaments.

V **Spectral phase measurement of a Fano resonance using tunable attosecond pulses**

The phase variation of an autoionizing Fano resonance in argon was measured using an interferometric method with a tunable source. The results are interpreted and compared to theoretical calculations. I took part in the operation of the tunable laser and participated in the final data acquisition. I did not participate in the theoretical analysis of the results.

Acknowledgements

First and foremost, I would like to thank my wife, Sofia Louisy, whose unconditional support through success, failure and mostly frustration (inherent in any experimental work), has gotten me through my PhD. We made it a routine for me to call her every day after work to tell her what I had done that day and, ultimately, this was the only way for me to compartmentalize my work and my private life, allowing my brain to get some well-deserved rest.

When I started my PhD in Lund, I was only 22. In the words of my co-workers, I was a "little child". Therefore, I still had a lot to learn; not only in Physics, but also in the "art" of working.

I would like to thank my main supervisor, Professor Anne L'Huillier, for teaching me the importance of a well-balanced life between friends/hobbies and work. I also want to thank her for supporting me when stress got the better of me, for always being there with an open door and an open mind to talk about any issue I might be facing. I want to thank her for showing me that a great mind can also come with a kind heart, and that professional success does not have to be gained at the expense of others. Finally, I thank her for answering so many Physics questions in such a clear way.

I would like to thank my co-supervisor, Cord Louis Arnold, for showing me the value of hard work, for always being there to answer my questions and experimental concerns, and, most of all, for all the help he provided in the lab, including, but not limited to, ensuring the best performance of the laser system.

I would like to thank my friend and co-worker, Neven Ibrakovic, for the coffee breaks filled with jokes and laughter. I want to thank him for the many evenings spent watching Planet Earth together; but most of all I want to thank him for being one of the best men (not only at my wedding) I know.

I would like to thank Hélène Coudert-Alteirac for the coffee breaks, the skating and the parties; Diego Guénot for the Physics and the fun with the ponies; Miguel Miranda for teaching me how to smartly align optical systems and for his generous help with so many things, especially the d-scan; Marija Kotur for all the fun; Eleonora Lorek for welcoming me so nicely from the very beginning (I will never forget the message on the board the first time I entered my office); Esben Witting Larsen for the beers, the Canadian adventures and for being the hand that pulls me underwater; Stefanos Carlström and Anne Harth for caring so much; Samuel Bengtsson for the way he tells stories; Emma Simpson for all the excellent stuffs; Piotr Rudawski for the football, the food and the vodka; Chen Guo for the help with the single-shot d-scan; Christoph Heyl for NOG; Lana Neoricic for the help with the capillary system; and the many

other people I worked with, Linnea Rading, Per Johnsson, Sylvain Maclot, Saikat Nandi, Shiyang Zhong, David Busto, Filippo Campi, Mathieu Gisselbrecht, Yu-Chen Cheng, Marcus Isinger, Jan Lahl, Sara Mikaelsson, Jasper Peshel, Hampus Wikmark, David Kroon, Bastian Manschwetus, Jan Vogelsang, and all the people from other universities that collaborated to this work.

I would like to thank all those in the administration, especially Anne Petersson Jungbeck, for solving all my practical problems, Jakob Testad for the coffee breaks, Åke Johansson for always fixing my computer so fast, and Professor Claes-Göran Wahlström for the guidance.

I came to Sweden for this PhD, but I found two other unexpected things that had a huge impact on my life. Firstly, I found my wife. Secondly, I found a huge skateboarding world filled with amazing people, and this was exactly what I needed to balance my work. I want to thank Mimmi for all the great skating and for being such a good friend, J-Mag for his support and the skate opportunities, Mark and Joanna, Max, Magnus and the Halmstad crew.

I also found a heavy metal band that allowed me to scream out my frustration. I want to thank Igor Petersson, Viktor Fältman and Laurent Huot.

I also want to thank my friends from my engineering school, Julien Lancelot and Thomas Avisse, who kept on visiting me despite the horrible weather.

Finally, I want to thank my family for all their support and love, mum and dad, mamie, Elodie, Julien and Pauline.

References

1. E. Treacy. *Optical pulse compression with diffraction gratings.* IEEE J. Quant. Electron. **5**, 454 – 458 (1969).

2. C. V. Shank, R. L. Fork, R. Yen, R. H. Stolen and W. J. Tomlinson. *Compression of femtosecond optical pulses.* Appl. Phys. Lett. **40**, 761–763 (1982).

3. O. Martinez. *3000 times grating compressor with positive group velocity dispersion: Application to fiber compensation in 1.3-1.6 μm region.* IEEE J. of Quant. Electron. **23**, 59 – 64 (1987).

4. G. Cheriaux, P. Rousseau, F. Salin, J. P. Chambaret, B. Walker and L. F. Dimauro. *Aberration-free stretcher design for ultrashort-pulse amplification.* Opt. Lett. **21**, 414–416 (1996).

5. R. L. Fork, O. E. Martinez and J. P. Gordon. *Negative dispersion using pairs of prisms.* Opt. Lett. **9**, 150 (1984).

6. Z. Cheng, F. Krausz and Ch. Spielmann. *Compression of 2 mJ kilohertz laser pulses to 17.5 fs by pairing double-prism compressor: analysis and performance.* Opt. Commun. **201**, 145 – 155 (2002).

7. B. Proctor and F. Wise. *Quartz prism sequence for reduction of cubic phase in a mode-locked Ti:Al_2O_3 laser.* Opt. Lett. **17**, 1295–1297 (1992).

8. S. Kane and J. Squier. *Grism-pair stretcher-compressor system for simultaneous second- and third-order dispersion compensation in chirped-pulse amplification.* JOSA B - Opt. Phys. **14**, 661–665 (1997).

9. R. Szipöcs, K. Ferencz, Ch. Spielmann and F. Krausz. *Chirped multilayer coatings for broadband dispersion control in femtosecond lasers.* Opt. Lett. **19**, 201 (1994).

10. F. X. Kärtner, N. Matuschek, T. Schibli, U. Keller, H. A. Haus, C. Heine, R. Morf, V. Scheuer, M. Tilsch and T. Tschudi. *Design and fabrication of double-chirped mirrors.* Opt. Lett. **22**, 831 (1997).

11. N. Matuschek, F. X. Kärtner and U. Keller. *Theory of Double-Chirped Mirrors.* IEEE J. Quant. Electron. **4**, 197 (1998).

12. M. Nisoli, S. De Silvestri and O. Svelto. *Generation of high energy 10 fs pulses by a new pulse compression technique.* Appl. Phys. Lett. **68**, 2793 (1996).

13. M. Nisoli, S. De Silvestri, O. Svelto, R. Szipöcs, K. Ferencz, Ch. Spielmann, S. Sartania and F. Krausz. *Compression of high-energy laser pulses below 5 fs.* Opt. Lett. **22**, 522 (1997).

14. C. P. Hauri, W. Kornelis, F. W. Helbing, A. Heinrich, A. Couairon, A. Mysyrowicz, J. Biegert and U. Keller. *Generation of intense, carrier-envelope phase-locked few-cycle laser pulses through filamentation.* Appl. Phys. B **79**, 673 (2004).

15. A. Couairon and A. Mysyrowicz. *Femtosecond filamentation in transparent media.* Phys. Rep. **441**, 47–189 (2007).

16. A. Dubietis, G. Jonušauskas and A. Piskarskas. *Powerful femtosecond pulse generation by chirped and stretched pulse parametric amplification in BBO crystal.* Opt. Commun. **88**, 437 – 440 (1992).

17. M. Miranda, C. L. Arnold, T. Fordell, F. Silva, B. Alonso, R. Weigand, A. L'Huillier and H. Crespo. *Characterization of broadband few-cycle laser pulses with the d-scan technique.* Opt. Express **20**, 18732–18743 (2012).

18. A. McPherson, G. Gibson, H. Jara, U. Johann, T. S. Luk, I. A. McIntyre, K. Boyer and C. K. Rhodes. *Studies of multiphoton production of vacuum-ultraviolet radiation in the rare gases.* JOSA B **4**, 595 (1987).

19. M. Ferray, A. L'Huillier, X. F. Li, L. A. Lompre, G. Mainfray and C. Manus. *Multiple-harmonic conversion of 1064 nm radiation in rare gases.* J. Phys. B **21**, L31 (1988).

20. P. Tournois. *Acousto-optic programmable dispersive filter for adaptive compensation of group delay time dispersion in laser systems.* Opt. Commun. **140**, 245 (1997).

21. T. Oksenhendler, D. Kaplan, P. Tournois, G.M. Greetham and F. Estable. *Intracavity acousto-optic programmable gain control for ultra-wide-band regenerative amplifiers.* Appl. Phys. B: Lasers Opt. **83**, 491–494 (2006).

22. A. Moulet, S. Grabielle, C. Cornaggia, N. Forget and T. Oksenhendler. *Single-shot, high-dynamic-range measurement of sub-15 fs pulses by self-referenced spectral interferometry.* Opt. Lett. **35**, 3856–3858 (2010).

23. T. Oksenhendler, S. Coudreau, N. Forget, V. Crozatier, S. Grabielle, R. Herzog, O. Gobert and D. Kaplan. *Self-referenced spectral interferometry.* Appl. Phys. B **99**, 7 (2010).

24. N. Minkovski, G. I. Petrov, S. M. Saltiel, O. Albert and J. Etchepare. *Nonlinear polarization rotation and orthogonal polarization generation experienced in a single-beam configuration.* JOSA B **21**, 1659–1664 (2004).

25. L. Lepetit, G. Chériaux and M. Joffre. *Linear techniques of phase measurement by femtosecond spectral interferometry for applications in spectroscopy.* JOSA B **12**, 2467–2474 (1995).

26. M. D. Feit and J. A. Fleck. *Beam nonparaxiality, filament formation, and beam breakup in the self-focusing of optical beams.* JOSA B **5**, 633–640 (1988).

27. A. V. Husakou and J. Herrmann. *Supercontinuum generation of higher-order solitons by fission in photonic crystal fibers.* Phys. Rev. Lett. **87**, 203901 (2001).

28. J. Kerr. *XL. A new relation between electricity and light: Dielectrified media birefringent.* The London, Edinburgh, and Dublin Philosophical Magazine and Journal of Science **50**, 337–348 (1875).

29. J. Kerr. *LIV. A new relation between electricity and light: Dielectrified media birefringent (second paper).* The London, Edinburgh, and Dublin Philosophical Magazine and Journal of Science **50**, 446–458 (1875).

30. C. R. Mansfield and E. R. Peck. *Dispersion of helium.* JOSA **59**, 199–204 (1969).

31. A. Bideau-Mehu, Y. Guern, R. Abjean and A. Johannin-Gilles. *Measurement of refractive indices of neon, argon, krypton and xenon in the 253.7–140.4 nm wavelength range. Dispersion relations and estimated oscillator strengths of the resonance lines.* J. Quant. Spectrosc. Radiat. Transfer **25**, 395–402 (1981).

32. E. R. Peck and D. J. Fisher. *Dispersion of argon.* JOSA **54**, 1362–1364 (1964).

33. C. Bree, A. Demircan and G. Steinmeyer. *Method for computing the nonlinear refractive index via Keldysh theory.* IEEE J. Quant. Electron. **46**, 433–437 (2010).

34. G. A. Askaryan. *Cerenkov radiation and transition radiation from electromagnetic waves.* Sov. Phys. JETP **15**, 943 (1962).

35. R. Y. Chiao, E. Garmire and C. H. Townes. *Self-trapping of optical beams.* Phys. Rev. Lett. **13**, 479 (1964).

36. P. L. Kelley. *Self-focusing of optical beams.* Phys. Rev. Lett. **15**, 1005 (1965).

37. P. Lallemand and N. Bloembergen. *Self-focusing of laser beams and stimulated Raman gain in liquids.* Phys. Rev. Lett. **15**, 1010 (1965).

38. E. Garmire, R. Y. Chiao and C. H. Townes. *Dynamics and characteristics of the self-trapping of intense light beams.* Phys. Rev. Lett. **16**, 347 (1966).

39. G. Fibich and A. L. Gaeta. *Critical power for self-focusing in bulk media and in hollow waveguides.* Opt. Lett. (2000).

40. A. M. Perelomov, V. S. Popov and M. V. Terent'ev. *Ionization of atoms in an alternating electric field.* Sov. Phys. JETP **23**, 924–934 (1966).

41. A. M. Perelomov, V. S. Popov and M. V. Terent'ev. *Ionization of atoms in an alternating electric field: II.* Sov. Phys. JETP **24**, 207–217 (1967).

42. A. M. Perelomov and V. S. Popov. *Ionization of atoms in an alternating electric field: III.* Sov. Phys. JETP **25** (1967).

43. G. P. Agrawal. *Nonlinear Fiber Optics.* Academic Press (1989).

44. S. C. Pinault and M. J. Potasek. *Frequency broadening by self-phase modulation in optical fibers.* JOSA B **2**, 1318–1319 (1985).

45. R. H. Stolen and C. Lin. *Self-phase-modulation in silica optical fibers.* Phys. Rev. A **17**, 1448 (1978).

46. E. A. J. Marcatili and R. A. Sctimeltzer. *Hollow Metallic and Dielectric Waveguides for Long Distance Optical Transmission and Lasers.* Bell System Technical Journal **43**, 1783 (1964).

47. X. Chen, A. Jullien, A. Malvache, L. Canova, A. Borot, A. Trisorio, C. G. Durfee and R. Lopez-Martens. *Generation of 4.3 fs, 1 mJ laser pulses via compression of circularly polarized pulses in a gas-filled hollow-core fiber.* Opt. Lett. **34** (2009).

48. J. S. Robinson, C. A. Haworth, H. Teng, R. A. Smith, J. P. Marangos and J. W. G. Tisch. *The generation of intense, transform-limited laser pulses with tunable duration from 6 to 30 fs in a differentially pumped hollow fibre.* Appl. Phys. B: Lasers Opt. **85**, 525–529 (2006).

49. T. Nagy, V. Pervak and P. Simon. *Optimal pulse compression in long hollow fibers.* Opt. Lett. **36**, 4422–4424 (2011).

50. J. H. Marburger. *Self-focusing: theory.* Prog. Quantum Electron. **4**, 35–110 (1975).

51. E. L. Dawes and J. H. Marburger. *Computer studies in self-focusing.* Phys. Rev. **179**, 862 (1969).

52. K. G. Makris, Z. H. Musslimani, D. N. Christodoulides and S. Rotter. *Constant-intensity waves and their modulation instability in non-Hermitian potentials.* Nat. Commun. **6**, 7257 (2015).

53. M. Geissler, G. Tempea, A. Scrinzi, M. Schnürer, F. Krausz and T. Brabec. *Light Propagation in Field-Ionizing Media: Extreme Nonlinear Optics.* Phys. Rev. Lett. **83**, 2930 (1999).

54. E. Esarey, C. B. Schroeder and W. P. Leemans. *Physics of laser-driven plasma-based electron accelerators.* Rev. Mod. Phys. **81**, 1229–1285 (2009).

55. N. Matuschek, F. X. Kärtner and U. Keller. *Analytical Design of Double-Chirped Mirrors with Custom-Tailored Dispersion Characteristics.* IEEE J. Quant. Electron. **35**, 129 (1999).

56. V. Pervak, I. Ahmad, M. K. Trubetskov, A. V. Tikhonravov and F. Krausz. *Double-angle multilayer mirrors with smooth dispersion characteristics.* Opt. Express **17**, 7943–7951 (2009).

57. F. Silva, M. Miranda, B. Alonso, J. Rauschenberger, V. Pervak and H. Crespo. *Simultaneous compression, characterization and phase stabilization of GW-level 1.4 cycle VIS-NIR femtosecond pulses using a single dispersion-scan setup.* Opt. Express **22**, 10181–10191 (2014).

58. W. H. Knox, N. M. Pearson, K. D. Li and C. A. Hirlimann. *Interferometric measurements of femtosecond group delay in optical components.* Opt. Lett. **13**, 574–576 (1988).

59. T. V. Amotchkina, A. V. Tikhonravov, M. K. Trubetskov, D. Grupe, A. Apolonski and V. Pervak. *Measurement of group delay of dispersive mirrors with white-light interferometer.* Appl. Opt. **48**, 949–956 (2009).

60. I. A. Walmsley and C. Dorrer. *Characterization of ultrashort electromagnetic pulses.* Adv. Opt. Photon. **1**, 308–437 (2009).

61. D. J. Kane and R. Trebino. *Characterization of Arbitrary Femtosecond Pulses Using Frequency-Resolved Optical Gating.* IEEE J. Quantum Electron. **29**, 571 (1993).

62. R. Trebino and D. J. Kane. *Using phase retrieval to measure the intensity and phase of ultrashort pulses: frequency-resolved optical gating.* JOSA A **10**, 1101 (1993).

63. R. Trebino, K. W. DeLong, D. N. Fittinghoff, J. Sweetser, M. A. Krumbügel and B. Richman. *Measuring ultrashort laser pulses in the time-frequency domain using frequency-resolved optical gating.* Rev. Sci. Instrum. **68**, 1 (1997).

64. C. Iaconis and I. A. Walmsley. *Spectral phase interferometry for direct electric field reconstruction of ultrashort optical pulses.* Opt. Lett. **23**, 792 (1998).

65. P. O'Shea, M. Kimmel, X. Gu and R. Trebino. *Highly simplified device for ultrashort-pulse measurement.* Opt. Lett. **26**, 932–934 (2001).

66. A. S. Wyatt, I. A. Walmsley, G. Stibenz and G. Steinmeyer. *Sub-10 fs pulse characterization using spatially encoded arrangement for spectral phase interferometry for direct electric field reconstruction.* Opt. Lett. **31**, 1914–1916 (2006).

67. S. Akturk, C. D'Amico and A. Mysyrowicz. *Measuring ultrashort pulses in the single-cycle regime using frequency-resolved optical gating.* JOSA B **25**, A63–A69 (2008).

68. J. R. Birge, H. M. Crespo and F. X. Kärtner. *Theory and design of two-dimensional spectral shearing interferometry for few-cycle pulse measurement.* JOSA B **27**, 1165–1173 (2010).

69. K. W. DeLong, D. N. Fittinghoff, R. Trebino, B. Kohler and K. Wilson. *Pulse retrieval in frequency-resolved optical gating based on the method of generalized projections.* Opt. Lett. **19**, 2152–2154 (1994).

70. V. V. Lozovoy, I. Pastirk and M. Dantus. *Multiphoton intrapulse interference. IV. Ultrashort laserpulse spectral phase characterization and compensation.* Opt. Lett. **29**, 775–777 (2004).

71. V. Loriot, G. Gitzinger and N. Forget. *Self-referenced characterization of femtosecond laser pulses by chirp scan.* Opt. Express **21**, 24879–24893 (2013).

72. M. Miranda. *Sources and Diagnostics for Attosecond Science.* PhD thesis (2012).

73. M. Miranda, T. Fordell, C. Arnold, A. L'Huillier and H. Crespo. *Simultaneous compression and characterization of ultrashort laser pulses using chirped mirrors and glass wedges.* Opt. Express **20**, 688–697 (2012).

74. D. J. Kane and R. Trebino. *Single-shot measurement of the intensity and phase of an arbitrary ultrashort pulse by using frequency-resolved optical gating.* Opt. Lett. **18**, 823 (1993).

75. D. Fabris, W. Holgado, F. Silva, T. Witting, J. W. G. Tisch and H. Crespo. *Single-shot implementation of dispersion-scan for the characterization of ultrashort laser pulses.* Opt. Express **23**, 32803–32808 (2015).

76. F. Silva, I. Sola, H. Crespo, R. Romero, M. Miranda, C. L. Arnold, A. L'Huillier, J. Trull and C. Cojocaru. *Monolithic single-shot dispersion-scan: a new tool for real-time measurement and optimization of femtosecond Pulses.* In *CLEO/Europe-EQEC* (2017).

77. B. Bates, M. McDowell and A. C. Newton. *Correction of astigmatism in a Czerny-Turner spectrograph using a plane grating in divergent illumination.* J. Phys. E: Sci. Instrum. **3**, 206 (1970).

78. D. R. Austin, T. Witting and I. A. Walmsley. *Broadband astigmatism-free Czerny-Turner imaging spectrometer using spherical mirrors.* Appl. Opt. **48**, 3846–3853 (2009).

79. Y. An, Q. Sun, Y. Liu, C. Li and Z.-Q. Wang. *The design of astigmatism-free crossed Czerny-Turner spectrometer.* Optik - International Journal for Light and Electron Optics **124**, 2539 – 2543 (2013).

80. Z. Wei, H. Han, W. Zhang, Y. Zhao, J. Zhu, H. Teng and Q. Du. *Measurement and Control of Carrier-Envelope Phase in Femtosecond Ti:sapphire Laser.* In M. Grishin, editor, *Advances in Solid State Lasers Development and Applications* chapter 14. InTech Rijeka (2010).

81. H. R. Telle, G. Steinmeyer, A. E. Dunlop, J. Stenger, D. H. Sutter and U. Keller. *Carrier-envelope offset phase control: A novel concept for absolute optical frequency measurement and ultrashort pulse generation.* Appl. Phys. B **69**, 327 (1999).

82. D. J. Jones, S. A. Diddams, J. K. Ranka, A. Stentz, R. S. Windeler, J. L. Hall and S. T. Cundiff. *Carrier-envelope phase control of femtosecond mode-locked lasers and direct optical frequency synthesis.* Science **288**, 635 (2000).

83. A. Apolonski, A. Poppe, G. Tempea, Ch. Spielmann, Th. Udem, R. Holzwarth, T. W. Hänsch and F. Krausz. *Controlling the phase evolution of few-cycle light pulses.* Phys. Rev. Lett. **85**, 740 (2000).

84. M. Kakehata, H. Takada, Y. Kobayash, K. Torizuka, Y. Fujihira, T. Homma and H. Takahashi. *Single-shot measurement of carrier-envelope phase changes by spectral interferometry.* Opt. Lett. **26**, 1436 (2001).

85. J. Rauschenberger, T. Fuji, M. Hentschel, A. J. Verhoef, T. Udem, C. Gohle, T. W. Hansch and F. Krausz. *Carrier-envelope phase-stabilized amplifier system.* Laser Phys. Lett. **3**, 37–42 (2006).

86. S. B. P. Radnor, P. Kinsler and G. H. C. New. *Proposal for absolute CEP measurement using 0-to-f self-referencing.* arXiv preprint arXiv:0903.2935 (2009).

87. P. M. Paul, E. S. Toma, P. Breger, G. Mullot, F. Augé, Ph. Balcou, H. G. Muller and P. Agostini. *Observation of a train of attosecond pulses from high harmonic generation.* Science **292**, 1689 (2001).

88. Y. Mairesse, A. de Bohan, L. J. Frasinski, H. Merdji, L. C. Dinu, P. Monchicourt, P. Breger, M. Kovačev, R. Taïeb, B. Carré, H. G. Muller, P. Agostini and P. Salières. *Attosecond synchronization of high-harmonic soft X-rays.* Science **302**, 1540 (2003).

89. R. López-Martens, K. Varjú, P. Johnsson, J. Mauritsson, Y. Mairesse, P. Salières, M. B. Gaarde, K. J. Schafer, A. Persson, S. Svanberg, C.-G. Wahlström and A. L'Huillier. *Amplitude and Phase Control of Attosecond Light Pulses.* Phys. Rev. Lett. **94**, 033001 (2005).

90. M. Schultze, M. Fieß, N. Karpowicz, J. Gagnon, M. Korbman, M. Hofstetter, S. Neppl, A. L. Cavalieri, Y. Komninos, Th. Mercouris, C. A. Nicolaides, R. Pazourek, S. Nagele, J. Feist, J. Burgdörfer, A. M. Azzeer, R. Ernstorfer, R. Kienberger, U. Kleineberg, E. Goulielmakis, F. Krausz and V. S. Yakovlev. *Delay in Photoemission.* Science **328**, 1658–1662 (2010).

91. K. Klünder, J. M. Dahlström, M. Gisselbrecht, T. Fordell, M. Swoboda, D. Guénot, P. Johnsson, J. Caillat, J. Mauritsson, A. Maquet, R. Taïeb and A. L'Huillier. *Probing Single-Photon Ionization on the Attosecond Time Scale.* Phys. Rev. Lett. **106**, 143002 (2011).

92. Á. Jiménez-Galán, L. Argenti and F. Martín. *Modulation of Attosecond Beating in Resonant Two-Photon Ionization.* Phys. Rev. Lett. **113**, 263001 (2014).

93. R. Pazourek, S. Nagele and J. Burgdörfer. *Attosecond chronoscopy of photoemission.* Rev. Mod. Phys. **87**, 765 (2015).

94. M. Isinger, R.J. Squibb, D. Busto, S. Zhong, A. Harth, D. Kroon, S. Nandi, C. L. Arnold, M. Miranda, J. M. Dahlström, E. Lindroth, R. Feifel, M. Gisselbrecht and A. L'Huillier. *Photoionization in the time and frequency domain.* Science (2017).

95. S. Haessler, B. Fabre, J. Higuet, J. Caillat, T. Ruchon, P. Breger, B. Carré, E. Constant, A. Maquet, E. Mével, P. Salières, R. Taïeb and Y. Mairesse. *Phase-resolved attosecond near-threshold photoionization of molecular nitrogen.* Phys. Rev. A **80**, 011404 (2009).

96. M. Huppert, I. Jordan, D. Baykusheva, A. von Conta and H. J. Wörner. *Attosecond delays in molecular photoionization.* Phys. Rev. Lett. **117**, 093001 (2016).

97. A. L. Cavalieri, N. Müller, Th. Uphues, V. S. Yakovlev, A. Baltuška, B. Horvath, B. Schmidt, L. Blümel, R. Holzwarth, S. Hendel, M. Drescher, U. Kleineberg, P. M. Echenique, R. Kienberger, F. Krausz and U. Heinzmann. *Attosecond spectroscopy in condensed matter.* Nature **449**, 1029 (2007).

98. C. M. Heyl, S. N. Bengtsson, S. Carlström, J. Mauritsson, C. L. Arnold and A. L'Huillier. *Noncollinear optical gating.* New J. Phys. **16**, 052001 (2014).

99. R. J. Jones, K. D. Moll, M. J. Thorpe and J. Ye. *Phase-Coherent Frequency Combs in the Vacuum Ultraviolet via High-Harmonic Generation inside a Femtosecond Enhancement Cavity.* Phys. Rev. Lett. **94**, 193201 (2005).

100. C. Gohle, T. Udem, M. Herrmann, J. Rauschenberger, R. Holzwarth, H. A. Schuessler, F. Krausz and T. W. Hänsch. *A frequency comb in the extreme ultraviolet.* Nature **436**, 234 (2005).

101. X. F. Li, A. L'Huillier, M. Ferray, L. A. Lompre and G. Mainfray. *Multiple-harmonic generation in rare-gases at high laser intensity.* Phys. Rev. A **39**, 5751–5761 (1989).

102. K. C. Kulander and B. W. Shore. *Calculations of Multiple-Harmonic Conversion of 1064-nm Radiation in Xe.* Phys. Rev. Lett. **62**, 524 (1989).

103. J. L. Krause, K. J. Schafer and K. C. Kulander. *Calculation of photoemission from atoms subject to intense laser fields.* Phys. Rev. A **45**, 4998 (1992).

104. K. C. Kulander, K. J. Schafer and J. L. Krause. *Dynamics of short-pulse excitation, ionization and harmonic conversion.* In *Super-Intense Laser-Atom Physics.* Plenum Press, New York (1993).

105. K. J. Schafer, B. Yang, L. F. DiMauro and K. C. Kulander. *Above threshold ionization beyond the high harmonic cutoff.* Phys. Rev. Lett. **70**, 1599 (1993).

106. P. B. Corkum. *Plasma perspective on strong-field multiphoton ionization.* Phys. Rev. Lett. **71**, 1994 (1993).

107. M. Yu. Kuchiev. *Atomic antenna.* JETP Lett. **45**, 404–406 (1987).

108. M. Lewenstein, Ph. Balcou, M. Yu. Ivanov, A. L'Huillier and P. B. Corkum. *Theory of high-order harmonic generation by low-frequency laser fields.* Phys. Rev. A **49**, 2117 (1994).

109. A. L'Huillier, M. Lewenstein, P. Salières, Ph. Balcou, M. Yu. Ivanov, J. Larsson and C. G. Wahlström. *High-order harmonic generation cutoff.* Phys. Rev. A **48**, R3433 (1993).

110. E. Constant, D. Garzella, P. Breger, E. Mével, Ch. Dorrer, C. Le Blanc, F. Salin and P. Agostini. *Optimizing High Harmonic Generation in Absorbing Gases: Model and Experiment.* Phys. Rev. Lett. **82**, 1668 (1999).

111. T. Brabec. *Strong Field Laser Physics* volume 134 of *Springer Series in Optical Science.* Springer (2009).

112. E. Takahashi, Y. Nabekawa, T. Otsuka, M. Obara and K. Midorikawa. *Generation of highly coherent submicrojoule soft x rays by high-order harmonics.* Phys. Rev. A **66**, 021802– (2002).

113. C. M. Heyl, J. Güdde, A. L'Huillier and U. Höfer. *High-order harmonic generation with μJ laser pulses at high repetition rates.* J. Phys. B: At., Mol. Opt. Phys. **45**, 074020 (2012).

114. J. Rothhardt, M. Krebs, S. Hädrich, S. Demmler, J. Limpert and A. Tünnermann. *Absorption-limited and phase-matched high harmonic generation in the tight focusing regime.* New J. Phys. **16**, 033022 (2014).

115. V. Gruson, L. Barreau, Á. Jiménez-Galan, F. Risoud, J. Caillat, A. Maquet, B. Carré, F. Lepetit, J.-F. Hergott, T. Ruchon, L. Argenti, R. Taïeb, F. Martín and P. Salières. *Attosecond dynamics through a Fano resonance: Monitoring the birth of a photoelectron.* Science **354**, 734–738 (2016).

116. D. Busto, L. Barreau, M. Isinger, M. Turconi, C. Alexandridi, A. Harth, S. Zhong, R. J. Squibb, D. Kroon, S. Plogmaker, M. Miranda, Á. Jiménez-Galan, L. Argenti, C. L. Arnold, R. Feifel, F. Martín, M. Gisselbrecht, A. L'Huillier and P. Salières. *Time-frequency representations of autoionization dynamics in helium.* arXiv preprint arXiv:1709.07639 (2017).

117. V. Véniard, R. Taïeb and A. Maquet. *Two-Color Multiphoton Ionization of Atoms Using High-Order Harmonic Radiation.* Phys. Rev. Lett. **74**, 4161 (1995).

118. V. Véniard, R. Taïeb and A. Maquet. *Phase dependence of (N+1)-color (N>1) IR–UV photoionization of atoms with higher harmonics.* Phys. Rev. A **54**, 721 (1996).

119. U. Fano. *Effects of configuration interaction on intensities and phase shifts.* Phys. Rev. **124**, 1866 (1961).

120. E. Goulielmakis, Z. Loh, A. Wirth, R. Santra, N. Rohringer, V. S. Yakovlev, S. Zherebtsov, T. Pfeifer, A. M. Azzeer, M. F. Kling, S. R. Leone and F. Krausz. *Real-time observation of valence electron motion.* Nature **466**, 739–743 (2010).

121. K. T. Kim, C. Zhang, T. Ruchon, J.-F. Hergott, T. Auguste, D. M. Villeneuve, P. B. Corkum and F. Quere. *Photonic streaking of attosecond pulse trains.* Nat. Photonics **7**, 651–656 (2013).

122. S. R. Leone, C. W. McCurdy, J. Burgdörfer, L. S. Cederbaum, Z. Chang, N. Dudovich, J. Feist, C. H. Greene, M. Ivanov, R. Kienberger, U. Keller, M. F. Kling, Z.-H. Loh, T. Pfeifer, A. N. Pfeiffer, R. Santra, K. Schafer, A. Stolow, U. Thumm and M. J. J. Vrakking. *What will it take to observe processes "in real time"?* Nat. Photonics **8**, 162–166 (2014).

123. Y. Nabekawa, T. Shimizu, Y. Furukawa, E. J. Takahashi and K. Midorikawa. *Interferometry of Attosecond Pulse Trains in the Extreme UltravioletWavelength Region.* Phys. Rev. Lett. **102**, 213904 (2009).

124. P. Tzallas, L. A. A. Skantzakis, E .and Nikolopoulos, G. D. Tsakiris and D. Charalambidis. *Extreme-ultraviolet pump-probe studies of one-femtosecond-scale electron dynamics.* Nat. Phys. **7**, 781–784 (2011).

125. E. J. Takahashi, P. Lan, O. D. Mücke, Y. Nabekawa and K. Midorikawa. *Attosecond nonlinear optics using gigawatt-scale isolated attosecond pulses.* Nat. Commun. **4** (2013).

126. F. Calegari, G. Sansone, S. Stagira, C. Vozzi and M. Nisoli. *Advances in attosecond science.* J. Phys. B: At., Mol. Opt. Phys. **49**, 062001 (2016).

127. M. Chini, K. Zhao and Z. Chang. *The generation, characterization and applications of broadband isolated attosecond pulses.* Nat. Photonics **8**, 178–186 (2014).

128. M. Nisoli and G. Sansone. *New frontiers in attosecond science.* Prog. Quantum Electron. **33**, 17–59 (2009).

129. G. Sansone, L. Poletto and M. Nisoli. *High-energy attosecond light sources.* Nat. Photonics **5**, 655–663 (2011).

130. M. Hentschel, R. Kienberger, Ch. Spielmann, G. A. Reider, N. Milosevic, T. Brabec, P. Corkum, U. Heinzmann, M. Drescher and F. Krausz. *Attosecond metrology.* Nature **414**, 509 (2001).

131. I. P. Christov, M. M. Murnane and H. C. Kapteyn. *High-harmonic generation of attosecond pulses in the single cycle regime.* Phys. Rev. Lett. **78**, 1251 (1997).

132. P. B. Corkum, N. H. Burnett and M. Y. Ivanov. *Subfemtosecond pulses.* Opt. Lett. **19**, 1870 (1994).

133. O. Tcherbakoff, E. Mével, D. Descamps, J. Plumridge and E. Constant. *Time-gated high-order harmonic generation.* Phys. Rev. A **68**, 0438040 (2003).

134. H. Mashiko, S. Gilbertson, C. Li, S. D. Khan, M. M. Shakya, E. Moon and Z. Chang. *Double optical gating of high-order harmonic generation with carrier-envelope phase stabilized lasers.* Phys. Rev. Lett. **100**, 103906 (2008).

135. X. Feng, S. Gilbertson, H. Mashiko, H. Wang, S. D. Khan, M. Chini, Y. Wu, K. Zhao and Z. Chang. *Generation of Isolated Attosecond Pulses with 20 to 28 Femtosecond Lasers.* Phys. Rev. Lett. **103**, 183901 (2009).

136. F. Ferrari, F. Calegari, M. Lucchini, C. Vozzi, S. Stagira, G. Sansone and M. Nisoli. *High-energy isolated attosecond pulses generated by above-saturation few-cycle fields.* Nat. Photonics **4**, 875–879 (2010).

137. H. Vincenti and F. Quéré. *Attosecond Lighthouses: How To Use Spatiotemporally Coupled Light Fields To Generate Isolated Attosecond Pulses.* Phys. Rev. Lett. **108**, 113904 (2012).

138. J. A. Wheeler, A. Borot, S. Monchoce, H. Vincenti, A. Ricci, A. Malvache, R. Lopez-Martens and F. Quere. *Attosecond lighthouses from plasma mirrors.* Nat. Photonics **6**, 829–833 (2012).

139. T. J. Hammond, G. Brown, K. T. Kim, D. M. Villeneuve and P. B. Corkum. *Attosecond pulses measured from the attosecond lighthouse.* Nat. Photonics **10**, 171–175 (2016).

140. J. Mauritsson, T. Remetter, M. Swoboda, K. Klünder, A. L'Huillier, K. J. Schafer, O. Ghafur, F. Kelkensberg, W. Siu, P. Johnsson, M. J. J. Vrakking, I. Znakovskaya, T. Uphues, S. Zherebtsov, M. F. Kling, F. Lepine, E. Benedetti, F. Ferrari, G. Sansone and M. Nisoli. *Attosecond Electron Spectroscopy Using a Novel Interferometric Pump-Probe Technique.* Phys. Rev. Lett. **105**, 053001 (2010).

141. Ch. Neidel, J. Klei, C.-H. Yang, A. Rouzée, M. J. J. Vrakking, K. Klünder, M. Miranda, C. L. Arnold, T. Fordell, A. L'Huillier, M. Gisselbrecht, P. Johnsson, M. P. Dinh, E. Suraud, P.-G. Reinhard, V. Despré, M. A. L. Marques and F. Lépine. *Probing Time-Dependent Molecular Dipoles on the Attosecond Time Scale.* Phys. Rev. Lett. **111**, 033001 (2013).

142. D. Milam. *Review and assessment of measured values of the nonlinear refractive-index coefficient of fused silica.* Appl. Opt. **37**, 546–550 (1998).

143. T. Nagy, M. Forster and P. Simon. *Flexible hollow fiber for pulse compressors.* Appl. Opt. **47**, 3264–3268 (2008).

Papers

Paper I

Fast iterative retrieval algorithm for ultrashort pulse characterization using dispersion scans

M. Miranda, J. Penedones, C. Guo, A. Harth, M. Louisy, L. Neoricic, A. L'Huillier, and C. L. Arnold.

Journal of the Optical Society of America B **34**, 190-197 (2017).

Paper II

Compact single-shot d-scan setup for the characterization of few-cycle laser pulses

M. Louisy*, C. Guo*, L. Neoricic, S. Zhong, A. L'Huillier, C. L. Arnold, and M. Miranda;
(*Authors contributed equally).

Applied Optics **56**, 9084-9089 (2017).

Paper III

Gating attosecond pulses in a noncollinear geometry

M. Louisy*, C. L. Arnold*, M. Miranda, E. W. Larsen,
S. N. Bengtsson, D. Kroon, M. Kotur, D. Guénot, L. Rading,
P. Rudawski, F. Brizuela, F. Campi, B. Kim, A. Jarnac, A. Houard,
J. Mauritsson, P. Johnsson, A. L'Huillier, and C. M. Heyl;
(*Authors contributed equally).

Optica **2**, 563-566 (2015).

Paper IV

Scale-invariant nonlinear optics in gases

C. M. Heyl, H. Coudert-Alteirac, M. Miranda, M. Louisy, K. Kovacs, V. Tosa, E. Balogh, K. Varjú, A. L'Huillier, A. Couairon, and C. L. Arnold.

Optica **3**, 75-81 (2016).

Paper V

Spectral phase measurement of a Fano resonance using tunable attosecond pulses

M. Kotur, D. Guénot, D. Kroon, E. W. Larsen, M. Miranda, M. Louisy, S. N. Bengtsson, S. Carlström, J. Mauritsson, J. M. Dahlström, S. E. Canton, M. Gisselbrecht, C. L. Arnold, and A. L'Huillier.

Nature Communications **7**, 10566 (2016).